Heinrich Heine Universität Düsseldorf

Development and Characterization of an Ion Trap Apparatus for Spectroscopy of Single Molecular and Atomic Ions

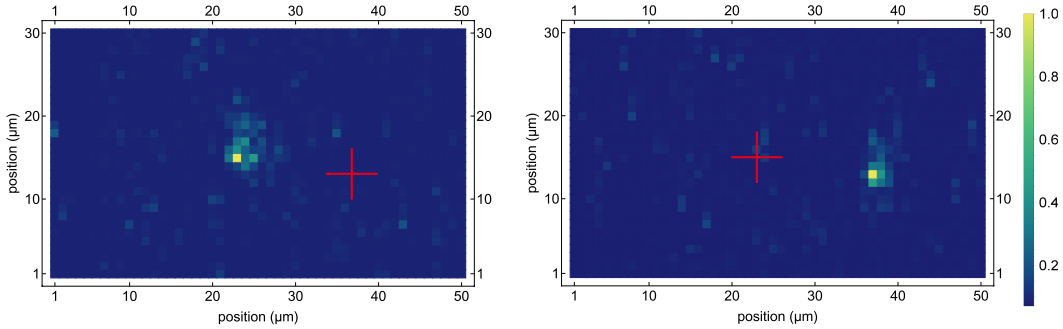

Inaugural-Dissertation

Zur Erlangung des Doktorgrades
der Mathematisch-Naturwissenschaftliche Fakultät
der Heinrich-Heine-Universität Düsseldorf

vorgelegt von

Christian Wellers
aus Düsseldorf

Düsseldorf, August 2022

Aus dem Institut für Experimentalphysik
der Heinrich-Heine-Universität Düsseldorf

Titelbild: Abbildung 12 aus “Controlled Preparation and Vibrational Excitation of Single Ultracold Molecular Hydrogen Ions”, Anhang A.

Gedruckt mit der Genehmigung
der Mathematisch-Naturwissenschaftlichen Fakultät
der Heinrich-Heine-Universität Düsseldorf

Berichterstatter 1: Prof. S. Schiller, Ph.D.

Berichterstatter 2: Prof. Dr. Axel Görlitz

Tag der mündlichen Prüfung: 25.11.2022

Abstract

A novel system for the spectroscopic analysis of single atomic or molecular ions has been developed, set up and put into operation. Its main purpose is to study the molecular hydrogen isotopologues H_2^+, D_2^+ and HD^+, which are theoretically the simplest manageable molecular ions. By measuring different rovibrational transitions and combining the results, important fundamental constants can be determined. In particular, these are the three mass ratios (electron-proton m_e/m_p, electron-deuteron m_e/m_d and deuteron-proton m_d/m_p) and the *Rydberg* constant R_∞.

In order to compete with other measurement methods, high-precision measurements of rovibrational transition frequencies on HD^+, H_2^+ and $D_2^+$with a relative frequency uncertainty $u_r = 10^{-12}$ are required. This is better than the current theoretical relative uncertainty $u_r \approx 7 \cdot 10^{-12}$ [1].

The molecular hydrogen ion cannot be observed directly, which is why a single fluorescent beryllium ion is employed. An ion pair consisting of a single atomic ion and the molecular ion can be laser cooled and is an essential diagnostic tool for mass spectroscopy of the molecular ion or for its state detection. For example, continuous mass spectrometry can be used to observe chemical reactions of the molecular ion with the residual gas in the vacuum chamber.

The currently used method of state-dependent photodissociation is also inconvenient in the case of a single molecular ion and should be replaced by non-destructive detection. A variant based on quantum logic requires a laser system that can cool the oscillation mode of the two-ion system to the ground state. This laser has been built. A second method uses a state-dependent optical dipole force (ODF). The effect of the ODF is calculated for relevant states in HD^+ and possible spectroscopy scenarios are discussed. In particular, a spectroscopy scheme is presented that will allow comparison to the latest results from the ensemble study. It includes the state preparation using radiofrequencies and is based on a non-destructive state detection technique. Further alternatives of spectroscopy are proposed, as well as extensions and improvements to the system, some of which have already been initialised. It turns out that the two-ion quantum system behaves differently from previous works investigating ensemble systems. Those consist of a few ten hydrogen molecules surrounded by a few hundred beryllium ions. In this work, it can no longer be assumed that the ion is in any desired initial state and the state must be specifically prepared. With the ensemble system, it can be statistically assumed that at least some ions are in the desired state.

This work presents an important milestone on the way to high-precision spectroscopy of a single molecular hydrogen ion. A complex apparatus, consisting of an ultra-high vacuum system with integrated particle trap, detectors and beryllium ovens has been

developed from scratch. The laser systems needed for laser cooling and spectroscopy of a single molecular ion have been built and integrated into the system. With the presented system, single HD^+ ions have been trapped, identified and successfully performed spectroscopy for the first time. The apparatus has been analysed for systematic effects using the beryllium ions. A radiofrequency (rf) spectroscopy of the hyperfine transition in the beryllium ground state allows the determination of the magnetic field strength at the ion's location. This is necessary for high precision spectroscopy and provides important insides into the upcoming rf spectroscopy of molecular hydrogen.

Danksagung

An dieser Stelle möchte ich mich bei allen bedanken, die mich während meiner Doktorarbeit auf verschiedenste Weise unterstützt haben.
Mein besonderer Dank gilt Prof. Stephan Schiller, der mir von Anfang an dieses umfangreiche Projekt zugetraut hat. Ich konnte mit ihm alle aufkommenden Probleme ausführlich diskutieren und er stand mir stets mit hilfreichen Ratschlägen zur Seite.
Er hat eine Kooperation mit Prof. Kenneth R. Brown ermöglicht, dem ich an dieser Stelle ebenfalls ganz herzlich danken möchte. Mit seiner tatkräftigen Unterstützung im Labor und seinem Fachwissen hat er zum Erfolg des Projekts beigetragen. Ich konnte zu jeder Zeit meine Ideen mit ihm austauschen.
Außerdem möchte ich all den Kollegen und Bachelor- sowie Masterstudenten danken, ohne die die Realisierung dieses Projekts nicht möglich gewesen wäre. Hier sind besonders Gouri S. Giri, Magnus R. Schenkel, Soroosh Alighanbari, Ulrich Rosowski und Michael G. Hansen zu erwähnen. Ich danke euch für die angenehme Zusammenarbeit.
Bei technischen Fragestellungen konnte ich mich immer auf die schnelle und kompetente Hilfe der Elektronikwerkstatt verlassen. Dafür möchte ich mich bei Peter Dutkiewicz, Rita Gusek und Dmitri Iwaschko bedanken.
Bei meinem langjährigen Studienfreund David Offenberg möchte ich mich für das aufmerksame Korrekturlesen bedanken. Er hatte stets ein offenes Ohr und wir haben bei zahlreichen Wanderungen über das Projekt gesprochen.
Ganz herzlich möchte ich bei meiner Familie, insbesondere bei meinen Eltern, für ihre liebevolle Unterstützung in jeglicher Form bedanken.
Zuletzt bedanke ich mich ganz besonders bei Carina, die mir zu jeder Zeit verständnisvoll den Rücken gestärkt hat. Ich danke dir für deine Geduld an arbeitsintensiven Wochenenden und Abenden und den Motivationsreden in schweren Zeiten. Ohne dich wäre diese Arbeit so nicht möglich gewesen.

Eidesstattliche Versicherung

Ich versichere an Eides statt, dass die Dissertation von mir selbständig und ohne unzulässige fremde Hilfe unter Beachtung der „Grundsätze zur Sicherung guter wissenschaftlicher Praxis an der Heinrich-Heine-Universität Düsseldorf“ erstellt worden ist.

.....

Contents

Abstract i

Danksagung v

Eidesstattliche Versicherung vii

1. Introduction 1
   1.1. The aim of the project . . . 3

2. Particle Trap and Analysis of Particle Motion 7
   2.1. Linear Quadrupole Trap . . . 7
      2.1.1. Classical Ion Motion . . . 9
         2.1.1.1. Pseudo Potential Model . . . 11
   2.2. Eigenmodes of Ion Strings . . . 12
      2.2.1. Multi Species Ion String . . . 15
      2.2.2. Interpretation of the Ion Motion . . . 16

3. The Molecular Hydrogen Ion 17
   3.1. Angular Momentum Coupling Scheme for the HD^+ Molecule . . . 21
   3.2. Interaction with a Magnetic Field . . . 21
   3.3. Transitions of the Homonuclear MHI . . . 22

4. Laser Transitions, Line Shapes and Cooling of a Beryllium Ion 25
   4.1. Level Structure of the Beryllium Ion . . . 25
   4.2. Ion-Photon Interaction and Conservation of Momentum . . . 28
   4.3. Laser Cooling of Trapped Ions . . . 29
      4.3.1. *Doppler* Cooling and Line Spectrum . . . 30

5. System Overview 33
   5.1. Design of the Trap . . . 37
   5.2. Electron Gun . . . 40
   5.3. Electron Beam Detector . . . 41
   5.4. Beryllium Oven . . . 42

5.5. Further Components . . . 43
5.6. Laser Systems . . . 45

6. Experimental Procedures 53
6.1. Beryllium Loading Schemes . . . 53
6.2. Beryllium Trapping . . . 55
6.3. Secular Excitation . . . 55
6.4. Detection with the CCD Camera . . . 57
6.5. Compensation of Stray Charges . . . 58
6.5.1. Beryllium Fluorescence Pattern . . . 59
6.5.2. Radial Compensation - Rough Method . . . 59
6.5.3. Axial Compensation - Rough Method . . . 60
6.5.4. Time-Resolved Fluorescence Detection . . . 60
6.6. Ion Temperature . . . 63
6.7. Mass Spectroscopy . . . 64
6.8. Comments . . . 64
6.8.1. Fluctuation of the Detected Fluorescence . . . 64
6.8.2. Improvement of the Signal to Noise Ratio . . . 65

7. Radiofrequency Spectroscopy of Beryllium 67
7.1. Beryllium Hyperfine Transitions . . . 67
7.2. Recording the Spectra . . . 70
7.3. Measurement of the Applied Magnetic Field Strength . . . 71
7.3.1. Improvement of the Magnetic Field Strength Measurement . . . 73
7.4. Systematic Effects on the Spectrum . . . 73
7.4.1. Frequency Shift due to UV 3 Laser Intensity . . . 74
7.4.2. Effect of the UV 3 and rf Intensity . . . 74
7.4.3. Effect of the Trap Potential . . . 76
7.5. Measurement with the EOM . . . 78

8. Studies on MHI 81
8.1. MHI Trapping . . . 81
8.2. MHI Detection . . . 83
8.3. Chemical Reactions . . . 84
8.4. Concept of State Preparation . . . 86
8.4.1. HD^+ Molecule . . . 86
8.4.2. State Distillation of H_2^+ and D_2^+ . . . 87
8.5. Spectroscopy of a Single Ultracold MHI . . . 88

8.6. Other Ion Species . . . 91
8.6.1. Charge Exchange . . . 92

9. Non-Destructive Detection of the MHI State 93
9.1. Detection by an Optical Dipole Force . . . 93
9.1.1. ODF for $(v = 0, L = 0) \leftrightarrow (v' = 2, L' = 1)$ . . . 95
9.1.2. ODF for $(v = 3, L = 0) \leftrightarrow (v' = 5, L' = 1)$ . . . 96
9.2. Radiofrequency Spectroscopy of HD^+ . . . 97
9.2.1. Fourth Overtone Spectroscopy with a Single Ion . . . 97
9.3. Candidate transitions for Spectroscopy . . . 100

10.Summary 101

11.Outlook 103

Appendix 105

A. Article: Controlled Preparation and Vibrational Excitation of Single Ultracold Molecular Hydrogen Ions 107
A.1. Authors' contributions . . . 107
A.2. Copyright . . . 107

B. Winding Machine and Material Studies 125
B.1. Tests with Materials other than Beryllium . . . 125

Bibliography 129

1. Introduction

Ultracold molecular ions are an important system for testing fundamental physics[1]. When trapped and deeply cooled, high precision molecular spectroscopy allows the determination of fundamental constants of atomic physics, tests of the quantum electrodynamics (QED) [3, 4, 5] and the search for physical effects beyond the Standard Model [6]. Molecular ions are proposed to be a better measure than atomic ions for whether or not the electron-proton mass ratio is constant in time [7, 8, 9, 10, 11, 12].

Molecular ions usually cannot be laser-cooled directly due to the lack of cycling transitions as a consequence of complex internal structure of the molecular ions due to the multitude of rovibrational levels. They can be efficiently cooled to millikelvin temperatures by sympathetic cooling by co-trapped atomic ions. This technique can be used over a wide mass range of molecular ions from 1 u [13] to several thousand u [14] and used to cool one or many ions. Example molecular ions that have been trapped include HD^+, molecular nitrogen N_2^+ [15], CaH^+ [16, 17] and SiO^+ [18].

As shown by *Dehmelt* [19, 20, 21] the environment of a single trapped atomic ion can be controlled very well and nondestructive internal state detection is feasible. Nondestructive state detection for a single molecular ion was first demonstrated with an atomic ion and molecular ion crystal of Mg^+ - MgH^+ [22]. This technique has now been demonstrated on two additional atom-ion pairs, Ca^+ - CaH^+ [23] and Ca^+ - N_2^+ [24]. Different methods of non-destructive internal state detection have been successfully demonstrated including coherent motional excitation of the system [25, 26] or quantum logic spectroscopy [27, 28].

In this work, I constructed an apparatus capable of performing spectroscopy on a single molecular hydrogen ion (MHI) in a well-defined quantum state. MHI is a three-body system consisting of two single positively charged nuclei and one electron (Figure 1.1). It has been previously shown in the Schiller group and other groups that very accurate experimental and theoretical determinations of MHI transition frequencies are possible, with a relative precision of $10^{-11} - 10^{-12}$ [3, 29, 5, 1]. Figure 1.2 shows the HD^+ energy spectrum with its innumerous rotational and vibrational states in the electronic ground state. Also illustrated is an example of a spectroscopy scheme and

[1] This introductory part is found in a similar form in the appendix (Appendix A) of this thesis and the publication [2] within it.

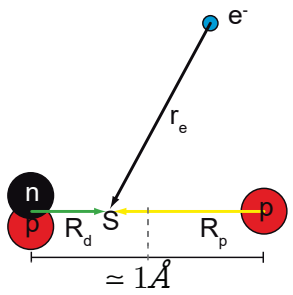

Figure 1.1.: Schematic sketch of the three-body problem for the heteronuclear HD^+ molecule. The point-like electron is located at a distance r_e from the centre of mass S, which does not coincide with the geometric centre. The distance between the two nuclei is $R \simeq 1.0\,\text{Å}$.

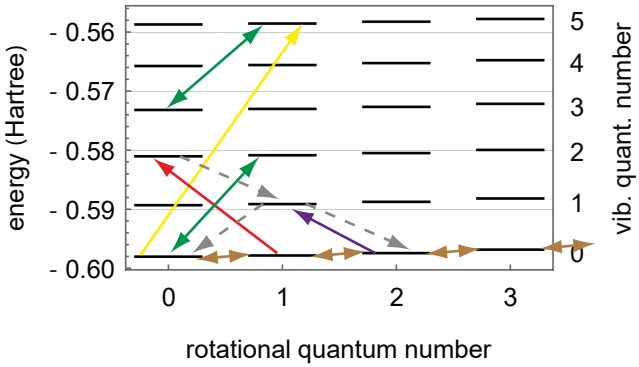

Figure 1.2.: HD^+ energies and ($v = 0$, $L = 0$) state preparation: The QCL (purple, 5.5 µm) depopulates $L = 2$, state $L = 1$ is depopulated with 2.7 µm radiation (red). Decay channels due to spontaneous emission are dashed grey. The initial $(0,0)$ and final $(5, 1)$state of the spectroscopy laser (1.15 µm, yellow) are detected with an optical dipole force (green). In the vibrational ground state, the rotation levels are coupled by the blackbody radiation (brown). States $(0, L \geq 3)$ are ignored due to their short lifetime. Energies by [30, 31].

the necessary state preparation (details in Section 8.4.1). It is an eminent goal of both theoretical and experimental groups, ours included, to improve the precision of the frequency determinations. Indeed, it has been forecast that a relative inaccuracy of 10^{-17} can be achieved experimentally [10, 11].

Prior work in our group used multiple MHIs held in a weakly confining trap (in the following referred to as "trap 1"). The apparatus that I constructed contains a new strongly confining single-ion trap ("trap 2"). Both traps are located in the same laboratory and we will use the same laser resources in the future. This enables comparison of MHI frequencies measured in both traps and the determination and removal of systematic errors.

1.1. The aim of the project

The new generation of table-top spectroscopy experiment is intended to be the basis for ultra-high resolution and ultra-high precision spectroscopy of a single ion. It is intended to move from the investigation of a few 10 to few 100 trapped MHIs, as has been done successfully by our group for more than 20 years, to the new regime of a single molecular ion. We expect the ion to be controlled much better than in trap 1, thus allowing us to reach the extreme precision of 10^{-17}. The conventional method of internal state detection by photodissociation [32] is unsuitable for single ions, because of its very slow spectral data acquisition. In addition, single molecular ion experiments are more susceptible to stray electric fields and constant refilling of the trap by electron impact ionization will require additional tuning of electric fields between experiments. On the other hand, after the electric fields are compensated the single ion or a string of ions at the node of the electrical potential will not experience the driven trap motion any more, known as micromotion. For a cluster of ions, micromotion is unavoidable and results in a systematic error that prevents us from achieving a much more precise measurement of molecular transition frequencies.

The proposed experiments focus on the three non-radioactive isotopologues H_2^+, D_2^+ and the heteronuclar HD^+, and a general method is required, which enables trapping, cooling and the spectroscopy of a light molecule.

With a strongly confining trap potential, it is possible to perform spectroscopy in the *Lamb-Dicke* regime where the ion is confined in a space smaller than the wavelength of the addressing light. The *Lamb-Dicke* regime eliminates the frequency shift due to the first-order *Doppler* effect and it also enables the desired non-destructive readout methods of the quantum state.

Different non-destructive methods can be used. These methods all rely on coupling the internal state of the molecular ion to the motion and then reading out the motion by coupling the motion to the atomic ion. Quantum logic spectroscopy relies on starting from the ground state of motion and adding one single excitation of motion via the molecular transition. One can also use and optical dipole force (ODF) to conditionally displace the motion at a larger scale. Quantum logic spectroscopy requires ground-state cooling while ODF measurements require only achieving the *Doppler* temperature of beryllium, with an average of five excitations in the axial vibrational mode (Section 6.6). Since, the ODF has heating rates of more than 20 phonons/ms (Section 9.1), it should be detectable with a CCD camera. Both methods require low background ion heating rates to achieve good signal to noise but the ODF is also less sensitive to this noise source.

The cooling process of the molecular ion is implemented with a laser. In principle, the MHIs could also be cooled using a cryostat, but this would increase the complexity of these experiments. The system presented here is intended to be the basis for later, possibly more complex, experiments.

Since the MHI is a very light molecule of 2-4 u, the atomic ion should be similar in weight. The lightest atomic ion that can be cooled with a laser is beryllium (9 u), whose fluorescence can be observed with a photon multiplier tube (PMT) or a CCD camera. For a two-ion crystal with mixed species, a mass ratio smaller than a factor of five is still good for sympathetic cooling [33]. Thus, the new system must be able to handle beryllium as well as MHI.

Beryllium ions are critical for the molecular ion measurements and the apparatus is designed with this requirement in the forefront. Atomic beryllium is vaporised in a specially designed oven, photoionised with a home-made laser system or an electron gun by electron impact, stored in a newly designed trap and laser cooled, observed with the help of a PMT and a camera, and used as a detection tool for the trapping and spectroscopy of the MHI. For this purpose, a custom-made ultra-high vacuum chamber with a small volume and six optical axes for laser access is necessary.

In addition, the new apparatus has been designed to enable rf spectroscopy of trapped molecular ions with an rf antenna. The antenna has been developed to have a wide frequency range and to generate an optimised alternating magnetic field at the ion's location in the trap. It enables the investigation of a further class of transitions that are difficult to directly access with lasers.

The system is expected to fulfil the following criteria:

- Small volume tabletop system that can store a single molecular ion and an atomic beryllium ion simultaneously.

- Controlled inlet of various neutral gases and their ionisation capability.
- A particle trap with a strong confining potential and very good optical access for the different laser systems.
- Detection of the beryllium fluorescence.
- Determination of the stored ion species and number including a time-efficient detection of their internal and motional state.
- The precise manipulation of the internal and motional state of the atomic and molecular ion.
- Implementation of rf spectroscopy with a broadband antenna whose emitted magnetic field is optimised at the ion's location.
- Controllable environment: the magnetic field strength in the storage volume of the trap must be adjustable and compensated to less than a few milligauss.
- Enabling convenient maintenance routines: a modular design ensures good accessibility and maximum flexibility when adapting the spectroscopic scheme.

2. Particle Trap and Analysis of Particle Motion

The centrepiece of the system is the rf ion trap or *Paul* trap, which allows ions to be stored based on electric fields. In contrast to the Penning trap, no external magnetic fields are required. This is particularly important for precision spectroscopy of an MHI, as a magnetic field would shift the energies of its states. In any case, this must be avoided.

In order to achieve a three-dimensional potential minimum for the ion due to electric fields, *Wolfgang Paul* came up with the *Nobel* Prize-winning idea of using an electric quadrupole potential for the radial confinement and additionally superimposing an axial confinement. The latter is described in numerous textbooks [34, 35, 36, 37, 38].

2.1. Linear Quadrupole Trap

Wolfgang Paul's patent describes the ideal quadrupole trap with hyperbolically shaped electrode cross section [39]. The idea can be technically simplified with cylindrical electrodes. This simplification causes a modified condition for the radius r_0, which is the shortest distance between the electrode surface and the centre of the trap. The so-called linear *Paul* trap also produces a quadrupole potential [40].

In general, the ideal (pure) quadruple potential

$$\phi_{\text{quad}} = \mathrm{f}[t] \cdot \left(\alpha x^2 + \beta y^2 + \gamma z^2\right) + \delta \tag{2.1}$$

can be expressed mathematically in *Cartesian* coordinates by the four parameters α to δ and the important quadratic dependence with respect to the origin.

The parameters α, β and γ scale the three basis directions individually, while $\mathrm{f}[t]$ is an overall arbitrary periodic prefactor. Other possible potentials are included in δ. As

a boundary condition for a potential minimum the *Laplace* equation

$$\Delta\phi = 0 \tag{2.2}$$

$$= 2\mathrm{f}[t]\left(\alpha+\beta+\gamma\right) \tag{2.3}$$

has to be fulfilled. The term inside the bracket of equation 2.3 has to be zero, which is not possible for pure static electric fields [41]. The most simple and therefore common solution are $\alpha = -\beta, \gamma = 0$ or $\alpha = \beta, \gamma = -2\alpha$. In addition, the axial confinement leads to a radial defocusing potential introduced by the parameter ϵ. This electric potential

$$\phi_{\mathrm{quad}} = \mathrm{f}[t]\cdot\left(x^2-y^2\right)+\left[\gamma z^2+\epsilon\left(x^2+y^2\right)\right]+\delta \tag{2.4}$$

can be generated by the trap shown in Figure 5.8. Opposite electrodes are contacted in pairs. Since the applied voltage for each pair is 180° out of phase, the trap potential is composed of the sum of the voltages. It is called "symmetrical trap configuration". Assuming that the voltage amplitudes for both pairs are identical, the trap voltage U_{rf} can be measured as the peak-to-peak voltage of one pair. It is easily doable with the monitor output of the trap electronics.

For this type of trap, the parameter $\mathrm{f}[t]$ and δ can be determined using the known potential's magnitude: The maximum voltage U_{rf} is given as the potential difference between the two electrode surfaces $\left|\phi_1\left(x=r_0, z=0\right)\right| - \left|\phi_2\left(y=r_0, z=0\right)\right|$, from which, together with equation 2.4, the parameter

$$\mathrm{f}(t=0, z=0) = \left|\frac{U_{\mathrm{rf}}}{2\cdot r_0^2}\right| \tag{2.5}$$

can be concluded. Further electric potentials can be added to the quadrupole potential because of the superposition principle. Therefore, an ion can be trapped in three spatial dimensions. In order to be able to implement the so-called sideband cooling later on, an axial harmonic trap potential is required. It can be shown that the potential of two tip-shaped electrodes, positioned symmetrically around the trap centre, has a quadratic characteristic (Figure 5.10). The resulting defocusing potential of the tip-shaped or "end cap" electrode in x- and y- direction has half the magnitude of the axial confinement U_{ec}. This results finally in the trap's electric potential

$$\phi_{\mathrm{trap}} = \left(\frac{U_{\mathrm{dc}}+U_{\mathrm{rf}}\cos\left[\Omega t\right]}{2r_0^2}\left(x^2-y^2\right)\right)+\left[\kappa U_{\mathrm{ec}}z^2-\frac{\kappa U_{\mathrm{ec}}}{2}\left(x^2+y^2\right)\right]+\underbrace{\boldsymbol{E}\cdot\boldsymbol{r}}_{=0} \tag{2.6}$$

with the trap drive frequency $\Omega = 2\pi\widetilde{\Omega}$ and the same notation as in [42]. The trap geometry due to the end caps is hidden in the proportionality factor $\kappa = \frac{d^2}{dz^2}\left(\phi_{\mathrm{ec}}/U_{\mathrm{ec}}\right)_{z=0}$, the so-called geometry parameter. It can be determined from the axial potential $\phi_{\mathrm{ec}} = \kappa U_{\mathrm{ec}} z^2$. A quadratic fit to the simulation data close to the origin results in a theoretical geometric parameter $\kappa_{\mathrm{theo}} = 12572\,\mathrm{m}^{-2}$ (Figure 5.10).Space charges lead to an additional static electric field $\boldsymbol{E}$. It can be compensated to zero by additional compensation electrodes.

2.1.1. Classical Ion Motion

An ion with charge Q and mass m located in the trap is accelerated

$$\ddot{x} = -Q \cdot \left(\frac{U_{\mathrm{dc}} + U_{\mathrm{rf}} \cos\left[\Omega t\right]}{m r_0^2} - \frac{\kappa U_{\mathrm{ec}}}{m} \right) x \tag{2.7}$$

$$\ddot{y} = -Q \cdot \left(\frac{-U_{dc} - U_{rf} \cos\left[\Omega t\right]}{m r_0^2} - \frac{\kappa U_{ec}}{m} \right) y \tag{2.8}$$

$$\ddot{z} = -2Q \cdot \frac{\kappa U_{ec}}{m} z$$

by the trap's potential in the direction $u = \{x, y\}$. A force $F_u = m \cdot \ddot{u} = -Q\frac{\partial \phi_{\mathrm{trap}}}{\partial u}$ is acting.

These differential equations are similar to *Mathieu* functions

$$\frac{d^2 u}{d\tau^2} = -\left(a_u - 2q_u \cos\left[2\tau\right]\right) u \tag{2.9}$$

with $\tau = \frac{\Omega}{2} t$, $d\tau = \frac{\Omega}{2} dt$ and $m \cdot \ddot{u} = m \cdot \frac{\Omega^2}{4} \frac{d^2 u}{d\tau^2}$, so the equations of motion can be rewritten as:

$$\frac{d^2 u}{d\tau^2} = \left(\underbrace{\frac{-4\left(\pm U_{\mathrm{dc}} + \kappa r_0^2 U_{\mathrm{ec}}\right) Q}{m r_0^2 \Omega^2}}_{a_{x,y} :=} + 2 \underbrace{\frac{\mp 2 Q U_{\mathrm{rf}}}{m r_0^2 \Omega^2}}_{q_{x,y} :=} \cos\left[2\tau\right] \right) u \tag{2.10}$$

$$\frac{d^2 z}{d\tau^2} = \underbrace{\frac{8\kappa Q U_{\mathrm{ec}}}{m\Omega^2}}_{a_z :=} z = \left(2a_{\mathrm{ec}}\right) z \tag{2.11}$$

The a_u parameter, defined in equation 2.10, consists of two terms, the quadrupole solution and a term related to the end cap $a_{\mathrm{ec}} = \frac{4\kappa Q U_{\mathrm{ec}}}{m\Omega^2}$. The q_u parameter, $q_y = -q_x$ and $q_z = 0$, is the same whether with or without applied end cap voltage U_{ec}.

In the case that no dc voltage ($U_{\mathrm{dc}} = 0$) is applied to the blade electrodes, the solution of the stable ion's trajectory is visualised in Figure 2.1 in terms of q_u and a_u, where the

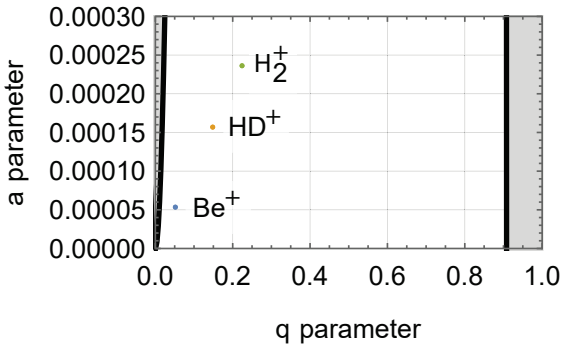

Figure 2.1.: *Mathieu* stability diagram: The a and q parameter for the species Be^+, HD^+ and H_2^+ for a trap frequency $\widetilde{\Omega} = 35\,\mathrm{MHz}$ ($U_{\mathrm{rf}} = 100\,\mathrm{V}$, $U_{\mathrm{ec}} = 3\,\mathrm{V}$). The stability region according to *Mathieu* is marked white.

symmetry of the *Mathieu* function has been used. In the axial direction the motion is also bound.

A general solution for the *Mathieu* function 2.9 follows from the *Floquet*-theorem [36]

$$u(\tau) = T\exp\left[\mu\tau\right]\sum_{n=-\infty}^{\infty} C_{2n}\exp\left[2in\tau\right] + T'\exp\left[-\mu\tau\right]\sum_{n=-\infty}^{\infty} C_{2n}\exp\left[-2in\tau\right] \tag{2.12}$$

$$\overset{\mu=\pm i\beta_u}{=} \left(T+T'\right)\sum_{n=-\infty}^{\infty} C_{2n}\cos\left[\left(2n\pm\beta_u\right)\frac{\Omega}{2}t\right] + i\left(T-T'\right)\sum_{n=-\infty}^{\infty} C_{2n}\sin\left[\left(2n\pm\beta_u\right)\frac{\Omega}{2}t\right], \tag{2.13}$$

with the integration constants $T\left(u_0, \dot{u}_0, \tau_0\right)$ and $T'\left(u_0, \dot{u}_0, \tau_0\right)$, which depend on the initial values $u_0, \dot{u}_0, \tau_0$ and the independent constants C_{2n} and μ. The latter are functions of the a_u and q_u parameter. Since an ion trap is a device that stores ions for a long time ($\tau \to \infty$), the ions are not lost because of hitting any electrodes ($u_{\max} < r_0$) and the ion path is periodic. If $\mu = \pm i\beta$ is an imaginary and β a rational fraction, the solution is periodic and stable. The constants C_{2n} follows by inserting equation 2.13 into 2.6

$$C_{2n+2} - D_{2n}C_{2n} + D_{2n-2} = 0$$

$$D_{2n} = \frac{a_u - \left(2n+\beta_u\right)^2}{q_u}$$

leading to $D_0 = \left(C_2 + C_{-2}\right)/C_0 = \left(a_u + \beta_u\right)^2/q_u$ [43].

The radial ion trajectory is a function of the secular frequencies

$$\omega_{u,n} = \left(n \pm \beta_u/2\right)\Omega, \tag{2.14}$$

while the spectra of the motion is determined by β_u that is a function of the parameters a_u and q_u.

Since the magnitudes of C_{2n} decrease for increasing n, high order frequencies are not relevant and $\beta_u\left(a_u, q_u\right)$ is defined as [36]

$$\beta_u^2 = a_u + \frac{q_u^2}{\left(\beta_u+2\right)^2 - a_u - \frac{q_u^2}{\left(\beta_u+4\right)^2 - a_u - \frac{q_u^2}{\left(\beta_u+6\right)^2 - a_u - \cdots}}} + \frac{q_u^2}{\left(\beta_u-2\right)^2 - a_u - \frac{q_u^2}{\left(\beta_u-4\right)^2 - a_u - \frac{q_u^2}{\left(\beta_u-6\right)^2 - a_u - \cdots}}}. \tag{2.15}$$

2.1.1.1. Pseudo Potential Model

In general, equation 2.15 can be used iteratively to calculate the β-parameter. Starting with a test value, the newly calculated value is re-inserted until the difference between the old and the new value is small. Since the trap will be operated in a regime $q_u < 0.4$ an effective potential approximation can be used to calculate β_u, which is accurate within 1 % [44]. The idea is to split the oscillation in the ion's position u into a fast and a slow oscillation [45, 46, 47, 38],

$$u\left(\tau\right) = U\left(\tau\right) + \delta\left(\tau\right), \tag{2.16}$$

assuming that the amplitude δ of the ion's displacement due to the fast driving rf field is much smaller then the larger amplitude U with its comparable slow displacement. Hence, $\delta \ll U$ and $\ddot{\delta} \gg \ddot{U}$ holds. Equation 2.9 can be approximated by

$$\frac{d^2\delta}{d\tau^2} = -\left(a_u - 2q_u\cos\left[2\tau\right]\right)U. \tag{2.17}$$

If $a_u \ll q_u$ and assuming that the slow oscillation U is nearly constant over one oscillation period of the fast driving rf field, it can be further simplified. In this case, integration leads to $\delta = -\frac{1}{2}Uq_u\cos\left[2\tau\right]$. The ion's position (eq. 2.16) can be rewritten as

$$u\left(\tau\right) = U\left(\tau\right) - \frac{1}{2}U\left(\tau\right)q_u\cos\left[2\tau\right]$$

and substituted into equation 2.9. Averaging over one rf cycle, $\left\langle\ddot{\delta}\right\rangle_{\mathrm{rf}} = 0$, leads to

$$\left\langle \frac{du^2}{d\tau^2} \right\rangle_{\mathrm{rf}} = \left\langle \frac{dU^2}{d\tau^2} \right\rangle_{\mathrm{rf}} = \frac{1}{\pi}\int_0^{\pi} \left(-a_u U + 2q_u U \cos[2\tau] + \frac{a_u q_u U}{2}\cos[2\tau] - q_u^2 U \cos^2[2\tau] \right) d\tau$$
$$= -\left(a_u + \frac{q_u^2}{2}\right) U .$$

It describes a trapped ion's harmonic oscillation

$$\frac{dU(t)^2}{dt^2} = -\omega_{u,0}^2 U(t) = -\frac{\Omega^2}{4}\left(a_u + \frac{q_u^2}{2}\right) U(t) \tag{2.18}$$
$$\omega_{u,0}^2 = \frac{\Omega^2}{4}\left(a_u + \frac{q_u^2}{2}\right). \tag{2.19}$$

We obtain β using equation 2.14

$$\beta_u = \sqrt{a_u + \frac{q_u^2}{2}}.$$

The ion's classical motion in a first order approximation of the trajectory is given by

$$u(t) \approx u_{\max}\left(1 + \frac{q_u}{2}\cos[\Omega t]\right)\cos\left[\omega_{u,0} t + \varphi\right],$$

assuming $C_{\pm 4} \simeq 0$. The phase φ is determined by the initial condition of the ion [48].

Therefore, the ion's trajectory is a combined motion of a slow oscillation with the secular frequency $\omega_{\mathrm{sec}} = \omega_{u,0}$ and an imposed fast oscillation with frequency Ω originating from the rf drive. The latter is the so-called micromotion that has a factor $\frac{q_u}{2}$ smaller amplitude. Its phase depends on the direction u of the trap's coordinate system. For $u = x$ the q-parameter is negative and the oscillation is 180° out of phase, while it is in phase for the y-direction (compare eq. 2.10).

2.2. Eigenmodes of Ion Strings

The previous description of the particle trajectories is based on the assumption that there is only one single particle in the *Paul* trap. For the MHI's spectroscopy, at least two ion species, namely MHI and beryllium, with one or more particles each are needed. The particularly interesting case without micromotion is when N ions are aligned like a string on the trap axis. This is the case if the radial confinement satisfies $\omega_{0,x} = \omega_{0,y} > 0.73 N^{0.86} \cdot \omega_{0,z}$ [49] and the temperature (and thus the kinetic energy) of the particles is small. The latter is typically achieved by laser cooling (Section 4.3).

Each ion $m = 1, \ldots, N$ can oscillate around its equilibrium position $u_m^{(0)}$ in all three spatial directions $u = \{x, y, z\}$ with the (small) displacement $q_m^{(u)} = u_m - u_m^0$.

The radial displacement will be very small because of the strong radial confinement (stiff limit, $q_m^{(x,y)} \approx 0$), while it will be substantial along the trap axis (soft limit). Since the *Coulomb* interaction extends over the entire particle string, the ions can oscillate collectively. The description is based on [50, 51].

In section 2.1.1.1 it is shown that the particle motion in the trap's potential corresponds to that of a harmonic oscillator for the different spatial directions with the three constants $\omega_{\mathrm{sec},u} = \omega_{0,u}$ (without micromotion). If N particles of the same mass M are stored in the trap, the repulsive *Coulomb* potential ϕ_{Coulomb} must be considered in addition to the pseudopotential ϕ_{pseudo} of the trap:

$$V = \phi_{\mathrm{pseudo}} + \phi_{\mathrm{Coulomb}} = \sum_{m=1}^{N} \frac{1}{2} \frac{M}{Q} \sum_{u=x,y,z} \omega_{m,u}^2 u_m^2 + \sum_{\substack{m,n=1 \\ m \neq n}}^{N} \frac{Q^2}{8\pi\varepsilon_0} \frac{1}{|\boldsymbol{r}_n - \boldsymbol{r}_m|}$$

$$= \frac{1}{2} \frac{M}{Q} \sum_{m=1}^{N} \left[\omega_{0,x}^2 x_m^2 + \omega_{0,y}^2 y_m^2 + \omega_{0,z}^2 z_m^2 \right] + \tag{2.20}$$

$$\frac{1}{2} \sum_{\substack{m,n=1 \\ m \neq n}}^{N} \frac{e^2}{4\pi\varepsilon_0} \frac{1}{\sqrt{(x_n - x_m)^2 + \left(y_n - y_m\right)^2 + (z_n - z_m)^2}} \tag{2.21}$$

Only the relevant, singly charged, particles with $Q = 1 \cdot e$ are considered, where the position vector $\boldsymbol{r}_m = \left(x_m, y_m, z_m\right)^\top$ of particle m is given by the components u_m. From the condition that in the equilibrium position no force $\boldsymbol{F} \propto -\nabla V = 0$ acts on the ions, it follows that the derivative of the potential

$$\left[\frac{\partial V}{\partial u_m} \right]_{u_m = u_m^{(0)}} = 0 \tag{2.22}$$

must vanish.

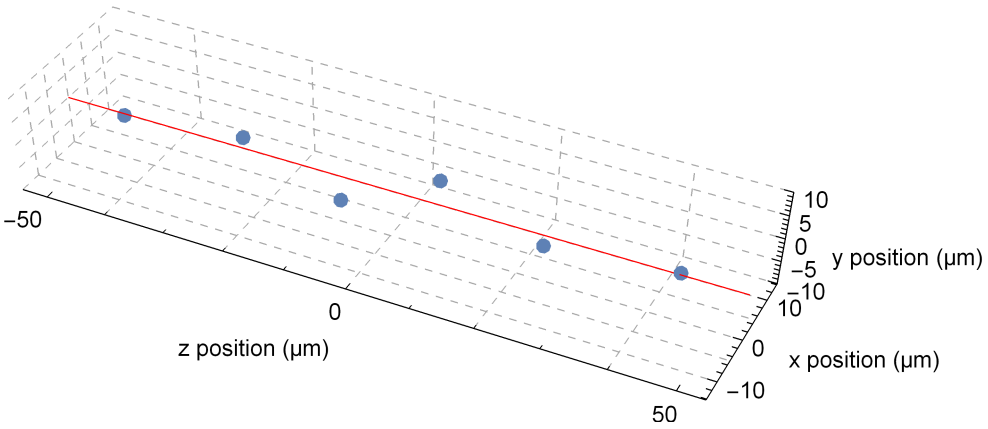

Figure 2.2.: Equilibrium positions in respect to the trap center (origin) for six beryllium ions for typical trap parameters ($U_{\mathrm{ec}} = 3\,\mathrm{V}$, $U_{\mathrm{rf}} = 32\,\mathrm{V}$ corresponding to $\omega_{\mathrm{Be},z} \approx 2\pi \cdot 0.18\,\mathrm{MHz}$ and $\omega_{\mathrm{Be},x} \approx 2\pi \cdot 0.26\,\mathrm{MHz}$). A typical three-dimensional zigzag arrangement with ion displacements from the trap axis (red) is shown.

The second-order *Taylor* expansion of the potential is

$$\begin{aligned} V' = &\sum_{m=1}^{3N} \left(\underbrace{V(u_m^0)}_{\text{const.}} + \underbrace{\left[\frac{\partial V}{\partial u_m}\right]_{u_m=u_m^{(0)}}}_{\equiv 0} \cdot \left(u_m - u_m^0\right) \right) + \\ &\sum_{m=1}^{3N} \frac{1}{2} \left(\left[\frac{\partial^2 V}{\partial^2 u_m}\right]_{u_m^{(0)}} \cdot \left(u_m - u_m^0\right)^2 \right) + \\ &\frac{1}{2} \sum_{\substack{m,n=1 \\ m\neq n}}^{3N} \left(\left[\frac{\partial^2 V}{\partial u_m \partial u_n}\right]_{u_m^{(0)}} \cdot \left(u_m - u_m^0\right)\left(u_n - u_n^0\right) \right) \end{aligned} \tag{2.23}$$

$$\begin{aligned} V = &\frac{1}{2} \sum_u \sum_{m,n=1}^{N} \left[\frac{\partial^2 V}{\partial u_n \partial u_m}\right]_{u_m^{(0)}} q_n^{(u)} q_m^{(u)} \\ \equiv &\frac{1}{2} \sum_u \sum_{m,n=1}^{N} A_{n,m}^{(u)} q_n^{(u)} q_m^{(u)} . \end{aligned} \tag{2.24}$$

There is no change in the oscillation frequencies due to the contribution of the constant potential of the 0th order.

The matrix $A_{n,m}^{(u)}$ has $p = 1, \ldots, N$ eigenvalues $\left(\omega_u^{(p)}\right)^2$, which together with the corresponding eigenvectors $\boldsymbol{b}^{(p)} = \left(b_1^{(p)}, \ \ldots, \ b_N^{(p)} \right)^T$ satisfy the eigenvalue equation $A\boldsymbol{b} = \omega^2 \boldsymbol{b}$. The values $\omega_u^{(p)}$ are the ion string's eigenmode frequencies. The "eigenmodes" or "normal modes" defined by $Q_p(t) = \sum_{m=1}^{N} b_m^{(p)} q_m(t)$ can be therefore derived from the components of the eigenvector leading to the amplitudes and phases of the particles' oscillatory motion relative to each other.

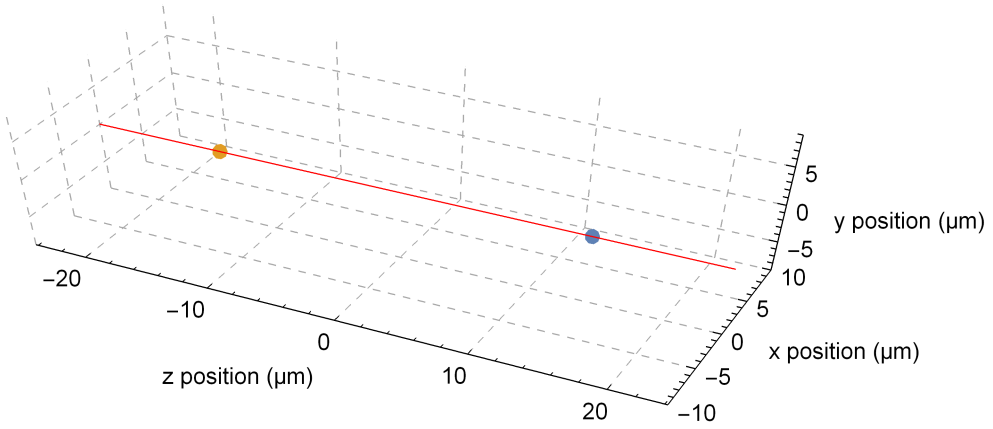

Figure 2.3.: Equilibrium position of an HD^+ ion (orange) cotrapped with a beryllium ion (blue) on the trap's center. The trap axis shown in red. In this two-ion case, the equilibrium positions are on the trap axis (one-dimensional arrangement) for the same parameters as in Figure 2.2.

With a computer software, the equilibrium positions[1] $u_m^{(0)}$ can be quickly determined for different numbers of particles N (Figure 2.2). The example shows that for the selected trap voltage $U_{\mathrm{rf}} = 32\,\mathrm{V}$, the ion positions no longer form a one-dimensional string, but arrange themselves three-dimensionally. The chosen viewing angle results in a typical zigzag pattern.

2.2.1. Multi Species Ion String

It is clear that in the case of the extension to different species, it must be possible to stably trap each individual ion species. This limits the mass range of the species to be trapped, assuming that only singly charged ions are considered. Figure 2.3 shows such a two-ion arrangement, which, with the same parameters as above, is here a one-dimensional arrangement. The extension according to [52] of the method presented in Section 2.2 to particles with different mass M_m localised at $\boldsymbol{r}_m$ leads to the potential

$$V = \frac{1}{2}\sum_u \sum_{m=1}^{N} \frac{M_m}{Q}\omega_{0,u}^2 u_m^2 + \sum_{\substack{m,n=1 \\ m\neq n}}^{N} \frac{e^2}{8\pi\varepsilon_0}\frac{1}{|\boldsymbol{r}_n - \boldsymbol{r}_m|}$$

for equally charged particles $Q = 1$.

The trap frequencies now depend on the arrangement of the species, which quickly leads to very complicated individual spectra, even for small numbers of ions. Similar

[1] Wolfram Mathematica command:
NMinimize[V, Flatten[u3N], Method → "SimulatedAnnealing", AccuracyGoal → ∞, PrecisionGoal → ∞][[2]]; With the potential V (Equation 2.20) and u3N = Array[ion, {N, 3}]; is a placeholder for the 3 coordinates u of the equilibrium position for N ions.

to Section 2.2, the eigenvalues of the matrix corresponding to the squared mode frequencies have to be determined. For a simpler treatment, first the sum in the potential energy is replaced by the new coordinate index $m = 1,\ldots,3N$, i.e. $\sum_u \sum_{m=1}^{N} \rightarrow \sum_{m=1}^{3N}$, and then the second derivative of the potential $\left[\frac{\partial^2 V}{\partial u_n \partial u_m}\right]_0$ at the equilibrium positions is evaluated. For this procedure it is advantageous to use mass-weighted coordinates $u'_i = \sqrt{M_i}\,u$, where the dash indicates the weighted quantities.

2.2.2. Interpretation of the Ion Motion

For example, three stored beryllium ions ($M_m = M_{\mathrm{Be}}, \omega_{m,u} = \omega_{\mathrm{Be},z}$, Figure 6.4b) can oscillate in the axial direction ($u = z$) in three different ways: Their three dimensionless equilibrium positions are $u^0_{1,z}/l \approx -1.07717$, $u^0_{2,z}/l = 0$ as well as $u^0_{3,z}/l \approx 1.07717$. Here, the scaling factor

$$l^3 = \frac{e^2}{4\pi\varepsilon_0}\frac{1}{M_{\mathrm{Be}}\omega^2_{\mathrm{Be},z}} \tag{2.25}$$

is used [50]. For this special case the squared frequency $\omega^2_{\mathrm{Be},z}$ can be extracted easily from the matrix $A^{(u)}_{n,m}$. Now the three eigenvalues $\mu_1 = 1$, $\mu_2 \approx 3.0$ and $\mu_3 \approx 5.8$ are in units of this squared frequency. Hereby the eigenvectors are

$$\boldsymbol{b}^{(1)}_z = \begin{pmatrix} 0.57735 \\ 0.57735 \\ 0.57735 \end{pmatrix}, \boldsymbol{b}^{(2)}_z = \begin{pmatrix} -0.707107 \\ 0 \\ 0.707107 \end{pmatrix}, \boldsymbol{b}^{(3)}_z = \begin{pmatrix} 0.408248 \\ -0.816497 \\ 0.408248 \end{pmatrix}.$$

For the first case ($p = 1$), the amplitudes and phases of the three ions are the same. So they perform a common movement in the same direction. The relative distances of the ions are preserved during the oscillation. The lowest oscillation frequency of the string $\omega^{(1)}_z = \sqrt{1}\omega_{\mathrm{Be},z}$ corresponds to the centre of mass (COM) oscillation frequency. It is equivalent to that of the single ion in the axial trap potential.

Mode $p = 2$ is called the "breathing mode". Here, the two outer ions oscillate with a frequency $\sqrt{3} \approx 1.73$ times higher compared to $p = 1$. Their amplitude has the same magnitude but is 180° out of phase. The middle ion is at rest.

If the outer ions move with the same amplitude and phase, the middle ion must compensate for this movement with an opposite, double amplitude, since the string's COM does not move ($p = 3$). The frequency of this antisymmetric stretch oscillation is $\sqrt{5.8} \approx 2.4$ times higher than $\omega^{(1)}_z$.

An example of a mixed string is discussed in detail in Section 8.2 and 8.6.1.

3. The Molecular Hydrogen Ion

The molecular hydrogen ion is composed of two positively charged nuclei that are bound in the ground state by a shared electron (Figure 1.1). The nuclei can be the baryons p, d or t. For practical reasons, only the stable homonuclear molecular ions H_2^+ and D_2^+ and the heteronuclear HD^+ are considered below.

This quantum mechanical three-body problem cannot be solved exactly, so different approximations have to be made depending on the required accuracy and precision. Physicists have been developing a mathematical model of the MHI for more than 100 years.

A very simple picture can be used to illustrate that the two nuclei are surrounded by the electron similarly to an atom: If the two protons of a helium ion are separated, then the electron moves in the field of the two charge centres and can be in different electronic states in a similar way to the helium ion (Figure 3.1). In the electronic ground state $1s\sigma$, the attractive interaction of the electron between the two nuclei dominates the repulsive *Coulomb* part, resulting in an energetically favoured, stably bound molecule. A contour plot is shown in Figure 3.2. In contrast to the helium ion, the two nuclei can now oscillate against each other and rotate around the common COM. Similarly to the quantum mechanical oscillator and rotator, the energy of the molecule is described by the quantum numbers v and L respectively (Figure1.2 and 3.4).

Nowadays, an effective *Schrödinger* equation with an effective Hamiltonian is used to calculate the energy levels of the MHI. This non-relativistic and thus non-*Lorentz* invariant approach (non-relativistic quantum electrodynamics for light hydrogenic ions [53], NRQED) is easier to handle than the relativistic equations of quantum electrodynamics. The effective Hamiltonian is an extended non-relativstic Hamiltonian for the *Coulomb* potential by adding further corrections. Then the properties of the bound state are calculated by a power series expansion according to the small parameter α

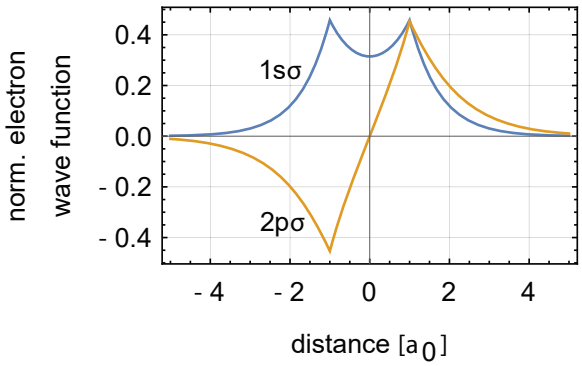

Figure 3.1.: Normalised electron wave functions for the molecular hydrogen ion in the clamped nuclei approximation. For the computation, the intranuclear nuclei distance $R \approx 2$ is chosen, as it minimizes the electronic energy corresponding to the equilibrium intranuclear distance of the nuclei. The exponential decrease is the classic dependence of the wave function at large distances from the nuclei.

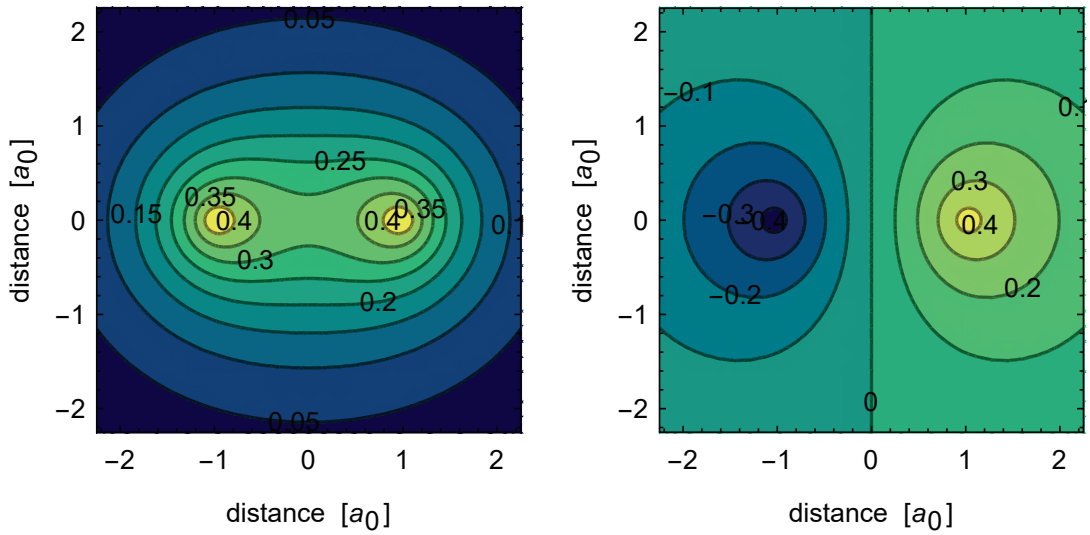

Figure 3.2.: Contour plot of the $1s\sigma$ ground (left) and $2p\sigma$ excited state (right). Since the considered states are σ-states ($m = 0$), they are axially symmetric around the internuclear axis. The positively charged nuclei are located at about $\pm 1\, a_0$.

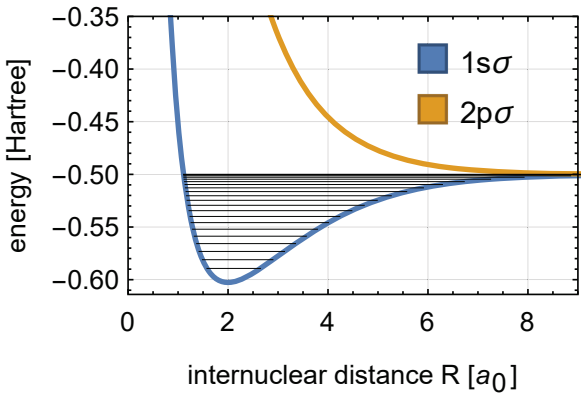

Figure 3.3.: Binding ($1s\sigma$) and anti-binding ($2p\sigma$) electronic curve. Additionally, the HD^+ vibrational energies for the rotational ground state $L = 0$ are shown [30].

(fine structure constant). The MHI's eigenenergies are written as

$$E(\alpha,\beta) = E_0 + \alpha^2 E_{\text{rel}} + \alpha^3 E^{(3)}_{\text{QED}} + \alpha^4 E^{(4)}_{\text{QED}} + \dots + \alpha^2 E^{(\text{fs})}_{\text{rel}} + \alpha^3 \beta E^{(3)}_{\text{QED, rec}} + \vdots$$

i.e. as functions of the electron-nuclear mass ratio $\beta = m_e/M \approx 10^{-3}$. The coefficient for the relativistic correction is E_{rel}, the leading order QED correction is $E^{(3)}_{\text{QED}}$ and higher-order corrections are required as well.

The resulting energies for different rovibrational states of H_2^+ and D_2^+ are shown in Figure 3.4 and for HD^+ in Figure 1.2.

The effective spin Hamiltonian for HD^+ consists of terms that are products of the spin operators and the rotational angular momentum [55],

$$\begin{aligned}\mathscr{H}^{\text{HD}^+}_{\text{eff}} =& E_1(\boldsymbol{L}\cdot\boldsymbol{s}_e) + E_2(\boldsymbol{L}\cdot\boldsymbol{I}_p) + E_3(\boldsymbol{L}\cdot\boldsymbol{I}_d) + \underbrace{E_4(\boldsymbol{I}_p\cdot\boldsymbol{s}_e) + E_5(\boldsymbol{I}_d\cdot\boldsymbol{s}_e)}_{\text{largest}} \\ &+ E_6\left\{2\boldsymbol{L}^2(\boldsymbol{I}_p\cdot\boldsymbol{s}_e) - 3\left[(\boldsymbol{L}\cdot\boldsymbol{I}_p)(\boldsymbol{L}\cdot\boldsymbol{s}_e) + (\boldsymbol{L}\cdot\boldsymbol{s}_e)(\boldsymbol{L}\cdot\boldsymbol{I}_p)\right]\right\} \\ &+ E_7\left\{2\boldsymbol{L}^2(\boldsymbol{I}_d\cdot\boldsymbol{s}_e) - 3\left[(\boldsymbol{L}\cdot\boldsymbol{I}_d)(\boldsymbol{L}\cdot\boldsymbol{s}_e) + (\boldsymbol{L}\cdot\boldsymbol{s}_e)(\boldsymbol{L}\cdot\boldsymbol{I}_d)\right]\right\} \\ &+ E_8\left\{2\boldsymbol{L}^2(\boldsymbol{I}_p\cdot\boldsymbol{I}_d) - 3\left[(\boldsymbol{L}\cdot\boldsymbol{I}_p)(\boldsymbol{L}\cdot\boldsymbol{I}_d) + (\boldsymbol{L}\cdot\boldsymbol{I}_d)(\boldsymbol{L}\cdot\boldsymbol{I}_p)\right]\right\} \\ &+ E_9\left[\boldsymbol{L}^2\boldsymbol{I}_d^2 - \frac{3}{2}(\boldsymbol{L}\cdot\boldsymbol{I}_d) - 3(\boldsymbol{L}\cdot\boldsymbol{I}_d)^2\right].\end{aligned} \tag{3.1}$$

The dominant contribution E_4 determines the hyperfine splitting, mainly by the proton spin $\boldsymbol{I}_p$ and electron spin $\boldsymbol{s}_e$ interaction. Approximately a factor 6 smaller is the

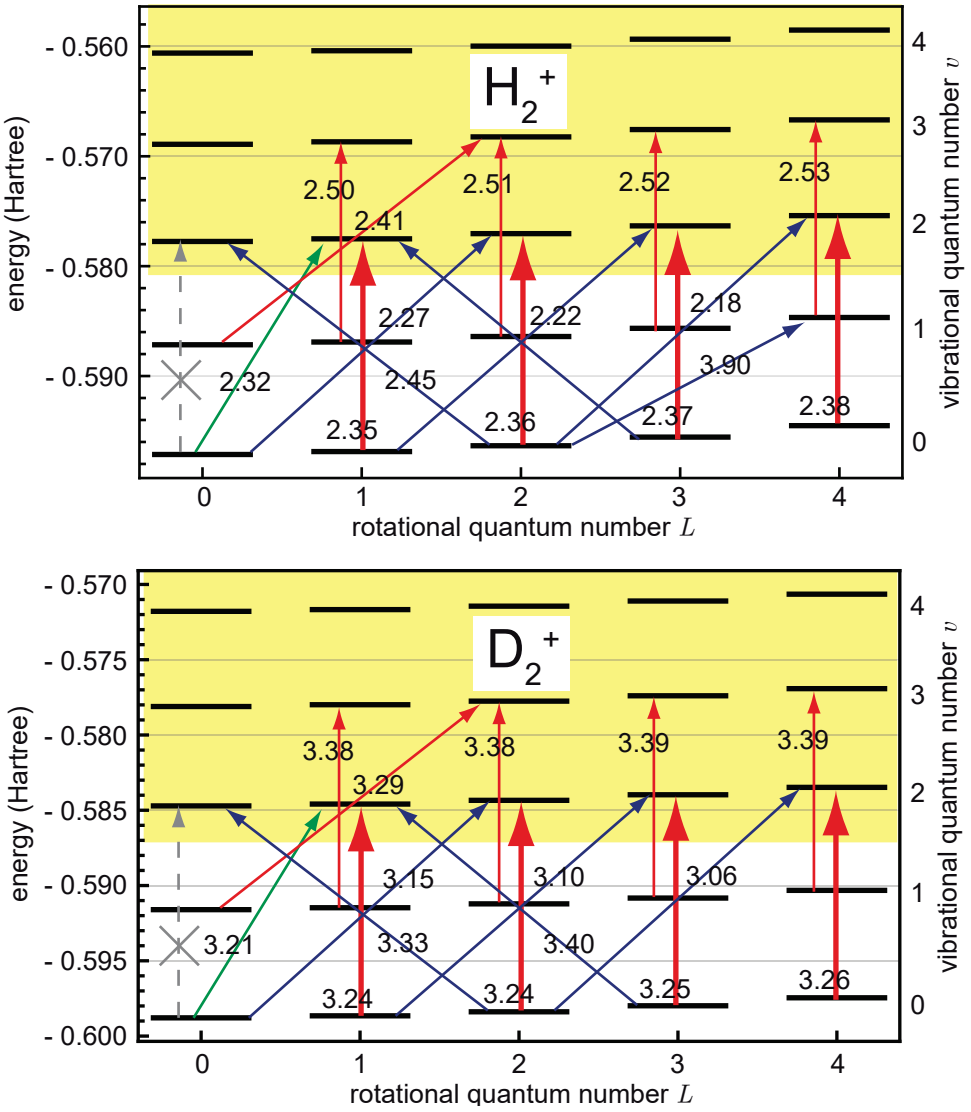

Figure 3.4.: Energies of the H_2^+ (upper Figure, by D. Bakalov, private communication) and D_2^+ (lower Figure, [54]) ion. Shown are transitions and the corresponding wavelength in µm that can be addressed with the Topo laser system (Section 5.6). The levels in the area highlighted in yellow are particularly suitable for photodissociation with 235 nm radiation from BePhI (see also Section 3.3 and Table 3.1).

coefficient E_5 for the interaction with the deuteron's spin $\boldsymbol{I}_d$. All other tensor spin-spin-orbit contributions (E_6, E_7 and E_8) are included as well as the contribution E_9 that is an interaction of the deuteron's quadrupole moment with the rotational angular momentum of the system $\boldsymbol{L}$.

In a similar way, the Hamiltonians can be constructed for the homonuclear molecules.

3.1. Angular Momentum Coupling Scheme for the HD^+ Molecule

Depending on the number of states, $\mathscr{H}_{\text{eff}}$ is a 4×4, 10×10 or 12×12 matrix, which acts on the wave function. The so called "pure" states $|vL;FSJ\rangle$ for a molecule are obtained by using a particular way of coupling the molecule's spins. The matrix can be computed in terms of the pure states as a basis. A diagonalisation results in a mixing of the pure states with corresponding coefficients. The eigenvalue states of $\mathscr{H}_{\text{eff}}$ are nevertheless still denoted by $|vL;FSJ\rangle$ where F and S are now approximate quantum numbers.

The interaction of the proton spin with the electron spin leads to the major energy contribution of the hyperfine splitting. Therefore, in the first instance, this major coupling is described by introducing the combined angular momentum $\boldsymbol{F} = \boldsymbol{I}_p + \boldsymbol{s}_e$. Next, the weaker coupling of the deuteron spin is added, resulting in the total spin $\boldsymbol{S} = \boldsymbol{F} + \boldsymbol{I}_d$. In the last step, the total spin $\boldsymbol{S}$ couples to the molecular rotation, with its rotational angular momentum $\boldsymbol{L}$. The total angular momentum of the system $\boldsymbol{J} = \boldsymbol{S} + \boldsymbol{L}$ is the sum of the total spin and the rotational angular momentum.

3.2. Interaction with a Magnetic Field

As a continuation of building up the hydrogen molecule's mathematical description, the effective spin Hamiltonian can be extended by the interaction of the molecule's magnetic moment $\boldsymbol{\mu}_A$ with a magnetic field $\boldsymbol{B}$ by $\mathscr{H}_{\text{mag}} = -\boldsymbol{\mu}_A \cdot \boldsymbol{B}$.

The interaction is simply added to the Hamiltonian $\mathscr{H}_{\text{eff}}^{\text{HD}^+}$ (equation 3.1). In case of the HD^+ ion, the effective total Hamiltonian for the electromagnetic field is [56]:

$$\mathscr{H}_{\text{eff}}^{\text{tot}} = \mathscr{H}_{\text{eff}}^{\text{HD}^+} + E_{10}\,(\boldsymbol{L}\cdot\boldsymbol{B}) + E_{11}\,(\boldsymbol{s}_e\cdot\boldsymbol{B}) + E_{12}\left(\boldsymbol{I}_p\cdot\boldsymbol{B}\right) + E_{13}\,(\boldsymbol{I}_d\cdot\boldsymbol{B})\,.$$

The coefficients E_{11}, E_{12} and E_{13} are trivial, since they follow from $\boldsymbol{\mu}_A$ and the magnetic moments of all particles. Here, the anomalous magnetic moment for a relativistic electron has to be used. The proton and deuteron magnetic moments are known from

level v	H_2^+	D_2^+
0	$5.199 \cdot 10^{-22}$	$4.660 \cdot 10^{-24}$
1	$7.399 \cdot 10^{-20}$	$1.251 \cdot 10^{-21}$
2	$1.904 \cdot 10^{-18}$	$7.685 \cdot 10^{-20}$
3	$9.309 \cdot 10^{-18}$	$1.498 \cdot 10^{-18}$

Table 3.1.: Dissociation cross section for H_2^+ and D_2^+ in cm^2 for 235 nm radiation [57]. The cross section for the vibrational level $v = 1$ is 25 times smaller than for $v = 2$ for H_2^+ and 60 times smaller for D_2^+.

experiments. The only term to be calculated numerically is $E_{10}(\boldsymbol{L} \cdot \boldsymbol{B})$ by averaging the wave function for the internal degrees of freedom of the system without spins.

Each of the $|vL;FSJ\rangle$ states contains $2J+1$ *Zeeman* states m_J. If the molecule is exposed to a magnetic field $\boldsymbol{B}$, the degeneracy is lifted and the *Zeeman* states split due to the *Zeeman* effect (Figure 9.3).

3.3. Transitions of the Homonuclear MHI

The homonuclear MHI offers interesting possibilities to study electric-dipole forbidden transitions. Here, a *Doppler* broadening of the transition line must be suppressed because of the necessary high radiation intensities. This can be achieved by cooling the ion into the *Lamb-Dicke* regime. Besides the electric quadrupole (E2) transitions, even electric dipole transitions $\Delta L = \pm 1$ should be possible for the homonuclear species, as V. Korobov and D. Bakalov have calculated (personal communication). This is possible because the real states of H_2^+ and D_2^+ no longer have a defined parity. The part of the relativistic Hamiltonian that describes the coupling between electron and nuclear spin as well as nuclear spin and the electron orbit also mixes odd nuclear spin states with even ones in first-order perturbation theory.

Figure 3.4 shows the relevant transition wavelengths of the H_2^+ molecular ion (left) and of the D_2^+ molecular ion (right). The thick red arrows indicate E2 transitions that are important for the "state distillation" (Section 8.4). For radiation of 235 nm, the cross section for an electronic excitation from the ground state $1s\sigma$ into the antibinding state $2p\sigma$ is much larger from the second excited vibrational level $v = 2$ than from its ground state $v = 0$ (Table 3.1). The values also indicate that an excitation from level $v = 1$ is possibly too slow. Therefore, the transitions $v = 1 \rightarrow v = 3$ must also be driven for the quantum state preparation (thin red arrows). Other E2 transitions that can be driven

with the Topo laser system (Section 5.6) are shown by blue arrows. The very weak E1 transition (0, 0) to (2, 1) is shown in green.

4. Laser Transitions, Line Shapes and Cooling of a Beryllium Ion

Laser cooling of a Beryllium ion and in particular the sub-*Doppler*-cooling in a harmonic potential of a miniaturised linear *Paul* trap is not a new technique, but still a challenging task [58]. A cold ion is essential for performing high-precision spectroscopy: The *Doppler* broadening of the line is suppressed, the expansion of the ion's wave function shrinks, while the oscillation energy in the harmonic potential decreases. At low temperatures, the *Lamb-Dicke* regime is reached, where the change in the motional state of the ion can be controlled with the spectroscopic laser.

The dynamics of the ions in the trap (Section 2.1) are treated in the interaction picture. The benefit of the interaction picture is that the three parts of the Hamiltonian (atom, field and interaction) can be treated separately simplifying the explicit calculation of the transition frequency that is important for the (motional) quantum state preparation, by the sophisticated sideband cooling technique. The latter requires a very good preceding *Doppler* cooling. The two processes are based on atom-photon interactions, in particular conservation of momentum, which is discussed in Section 4.2. A description of unresolved and resolved lines is presented afterwards.

4.1. Level Structure of the Beryllium Ion

The beryllium ion has a $1s^2 2s^1$ electronic configuration. In the following, the focus is on the two states of interest ^2S and ^2P. The transition frequency is about 1000 THz (Figure 4.1). The P levels show a fine structure because the orbital momenta and the spin couple, in contrast to the S level (electronic ground state), which has no angular momentum. Since the spin is $S = 1/2$, there are only two possibilities $L \pm \frac{1}{2}$ for the fine structure $^2P_{3/2}$ and $^2P_{1/2}$. Due to the electromagnetic multipole interaction, the levels split. The frequency splitting is roughly 197 GHz, while the linewidth of each line is γ =19.6 MHz [59]. They are well resolved (Section 4.3.1) and act as independent lines. The nuclear spin $I = 3/2$ of beryllium additionally causes a hyperfine splitting. All angular momenta add up to the total angular momentum $F = L + S + I$. The ground

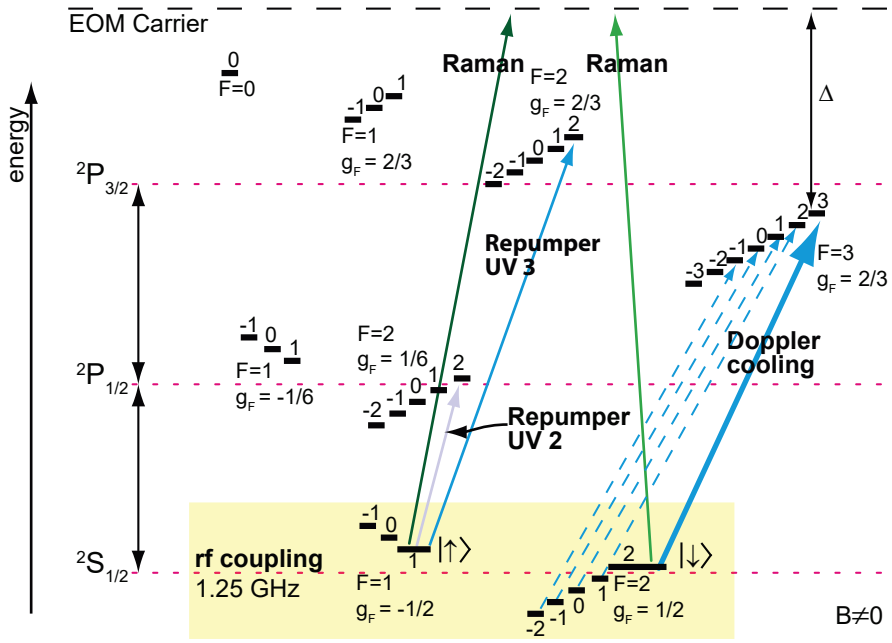

Figure 4.1.: Selected *Zeeman* sub levels of beryllium in a magnetic field (not to scale). Shown are the relevant laser transitions. The M1 transitions are discussed in detail in Chapter 7. The dashed lines indicate the optical pumping into the state with maximum m_F by driving the almost closed cycling transition. The EOM integrated in the UV 3 laser system generates a sideband with the frequency Δ.

state splits into two levels $F = 1,2$ with a 1.25 GHz spacing. The hyperfine splitting of the upper states, $F = 0,1,2,3$, is on the order of 10 times of the natural linewidth γ.

The degenerate *Zeeman* sub-states with projection quantum number m_F for each F-state split in a external magnetic field, and the splitting depends on the magnetic field strength B. The ground state splitting is computed with help of the *Breit-Rabi* formula

$$E(F,m_F;B) = hA\left(-\frac{1}{4} + \frac{g_I m_F \mu_B B}{hA} \pm \frac{2I+1}{4}\sqrt{1+\frac{4m_F}{2I+1}x(B)+x(B)^2}\right) \tag{4.1}$$

$$x(B) = \frac{(g_J - g_I)\mu_B}{\left(I+\frac{1}{2}\right)hA}B$$

with the hyperfine constant $A = -625008837.044(12)$ Hz, the g-factors $g_J = 2.002262$ and $g_I = 2.134779853 \cdot 10^{-4} g_J$ [60, 61] (Figure 4.2).

In addition to the internal energy states of the ion, the states of motion within the harmonic trap potential must be considered. As a consequence, each atomic state splits into many motional states equally spaced above the considered motion-free state (Figure 4.3). In the following, the two-level single ion interaction with a photon is discussed.

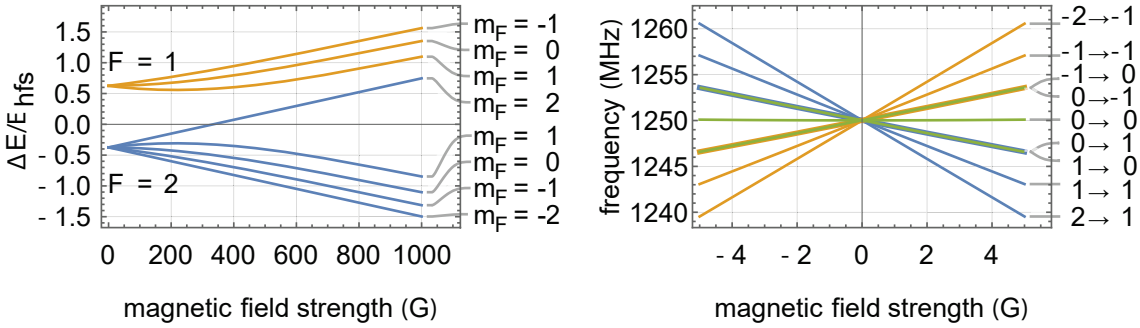

Figure 4.2.: Magnetic field dependent energy shift of the hyperfine levels of the beryllium ground state with respect to the $m_F = 0 \rightarrow 0$ transition at zero magnetic field, E_{hfs} (left). The resulting transition frequencies between these are shown on the right.

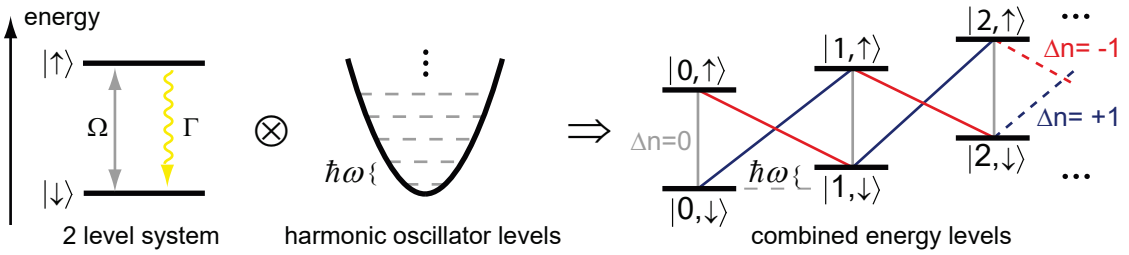

Figure 4.3.: A two-level system that oscillates in the trap potential: The internal ion state is superimposed on the quantum harmonic oscillator state in the trap potential ($\Delta E = \hbar\omega_{\mathrm{trap}}$). Thus, excitation possibilities arise in which the state of motion changes. Shown are two (electronic) states $|n, \uparrow \text{ or } \downarrow\rangle$ in the motional state with quantum number n.

4.2. Ion-Photon Interaction and Conservation of Momentum

Electrical dipole-allowed transitions E1 are required for the *Doppler* cooling transitions. The lithium-like beryllium ion is in the initial state $\left|g\right\rangle \equiv |\downarrow\rangle$ and interacts with a radiation field of energy $E_L = \hbar\omega_L$ (subscript L for laser). If the ion's resonance frequency ω_0 is approximately equal to the laser frequency ω_L, the ion can be excited to the final state $|e\rangle \equiv |\uparrow\rangle$. Discussing quantum states and electrical fields simultaneously corresponds to a semi-classical approach.

While absorbing a photon, the ion is accelerated because of the transferred photon momentum $\boldsymbol{P}_\nu = \hbar\boldsymbol{k}$ (wave vector $\boldsymbol{k}$). Due to spontaneous emission, a photon is emitted in a random direction. The rate is proportional to the resonance frequency ω_0 cubed of the considered transition and to the squared of the dipole transition matrix element with its dipole-operator $\boldsymbol{d} = -e\sum_{j=1}^{N}\boldsymbol{r}_j = -e\boldsymbol{r}$ (here, $N = 1$ electron in a non-closed shell), $\gamma \sim \omega_0^3 \langle e|\boldsymbol{d}\left|g\right\rangle^2$.

Averaging over many absorption/emission cycles, the total absorbed momenta are always parallel to the laser beam direction $\boldsymbol{k}$ and add up, while the momentum transfer during emission processes almost vanishes. Therefore, these cycles can be used for laser cooling, i.e. to reduce the momentum of the ion when the laser radiation is red detuned.

In the electric dipole approximation, the interaction of the ion with the field is described by an interaction Hamiltonian

$$\begin{aligned}\mathscr{H}_{\text{int}} &\approx -\boldsymbol{d}(\boldsymbol{r})\cdot\boldsymbol{E}(\boldsymbol{r},\boldsymbol{R},t)\\ &= \boldsymbol{d}\cdot\boldsymbol{E}_0\cos\left[\omega_L t + \boldsymbol{k}\cdot\boldsymbol{R} - \varphi(t)\right]\end{aligned} \tag{4.2}$$

that connects the internal degrees of freedom (electron's position vector $\boldsymbol{r}$ with respect to the nucleus) and the external degrees like the nucleus' position vector $\boldsymbol{R}$ in coordinate space. Here, E_0 is the (real) amplitude of the electric laser field. If there is a temporal variation of the phase $\varphi(t)$, the ground state preparation process will be disturbed. On a time scale of a few tens of milliseconds, a phase stabilisation should be implemented in this case.

The interaction Hamiltonian can be expressed in terms of the *Rabi* frequency $\Omega_{eg} = -\boldsymbol{d}\cdot\boldsymbol{E}_0 e^{i\varphi(t)}/\hbar \equiv \left|\Omega_{eg}\right| e^{-i\varphi(t)}$ [62] :

$$H_{\text{int}} = \hbar\left[\left|\Omega_{eg}\right||e\rangle\langle g| + \left|\Omega_{ge}\right|\left|g\right\rangle\langle e|\right]\cos\left[\omega_L t + \boldsymbol{k}\cdot\boldsymbol{R} - \varphi(t)\right] \tag{4.3}$$

The total Hamiltonian of this effective two-level system in the interaction picture is given by

$$\mathscr{H}_{\text{tot}} = \mathscr{H}_{\text{atom}} + \mathscr{H}_{\text{int}}, \tag{4.4}$$

with the Hamiltonian $\mathscr{H}_{\text{atom}} = \frac{\hbar\omega_0}{2}\left(|e\rangle\langle e| + |g\rangle\langle g|\right)$ of the undisturbed atom. Formally, the total Hamiltonian $\mathscr{H}_{\text{tot}} = \mathscr{H}_0 + V$ splits in the interaction picture into a part with known solution (for example that of the free ion $\mathscr{H}_0 = \mathscr{H}_{\text{atom}}$) and the interaction part $V = \mathscr{H}_{\text{int}}$. The latter is a time dependent operator. In an eigenstate representation, the matrix of $\mathscr{H}_0$ is diagonal, while $V_{ij}(t) = \langle i|V(t)|j\rangle$ in general is not and so transitions between the eigenstates are possible. However, it is not always meaningful to describe transitions in this intuitive way (details in [62]). To drive a transition between the states $|i\rangle$ and $|j\rangle$, the interaction $V(t)_{ij}$ has to be non-zero and therefore it has to have some *Fourier* components at the resonance frequency $\omega_{ij} = \left(E_i - E_j\right)/\hbar$.

To solve the *Schrödinger* equation $\mathscr{H}_{\text{tot}}\psi_e = E\psi_e$, first it is assumed that the transition rate from state $|g\rangle$ to $|e\rangle$ is equal to that from state $|e\rangle$ to state $|g\rangle$, $|\Omega_{eg}| = |\Omega_{ge}| \equiv \Omega_0$ and also the rotating wave approximation (RWA) is used. In this case two frequencies are important, the detuning of the wave frequency from the transition frequency $\delta = \omega_0 - \omega_L$ and the fast oscillation $\omega_0 + \omega_L$. Taking only slow processes into account, where in this context 'slow' are time periods larger than $1/(\omega_0 + \omega_L)$, only the contribution of the slowly varying terms δ are non-negligible in the so-called secular approximation. For a further simplification, a laser beam that is parallel to the z-axis is assumed, $\boldsymbol{k}\|\boldsymbol{z}$. Using $V'_{ij}(t) = e^{i\omega_{ij}t}V_{ij}(t)$ in the interaction picture (indicated by an inverted comma $'$) the Hamiltonian becomes with ($\omega_{eg} = \omega_{ge} \equiv \omega_0$) and $\varphi(t) = 0$:

$$\begin{aligned}\mathscr{H}' &= \frac{\hbar\Omega_0}{2}\left(e^{i\omega t}|e\rangle\langle g| + e^{-i\omega t}|g\rangle\langle e|\right)\left(e^{-i\omega_L t - ikz} + e^{i\omega_L t + ikz}\right)\\ &= \frac{\hbar\Omega_0}{2}\left(e^{i\delta t}e^{-ikz}\underbrace{|e\rangle\langle g|}_{\text{absorption}} + e^{-i\delta t}\underbrace{e^{ikz}}_{\text{momentum kick}}\underbrace{|g\rangle\langle e|}_{\text{emission}}\right)\end{aligned}$$

The (internal) electronic transition from one state to another by absorbing or emitting a photon changes also the (external) momentum of the ion ("it is kicked by the photon").

4.3. Laser Cooling of Trapped Ions

The aim of laser cooling is to reduce the population number n of the motional modes in the trap potential. This corresponds to a slowing down of the particle movement,

i.e. a reduction of its kinetic energy. An energy, in turn, can be related to a temperature with the *Boltzmann* constant k_B. To "cool" an ion, motional energy has to be dissipated from the system using the concept of section 4.2.

In the following laser cooling with resolved and unresolved spectral lines of beryllium are distinguished. An interaction of the ion with a photon implies a transition between two or more states. The rate of such a transition depends on the detuning δ of a laser with a certain linewidth, but also on the linewidth of the involved initial and final states and their energy difference to surrounding states. The state's minimal linewidth is called the natural linewidth and is related to the ability of the state to interact with the vacuum modes. In the case of beryllium, the P-state can decay quickly (dipole-allowed) to the S-state. Hence, its linewidth $\gamma \approx 2\pi \cdot 20\,\mathrm{MHz}$ is relatively broad.

4.3.1. *Doppler* Cooling and Line Spectrum

In order to cool the ion efficiently by photon recoil, many photons must be scattered in a short time interval. A suitable candidate for *Doppler* cooling is therefore the short-lived P-state. The $S_{1/2} \leftrightarrow P_{3/2}$ transition is an (almost) closed cycling transition.

In case of beryllium with its nuclear spin $I = 3/2$ there are are two possibilities for a *Doppler* cooling transition: Making use of the ion's hyperfine structure, the state $S_{1/2}\,(F = 2, m_F = \pm 2)$ is an ideal candidate for the initial state and $P_{3/2}\,(3, \pm 3)$ for the final state.

There is (almost) no chance for the electron to escape this transition - this is where the name cycling transition comes from. With the (almost) closed $\sigma^{\pm}$-cycling transition, the angular momentum is pushed to its extremum. If the laser's polarisation was wrong, excitation to unwanted states would be driven. However, the remaining $\sigma^{\pm}$-light leads to an overall pumping until maximum population is reached in state $m_F = \pm 2$ (Figure 4.1 and also Section 7).

In principle, there can still be a transition $S_{1/2}\,(F = 2) \rightarrow P_{3/2}\,(F = 2) \rightarrow S_{1/2}\,(F = 1)$, because the separation of the F-states in the $P_{3/2}$-level is relatively small. This will lead to a pumping into the meta-stable dark state $S_{1/2}\,(F = 1)$ (roughly every 10^{-4} cooling transitions will end in the dark state, even for optimal conditions [58]). Hence, *Doppler* cooling of beryllium requires a "repumper" or "recooling" laser, depleting that dark state and transferring population back to the initial state.

The state $|F = 1, m_F = 1\rangle$ will not decay by itself into the initial state. There are three possibilities to restore the initial sate and therefore perform the dissipation process:

1. Via a pump process to the $P_{1/2}$ state with its comparable large linewidth γ. Basically, one photon is scattered and the ion can be transferred to the possible states

$|2,2\rangle$ and $|2,1\rangle$. A second laser (e.g. UV 2) detuned by approx. 197 GHz (fine structure splitting) from the *Doppler*-cooling transition can be used to close the cycle. Hence, the transition $^2S_{1/2}\,(1,1)$ to $^2P_{1/2}\,(2,2)$ has to be driven resonantly with σ^+ polarised light. From that state it can either decay back to the state $^2S_{1/2}\,(1,1)$ and it has to be excited again or it decays to the initial state $^2S_{1/2}\,(F=2)$, which is a dark state in terms of the repumping process.

2. If sidebands of 1.25 GHz are modulated with an EOM onto the cooling laser, the metastable state is emptied via $P_{3/2}$.

3. The population can be transferred to $F = 2$ without any usage of a laser. An rf-antenna can drive this M1-transition (Figure 7.1 and 7.3), while the motional state is preserved. This property is particularly important for ground state cooling.

To pump the ion into the initial state $^2S_{1/2}\,(2,2)$ with the maximal angular momentum $m_F = 2$, the *Doppler* cooling laser is necessary.

To cool down the ion moving counter propagating in respect to the cooling laser's wave vector, a red-detuned "catching" beam (detuning δ) is used. It efficiently cools the initially on average hot and thus energetic ions. For this ion catching stage, a pre-cooling is needed that is more red-detuned than the ideal shifted beam for *Doppler* cooling. The optimal detuning is defined in respect to the point of maximal scattering and corresponds to half of the transition linewidth $\delta_{\text{ideal}} = \gamma/2 \approx 2\pi \cdot 10\,\text{MHz}$. This is basically true for a free ion and a low laser intensity ($I < I_{\text{sat}}$). The former is an approximation for a single ion at the trap's center. If the ion is perfectly cold, the effect of the cooling beam will be very small. Ideally, the Doppler temperature $T_D = \frac{\hbar\gamma}{2k_B}$ can be reached in this manner.

In the general case (uncompensated trap), the trap frequency $\widetilde{\Omega}$ leads to sidebands that are resolved in the fluorescence spectrum, (Figure 6.6), but this does not hold for the secular frequencies $\omega_{\text{sec}} \ll \gamma$ for the considered *Doppler* cooling transition. The micromotion peaks at $\pm\widetilde{\Omega} = 2\pi \cdot 35.8585\,\text{MHz}$ are less intense than the carrier and the total fluorescence signal is the sum of this three peaks. Since the FWHM is $\gamma = 2\pi \cdot 19.6\,\text{MHz}$ in each case, this leads to a broadened overall line shape. In contrast, ions on the trap axis do not experience micromotion modulation (perfectly compensated trap) and so the point of maximum scattering corresponds to the frequency of the atomic transition.

5. System Overview

The new experimental setup was designed to be modular from the very beginning, which means that individual elements can be added or used differently as desired without requiring much effort. The modules are optical setups or laser systems that are installed on their individual breadboard which are located on an U-shaped floating table. This has the advantage that they are easily accessible from all sides for maintenance work and beam distribution. A schematic overview of all modules involved in the project and their allocated space is shown in Figure 5.1, while a photographic impression of the laboratory is shown in Figure 5.2 and 5.3. The advantages of the modular concept can be seen when comparing the two photos, which were taken over a time span of two years: The UV 2 laser source was easily moved in favour of the QCL.

These systems are partly linked with optical fibres or alternatively via free-space beam propagation.

A more detailed close-up of the beam path near the vacuum chamber is shown in Figure 5.4. Due to the large number of laser beams used so far (more will be needed in the future to implement all applications), it is obvious that the vacuum chamber needs plenty of viewports. However, the generation of the vacuum should be made efficient by keeping the chamber volume as small as possible. The challenge is to arrange the complex assemblies in the vacuum chamber so that no viewport is blocked (Figure 5.7).

The chamber was therefore designed as follows: It can be divided into 3 levels (Figure 5.5). The topmost one is mainly for the electrical supply. The hydrogen gas inlet is also located here. The middle level is dedicated to the optical access, while everything else has to be placed in the lowest level: in particular, the 100 mm diameter turbo-molecular pump connector must be mentioned, as well as a large access through which the beryllium ovens can be easily removed. A residual gas analyser is also installed here. To achieve a vacuum less than 10^{-10} mbar, an ion pump with non-evaporable getter material is used.

Except for the ovens, the remaining contents are mounted on a grid-like structure. This structure holds the particle trap, the electron gun, the particle detector and the

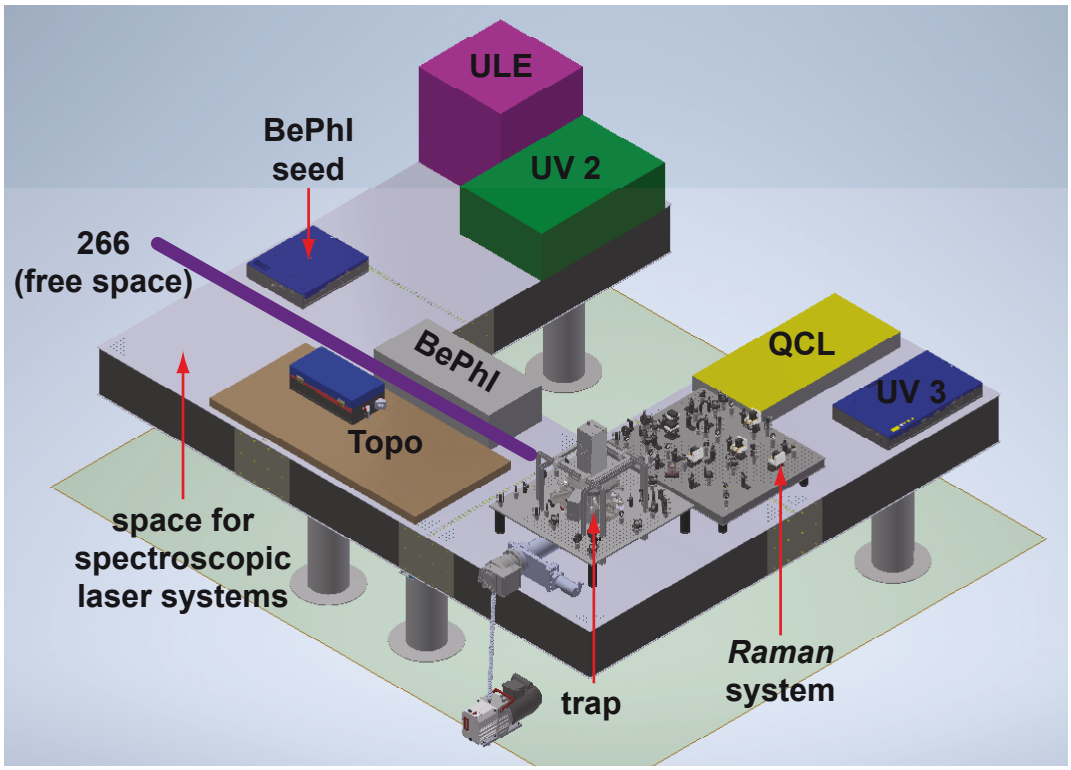

Figure 5.1.: Schematic overview of all modules: For beryllium manipulation, UV 3, ULE, *Raman* system, UV 2 and BePhI are used, while for the MHI manipulation QCL, 266 and Topo are taken. The abbreviations are explained in section 5.6.

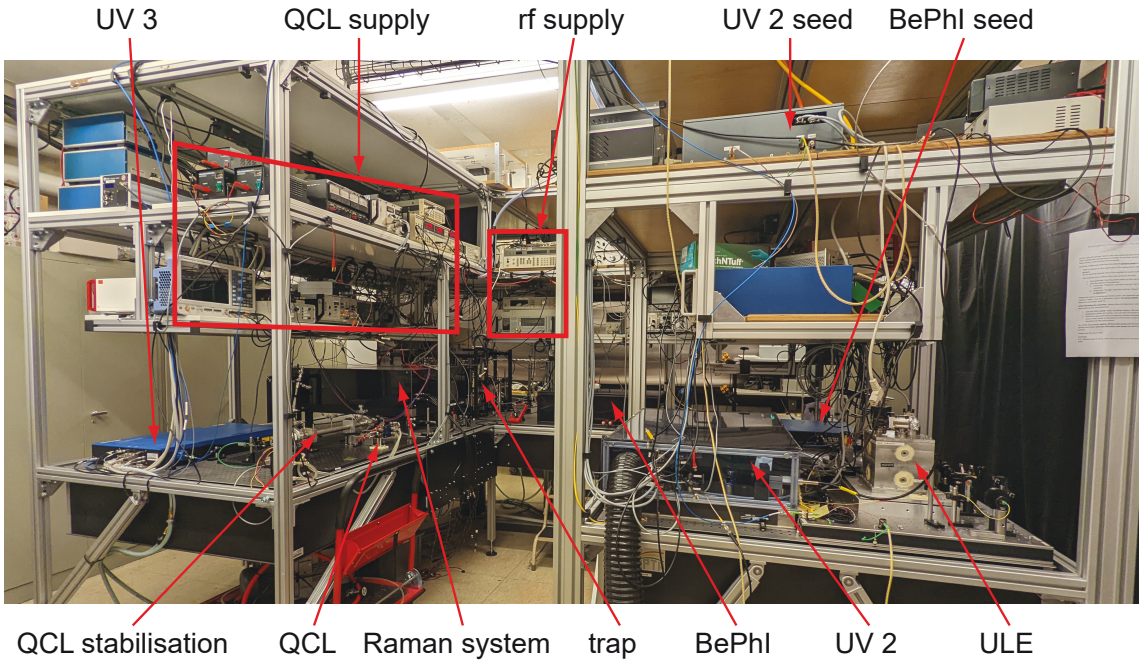

Figure 5.2.: Complete overview of the setup in the laboratory from May 2022: The abbreviations of the components are explained in the text.

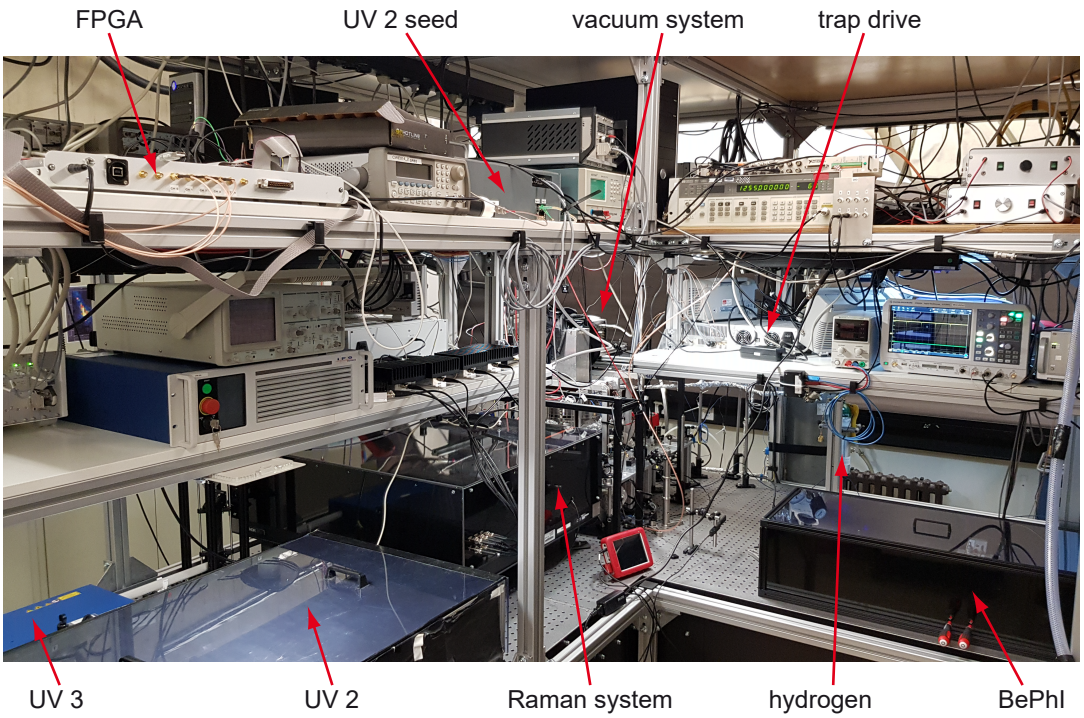

Figure 5.3.: Photograph of a segment of this experiment from April 2020: At that time, UV 2 was located at the location of the QCL from Figure 5.1.

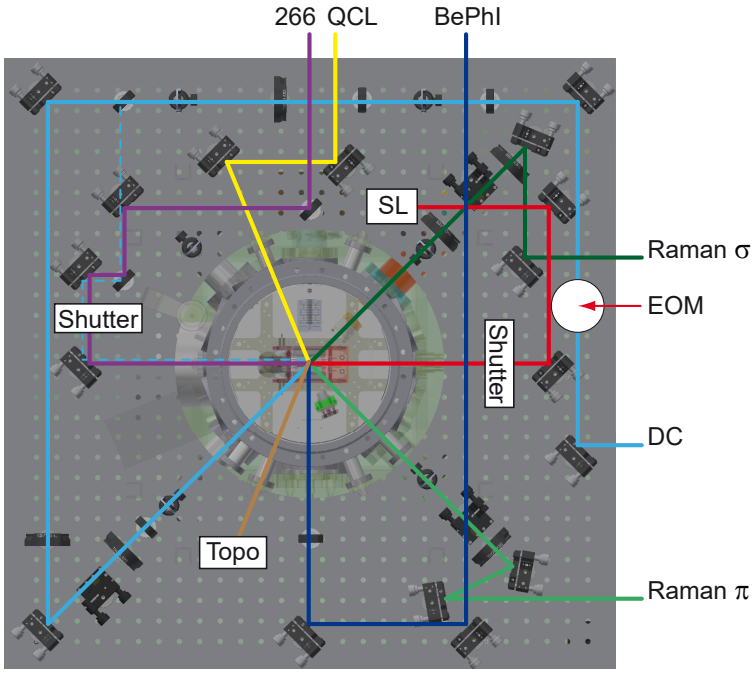

Figure 5.4.: Various laser beam paths around the chamber (not in the smallest detail): *Doppler* cooling beam (DC) in light blue (with split-off beam for axial cooling, dashed), two perpendicular *Raman* beams (light and dark green), BePhI (dark blue), QCL (yellow), 266 (violet) and the fiber coupled spectroscopy laser (SL, red) and Topo (light brown). An electro-optical modulator (EOM) generates sidebands on the DC at 1.25 GHz.

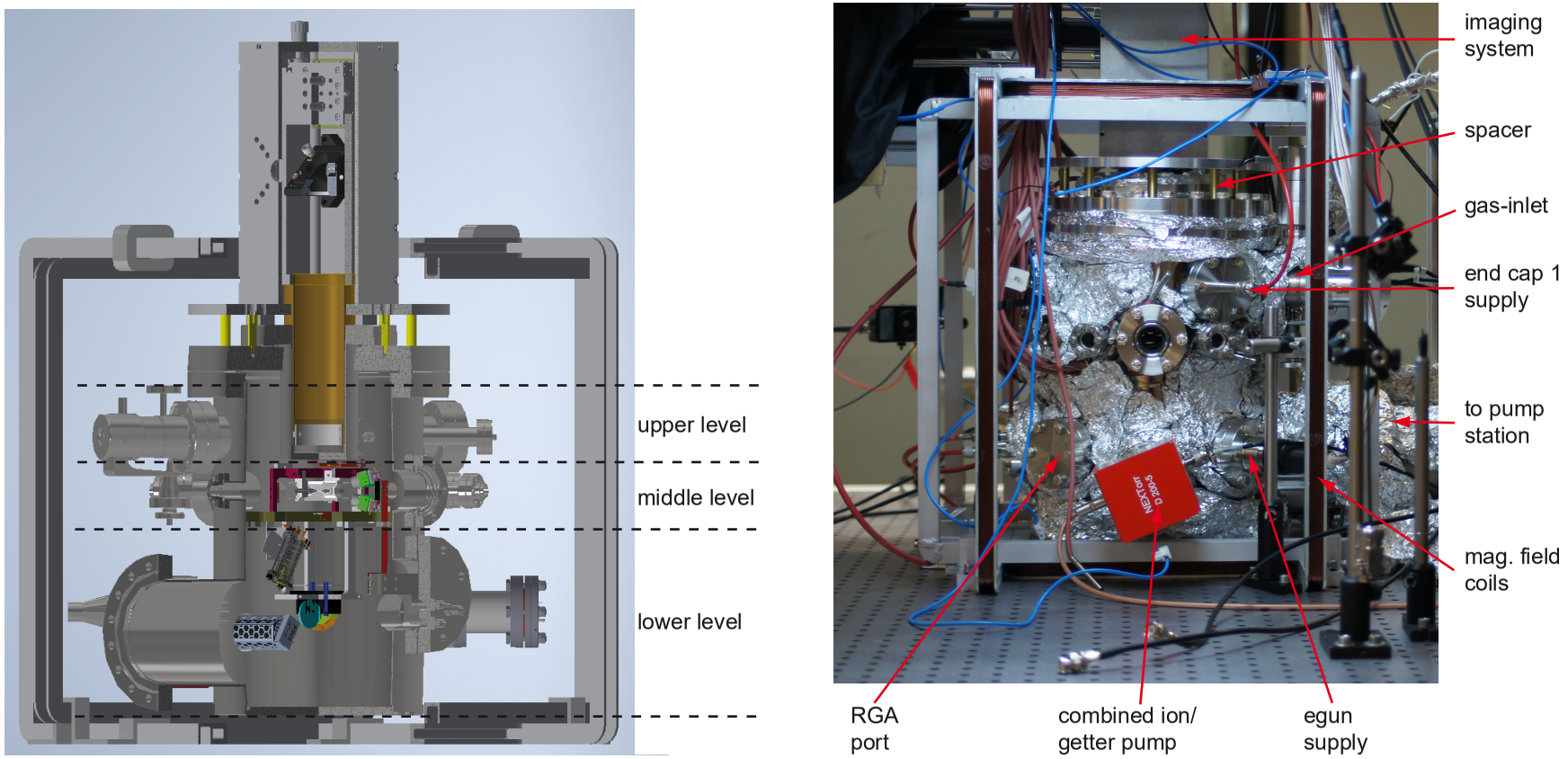

Figure 5.5.: Design of the vacuum chamber: Shown are the three levels of the chamber (left, see also Figure 1, Appendix A). The imaging unit for the ions is placed on the lid. A reentrant window in which the lens system is located reaches into the chamber to a position shortly above the trap (brown). On the right is a photo of the partially equipped chamber from June 2016, so that details can be seen.

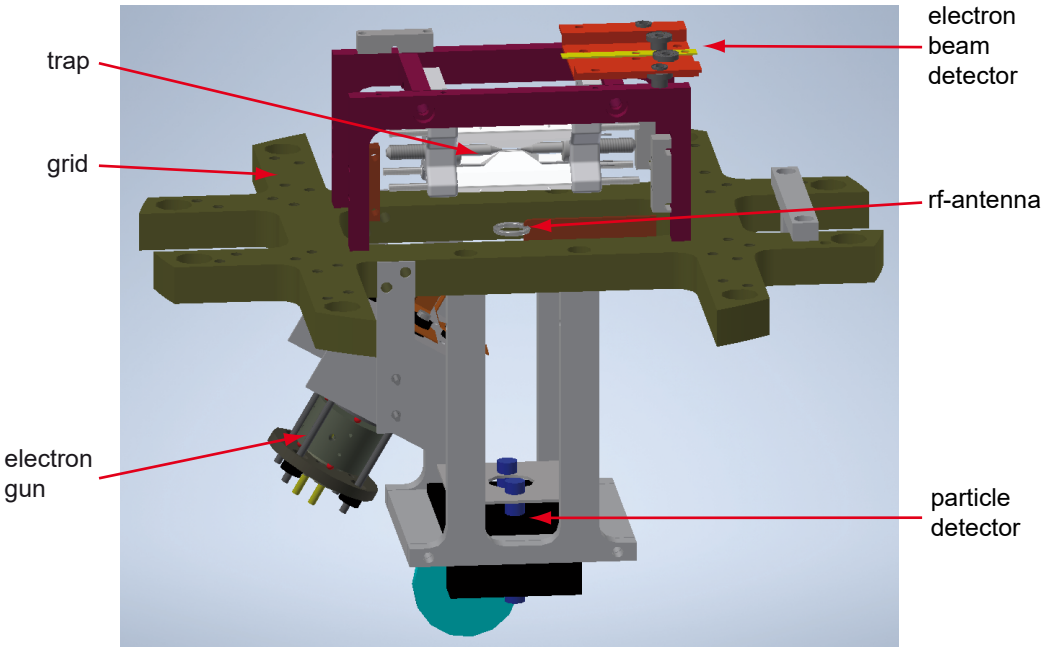

Figure 5.6.: Schematic overview of the experimental unit (side view).

electron beam detector. Thus, the entire unit can be removed from the chamber in one piece. A schematic drawing and a photo are shown in Figure 5.6 and 5.7.

5.1. Design of the Trap

The *Paul* trap is part of the experimentation unit (Figure 5.6 and 5.7). The design is adapted from one used in the Blatt group at the University of Innsbruck [63]. A detailed theoretical treatment of the *Paul* trap is given in Chapter 2.

The miniaturised linear *Paul* trap used (Figure 5.8) has the advantage of allowing high radial and axial confinement, while at the same time the distance $r_0 = 0.8\,\text{mm}$ between the electrodes and the centre of the trap is large enough for a good optical access.

This design requires quadrupole electrodes with a diameter of 0.4 mm. For stability reasons, only the side facing the ion is half-circular, while the rear part consists of a blade-shaped support structure (A in Figure 5.8). Finite element simulations show that this support structure has no negative influence on the potential at the ion's position (Figure 5.9).

The distance between the two end cap electrodes (B) is 5 mm. In the trap centre, at the storage location of the ion, an axial harmonic potential is needed (Section 2.1). This can be generated by two point charges, which are approximately implemented here by the tips of the end cap electrodes. For axial laser access to the centre of the trap, these

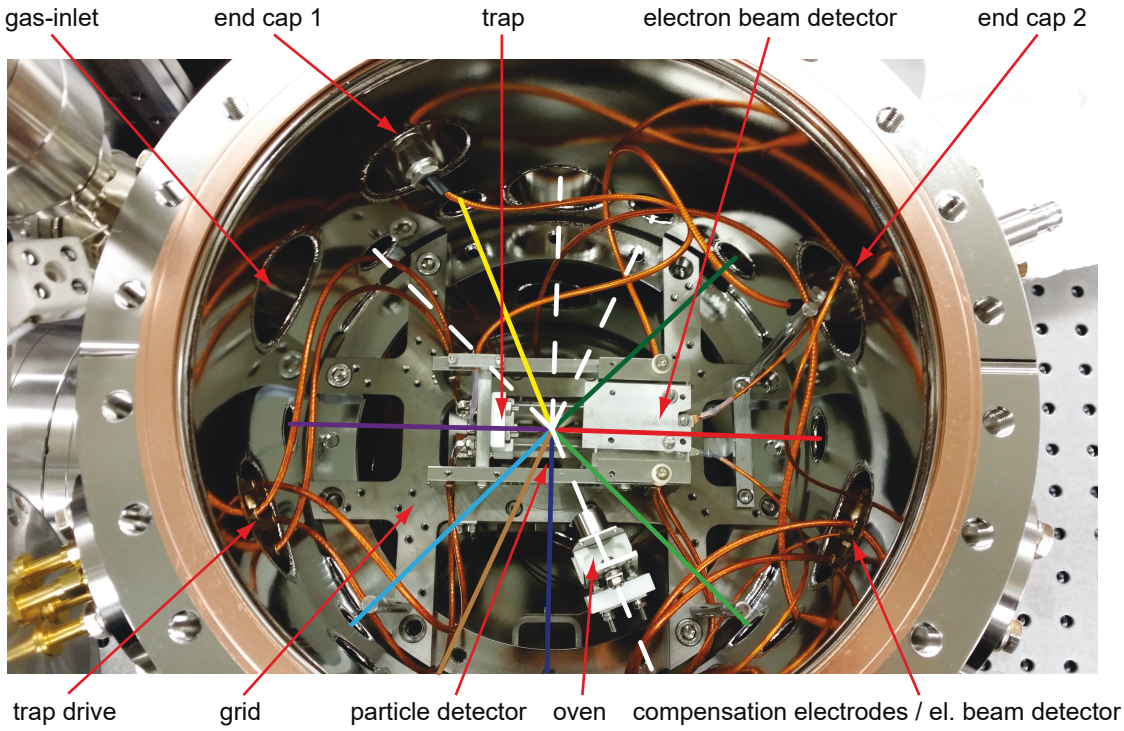

Figure 5.7.: Experimental unit in the chamber (top view): Next to the electrical connections, an open beryllium oven without a filament can be seen. The beam paths are indicated with the same color coding as in Figure 5.4. Unused pathways are shown with white dashed lines.

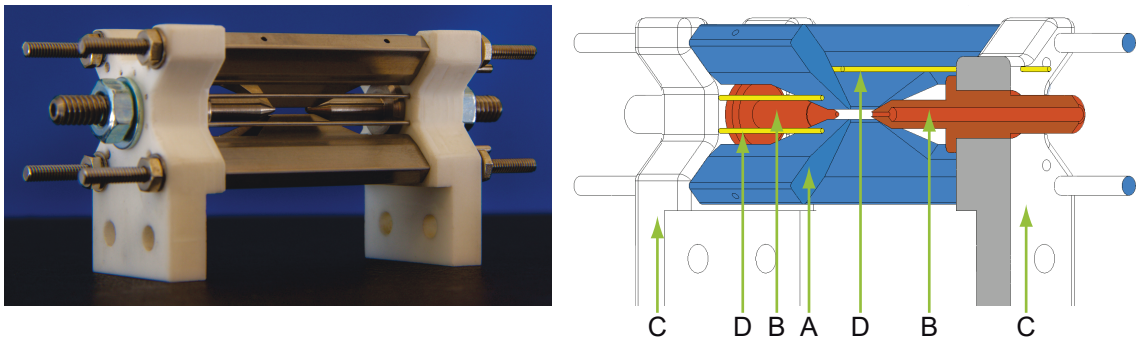

Figure 5.8.: Linear *Paul* trap: Photography of the *Paul* trap developed for this thesis (left) and a schematic drawing (right). The description of the individual components (A to D) is given in the main text. See also Figure 3, Appendix A.

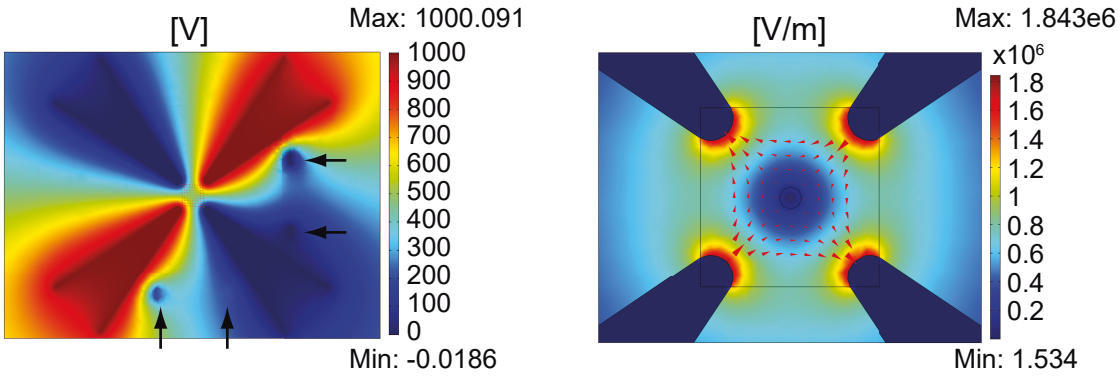

Figure 5.9.: Simulation of the radial potential (left) and the field direction (right, red arrows) due to the non-hyperbolically shaped blade electrodes. It can be seen that the support structure has no negative effect on the trap potential. It remains radially symmetrical. For the simulation, 20 % of the maximum voltage is applied to the compensation electrodes (black arrows).

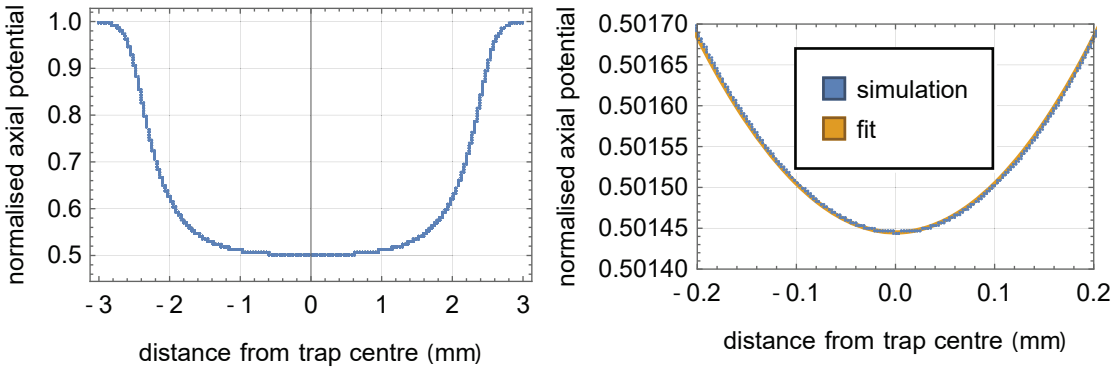

Figure 5.10.: Normalised axial potential of the end cap electrode simulated by Comsol: The full range is shown left, while the part relevant to a few ions (right) shows a good overlap with a square fit in a range of a few tens of micrometres.

electrodes have a central hole. Despite the clear deviation of the electrodes from point charges, the simulation of the axial potential (Figure 5.10) gives the desired shape.

The electrodes are mounted by the MACOR holder (C) shown in Figure 5.8, electrically insulated from each other and aligned with each other. However, the insulating property of the MACOR has the major disadvantage that charges can stick to it. These can be caused, for example, by the UV lasers interacting with residual gas particles present in the vacuum chamber, or by the use of the electron gun. Space charges present a problem because they change the shape of the trap potential, causing it to deviate from the ideal. To minimise the non-conductive MACOR surface facing the centre of the trap, the end caps are provided with a (shielding) plate. Charges that settle here are compensated by the voltage supply of the end cap electrode.

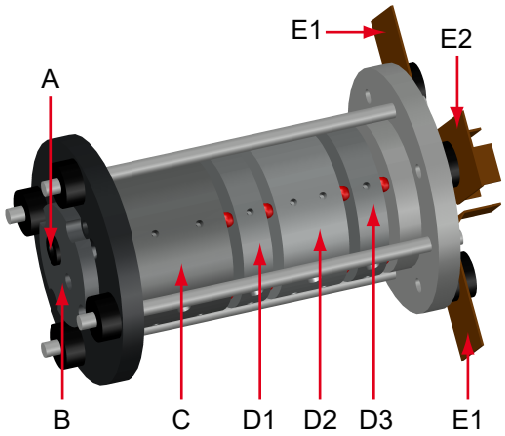

Figure 5.11.: Schematic illustration of the electron gun. For explanations, see main text.

Any asymmetries in the potential must be counterbalanced with the two compensation electrodes (D) available. For this purpose, one pair of cylindrical electrodes is mounted for horizontal deflection of the ion (parallel to the optical table) and one under the trap for vertical deflection. Each pair is at the same potential and generates a potential at the centre of the trap similar to that of a single electrode positioned centrally between the blade electrodes. The latter, however, would have the crucial disadvantage that the optical access to the ion is blocked by the electrode.

5.2. Electron Gun

The electron gun is part of the experimentation unit (Figure 5.11 and 5.7). This very compact version of an electron gun is described in [64]. With its 5 cm length, it fits well into the vacuum system. It hangs under the base plate and is axially aligned with the centre of the trap. The electron gun consists of three parts: A combination of an electrode, filament and *Wehnelt* cylinder as a directed ion source, imaging optics and deflection electrodes for directing the ion beam. A tungsten filament is heated with the cathode (B) current I_{cat} (the anode is labeled A), causing low-energy electrons to be emitted by incandescent emission. These are focused through a small aperture by a voltage U_{Weh} applied to the *Wehnelt* cylinder (C). Cathode and *Wehnelt* cylinder are at an adjustable negative potential with respect to ground. Before the electrons leave the electron gun with the well-defined acceleration energy they pass through an einzel lens (D1 to D3, voltages $U_{1,\mathrm{egun}} = U_{3,\mathrm{egun}}$ and $U_{2,\mathrm{egun}}$) and can thus be focused through the trap structure. An electron beam detector above the trap is used for alignment and functionality tests, and prevents the electrons from striking the reentrant window. A misalignment of the gun can be compensated by vertical (along the trap axis) and

U_{Weh}	cathode	U_{H}	U_{V}	$U_{1,\text{egun}}$	$U_{2,\text{egun}}$	I_{cat}
-214 V	-210 V	13.4 V	15.9 V	0.82 kV	2.00 kV	2.75 A

Table 5.1.: Electron gun setting: The values given refer to a trap voltage $U_{\text{rf}} = 60$ V with the magnetic field switched off.

horizontal deflection electrodes (E1, E2). Due to the small trap volume with the close spacing of the blade electrodes, focusing the electron beam using the einzel lens has proven to be particularly crucial, as also has the horizontal and vertical deflection of the beam.

In contrast to the values proposed in [64] for the electron impact ionisation of beryllium (750 eV), significantly lower energies can also be used. Thus, the voltage source does not need to be switched manually when changing from beryllium to HD trapping. Typical parameters for ionising beryllium, molecular hydrogen or other species are listed in Table 5.1. These parameters depend strongly on the selected trap voltage and applied magnetic field.

5.3. Electron Beam Detector

The electron beam detector is part of the experimentation unit (Figure 5.6 and 5.7). The alignment of the electron beam emitted by the electron gun is crucial, since it has to pass the small gap between the trap's quadrupole electrodes. It depends on many parameters, as discussed in Section 5.2. With the help of the detector, the beam can be directed in such a way that the generation of stray charge in the vicinity of the trap is reduced to a minimum.

The detector essentially consists of two metal plates of different sizes that are arranged one above the other. Its potential with respect to ground can be measured. The decisive aspect is that one plate is much smaller than the other. The alignment of the electron gun in respect to the trap and detector is mechanically chosen so that a straight beam passes the trap centre and hits the smaller plate, charging it. If the beam is broadened due to wrong focusing parameters $U_{1,\text{egun}}$,$U_{2,\text{egun}}$, U_V and U_H, it also hits the second one. It always intercepts the beam and prevents charging of the reentrant window above.

The beam is optimally aligned and focused if the signal from the smaller plate is maximised and that from the larger plate is minimised at the same time (Figure 5.12). The figure shows that the electron gun requires a relatively long heat-up time of 7 seconds.

For the ionisation of beryllium or other species, a signal of + 6 mV, measured with a 1 MΩ oscilloscope input, has been shown to be sufficient.

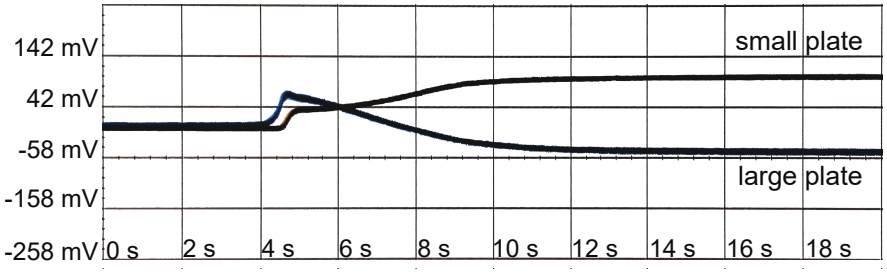

Figure 5.12.: Detected voltages at the two plates (large and small) of the electron beam detector as a function of time. At time index 4 s the electron gun is switched on and heats up. After another 7 seconds, a steady emission state is reached.

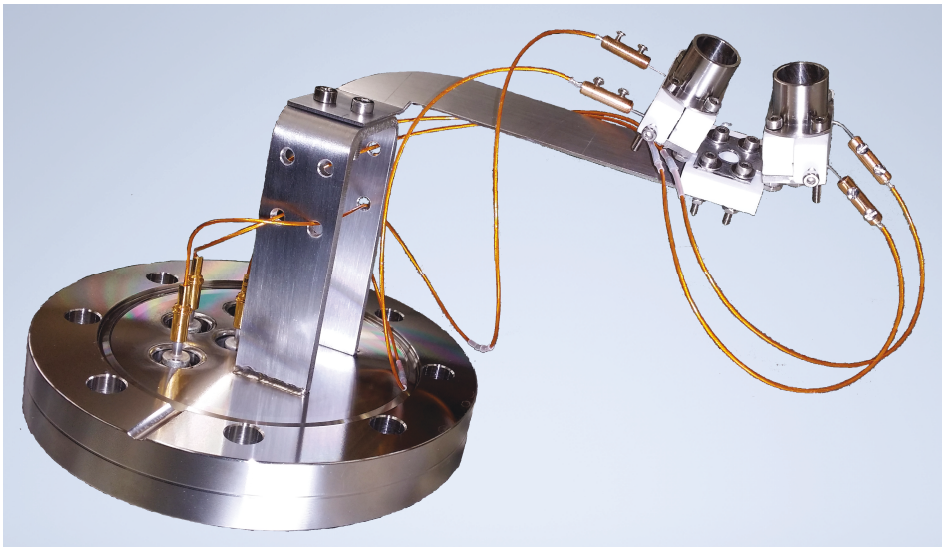

Figure 5.13.: Beryllium oven unit: The CF 63 flange makes replacement quick and convenient.

5.4. Beryllium Oven

The beryllium is vaporised in an oven and ejected through a slit cover towards the trap. In order to provide a large beryllium reservoir, two ovens are attached to one flange as shown in Figure 5.13. The latter allows an easy replacement. The ovens are arranged in such a way that an optical access to the trap remains guaranteed through a hole in the holder.

The oven content consist of a very pure beryllium wire (99.7 %) of 0.05 mm diameter. In order to be heated, the brittle beryllium is wrapped around a tungsten filament (tungsten 99.4 % / thorium oxide 0.6 %, diameter 0.1 mm). The production of the filament is explained in Appendix B. It is placed in a heating chamber made of Macor (Figure 5.14), in front of the slit (Figure 5.7). The counterpart of the oven, not shown here, can be seen in Figure 5.7 and 5.13. The thin and sensitive tungsten filament is electrically connected to a thick tungsten wire, which is fixed in the oven with two screws.

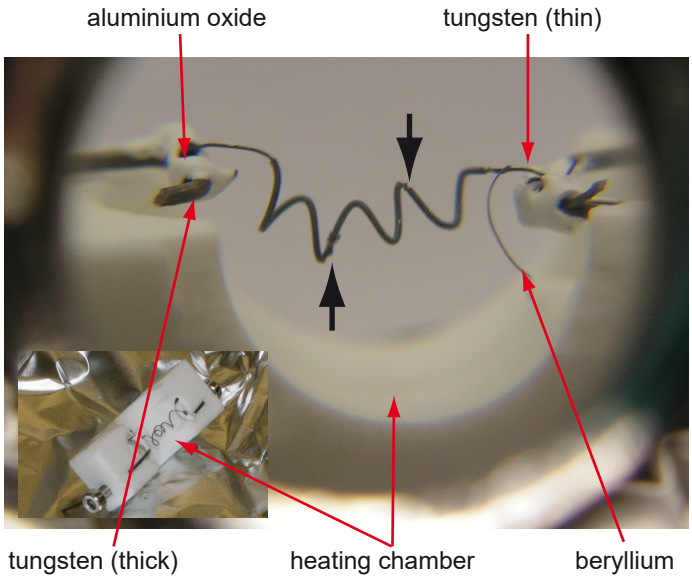

Figure 5.14.: Twisted tungsten filament in one half of the heating chamber. The filament is wrapped with beryllium. Enlarged view of the beryllium winding. The black arrows point to two major defects in the winding. The 50 µm thick overlength beryllium wire can be used as a scale.

A power supply slowly ramps up the current to the set point $I_{\text{set}} = 0.67\,\text{A}$ (emission threshold 0.55 A) by a remote control and keeps it constant, even if the electrical resistance changes due to heat-up effects. Either the user or finally a timer stops the heating process to avoid unintentional emptying of the oven. The current is also slowly reduced when the oven is switched off.

5.5. Further Components

This section gives a brief overview of the components of the system that have not been discussed so far.

Radiofrequency Antenna The radiofrequency antenna is part of the experimentation unit (Figure 5.6 and 5.7). It is a one loop antenna, which is placed 21 mm below the trap center. During development, care was taken to ensure that it is as broadband as possible. For this reason, the impedance must be adjusted when the frequency is changed.

Imaging Unit To image the ions, a lens system with a focal length of 36 mm is used. It consists of five lenses with a diameter of 50 mm. The numerical aperture is 1.2. To achieve the optimum resolution of 1 µm and magnification by a factor of 10, it is placed inside a tube (Figure 5.15) at a distance of 36 mm from the ion. The tube is located in a reentrant window and can be adjusted vertically with the aid

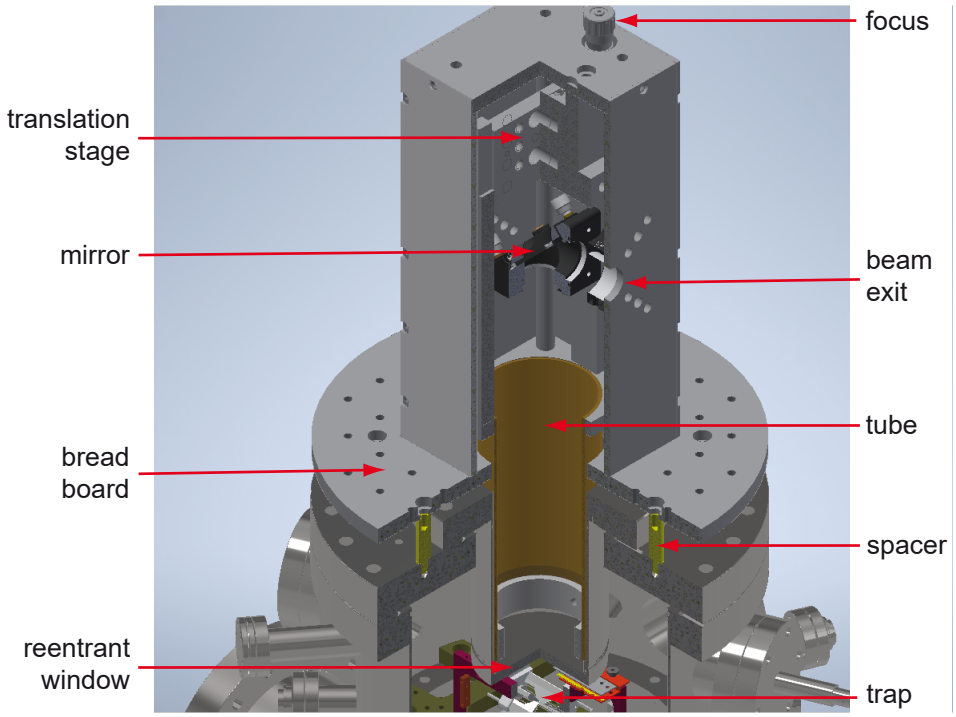

Figure 5.15.: Imaging path. A large reentrant window is placed just above the trap. The lens system (not shown) is clamped in a tube whose distance to the window can be adjusted with a translation stage. The beam is coupled out with a mirror. A beam splitter located on the breadboard and the PMT/camera are not shown.

of a translation stage. In order to prevent stray charges from being accumulated on the window, it is coated with a conductive indium tin oxide (ITO) layer.

The lens system including height adjustment is connected to a breadboard on which further optics are located. In the following, this unit is called the imaging unit. It is mounted with spacers on the lid of the vacuum chamber and can be easily removed during baking. The spacers are variable in height and allow the unit to be tilted freely in space.

The light emitted by the beryllium is collected by the lens system, deflected by a mirror and hits a pellicle beam splitter (not shown in Figure 5.15). The reflected part is imaged by a CCD camera (Andor iXon), while the transmitted part incidents on a PMT. There is a band-pass filter (Asahi Spectra, XHQA313) in front of the camera and the PMT. In this way, the PMT and CCD signal can be evaluated simultaneously.

Triaxial *Helmholtz* Coils Three pairs of rectangular *Helmholtz* coils are used to compensate for the existing magnetic field. On the other hand, they can be used to generate a well-defined magnetic field that defines the quantisation axis for the ions. This is required for a pure polarisation of the laser beams. The size of

the coils is chosen so that they fit into each other. The largest coil has 72 turns, the middle 64 turns and the smallest 40 turns. A Rohde & Schwarz HMP4030 power supply serves as a computer controllable current source for the magnetic field.

Compensation/End Cap Voltage Source The voltage supply of the compensation electrodes and the end caps consists of two digital analog converter (DAC) cards with a resolution of 16 Bit each. The first is for a coarse adjustment over the range of about ±35 V and the second is added with a range of ±3.5 V. Thus, in total a finer resolution than the 16 Bits is achieved. The hardware noise of about 4 mV is smoothed by a subsequent lowpass RC filter. Otherwise, the required very small secular excitation amplitudes of a few microvolts would be absorbed in the noise.

The identical voltage source for the end caps is enhanced to the required voltage with an additional voltage amplifier. The maximum achievable voltage is $U_{\mathrm{ec}} = 270\,\mathrm{V}$.

5.6. Laser Systems

The available lasers and their abbreviations are listed in this section (Figure 5.16).

Laser Cooling, *UV 3 / ULE* To drive a laser cooling transition as described in section 4.3, a 313 nm laser is required. In order to achieve a simultaneous cooling of the ion movement in the three spatial directions, the wave vector is oriented in such a way that its components in the directions u do not vanish. Since the coordinate system of the trap u is rotated around the trap axis by 45° with regard to the plane of the optical table, the beam is irradiated parallel to that plane. A further angle of 45° to the trap axis provides the axial component of the wave vector.

UV 3 is a commercial laser system. Two resonant doubling stages quadruple the frequency of a 1252 nm seed laser (Figure 5.16, *Doppler*-cooling laser & repumper). Between the two doubling stages there is an EOM, which can generate Δ =14.188999 GHz sidebands to the frequency-doubled beam at 30 dBm maximum rf input power. The sideband frequency is chosen to be a multiple of the free spectral range of the second cavity. In the non-linear crystal of the second stage, sum frequency generation takes place between the strong carrier and the carrier or a sideband.

If the seed (carrier) frequency is set to the frequency $\omega_0/4 \pm \Delta$ of the atomic

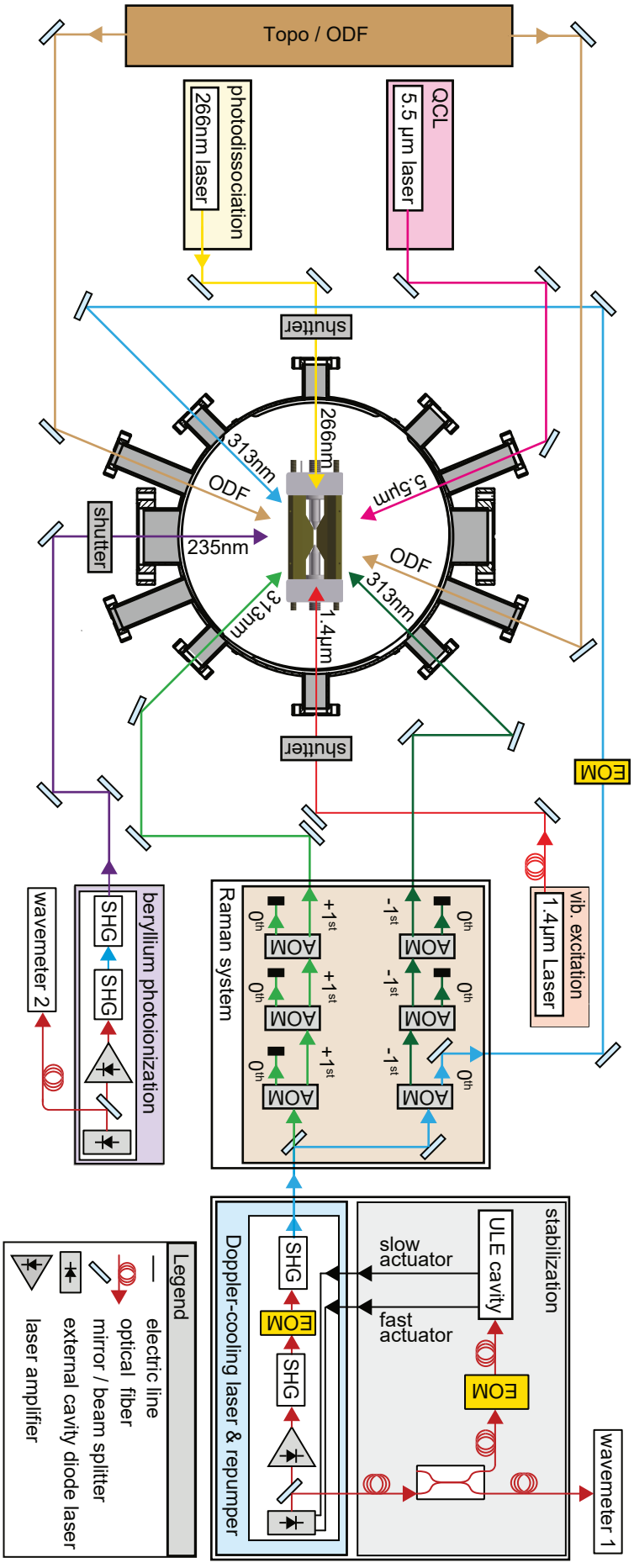

Figure 5.16.: Simplified overview of the present laser systems.

beryllium transition, the imprinted sidebands can be used for *Doppler* cooling. This allows a fast switching between *Doppler* and *Raman* cooling, where the *Raman* process is determined by the detuning Δ. Therefore, the up to 300 mW 313 nm radiation is directly coupled into the *Raman* system where it is split into the *Doppler* and *Raman* cooling branches (see "Sideband Cooling, *Raman System*"). By utilising one of the AOMs there, a fast power stabilisation can be implemented in addition to the slower, internal power stabilisation of UV 3. A second EOM is located further along the *Doppler* cooling beam path, which generates 1.25 GHz sidebands on the 313 nm carrier. A manual power control consisting of a lambda-half wave plate and polarising beam splitter cube is followed by a lambda-quarter wave plate. With the latter, a pure $\sigma^{\pm}$ polarisation of the light can be achieved in front of the vacuum window.

The seed laser is stabilised to an ultra low expansion (ULE) cavity[1]. For this purpose, a small percentage of the laser radiation is coupled into an optical fibre before it is amplified and frequency doubled (Figure 5.16, stabilisation). The outcoupled radiation is further split, one half is used for the wavelength measurement with a wavemeter, the other half is used for the frequency stabilisation. For this purpose, the latter is phase modulated with an EOM. The sidebands are used for locking UV 3 to ULE with a double-modulation technique [66]. The sideband frequencies, which can be very accurately adjusted with a DDS, allow a precise UV 3 frequency setting. In the locked state, the frequency can be detuned by about 300 MHz (200 kHz step size) without any mode jump[2]. For the light converted to UV, this almost corresponds to the beryllium hyperfine splitting. This locking technique has proven to be very robust. Usually, the laser does not need to be relocked during a working day.

If it is free running, then the line width is measuerd to be 500 kHz (FWHM). When it is locked to ULE, the linewidth of the central peak is 423 Hz (Figure 5.17).

Beryllium Photoionisation, *BePhI* For the photoionisation of beryllium, a 235 nm laser is required. A commercial 940 nm external cavity diode laser resonantly doubled to 470 nm is used as the basis for the BePhI system. There is also a small percentage of the 940 nm radiation being used for determining the wavelength. The setup of the second doubling stage (Figure 5.16, beryllium photoionization) is shown in Figure 5.18. After the 470 nm light is coupled out of the fibre, sidebands are imprinted with an EOM. These are used to stabilise the resonator

[1] The ULE system was built as part of another project and is described in [65].

[2] The mode jump-free tunability depends on the UV 3 seed mode. The range specified in [2] (Appendix A) could be significantly improved by optimising this mode.

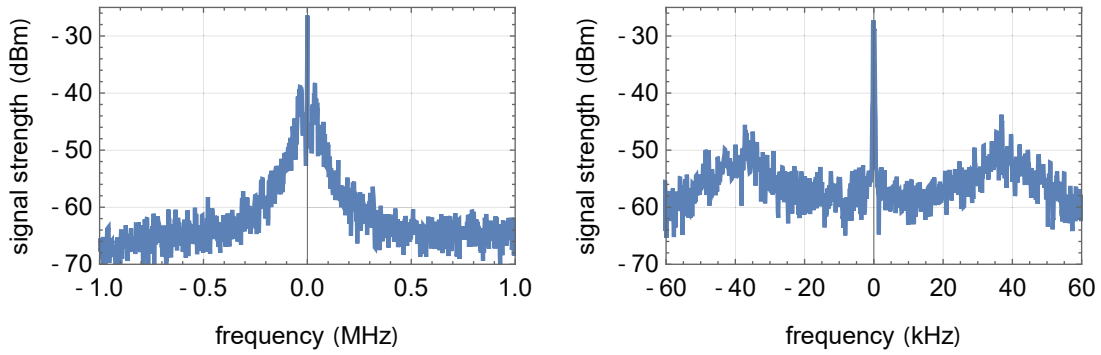

Figure 5.17.: Beat signal of the stabilised UV 3 with a stabilised (MOLO) optical frequency comb (RBW: 1 kHz (left), 100 Hz (right).

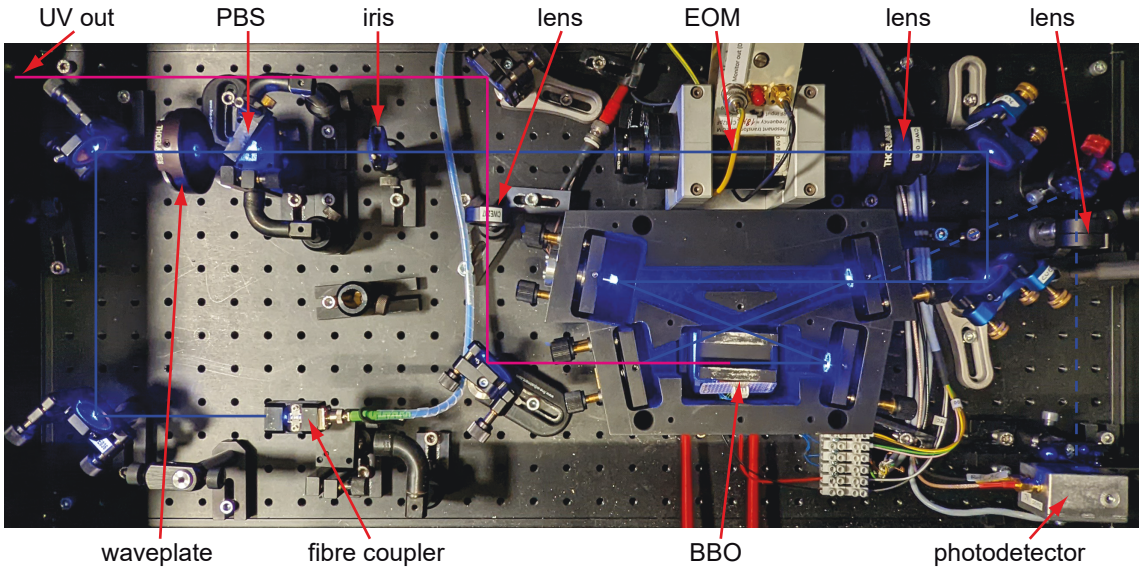

Figure 5.18.: Second doubling stage of the beryllium photoionisation (BePhI) source: Photographic overview complementary to the schematic Figure 5 in Appendix A. The BBO is located under the heat sink and not visible.

length to the laser. The frequency of the resonantly enhanced radiation is doubled in a beta barium borate (BBO) crystal. An active frequency stabilisation is not necessary because the *Doppler* broadening of the hot atoms is much larger than the drift of the seed laser. In this way, up to 12 mW 235 nm UV radiation can be generated with approximately 0.5 W 470 nm input radiation. The peak power drops to about 5.5 mW within a short time scale due to thermal effects. At this power level, it changes by ±10 % over a period of hours (Figure 6, Appendix A). For the application of photoionisation, 2.7 mW, measured behind the second window, after the radiation has passed the trap, is sufficient. In the figure it is not visible that a computer-controlled shutter is placed directly behind the UV out. As UV radiation can also be used to produce stray charges or discharge the trap structure, a continuous use should be avoided. Otherwise, the trap must be compensated again if necessary.

For practical reasons, the laser is irradiated perpendicular to the trap axis.

Sideband Cooling, *Raman System* To drive a transition that changes the motional state of the ion (Figure 4.1), two coherent laser beams with a frequency difference of 1.25 GHz and a detuning Δ of a beryllium resonance have to be generated. This is achieved by splitting a high-power UV beam (UV 3) into two branches and shifting each branch by ±625 MHz using three acousto-optical modulators (AOM) each (Figure 5.16, *Raman* system). The implementation of the system is shown in Figure 5.19.

The UV beam is coupled into the system at UV in and split into the two branches at the beam splitter (PBS). The transmitted/reflected part is shifted by 200 MHz at AOM1$^{\pm}$ (Gooch & Housego, Type I-M200-3C10BB-3-GH27). In the further path of the reflected beam, the zero order of AOM1^{-} is extracted and is used as a *Doppler* cooling beam (carrier out). The first diffraction order of both beams is again diffracted in first order at the other two following identical AOMs, AOM2$^{\pm}$ and AOM3$^{\pm}$ (Gooch & Housego, Type 35210-BR). The AOMs are operated simultaneously at 212.5 MHz. If necessary, one of the AOMs in each branch can also be used for power stabilisation, similar to the carrier output.

The exact timing of the *Raman* beams, their frequencies and intensities are controlled by an FPGA. This controls a 4-channel DDS (Analog Devices, Type AD9959) whose signal is distributed to the AOMs through a cascade of power amplifiers and splitters. The FPGA can be controlled by a simple script programming language via LabView.

With the setup presented here, the possible diffraction efficiency per branch is more than 40 %.

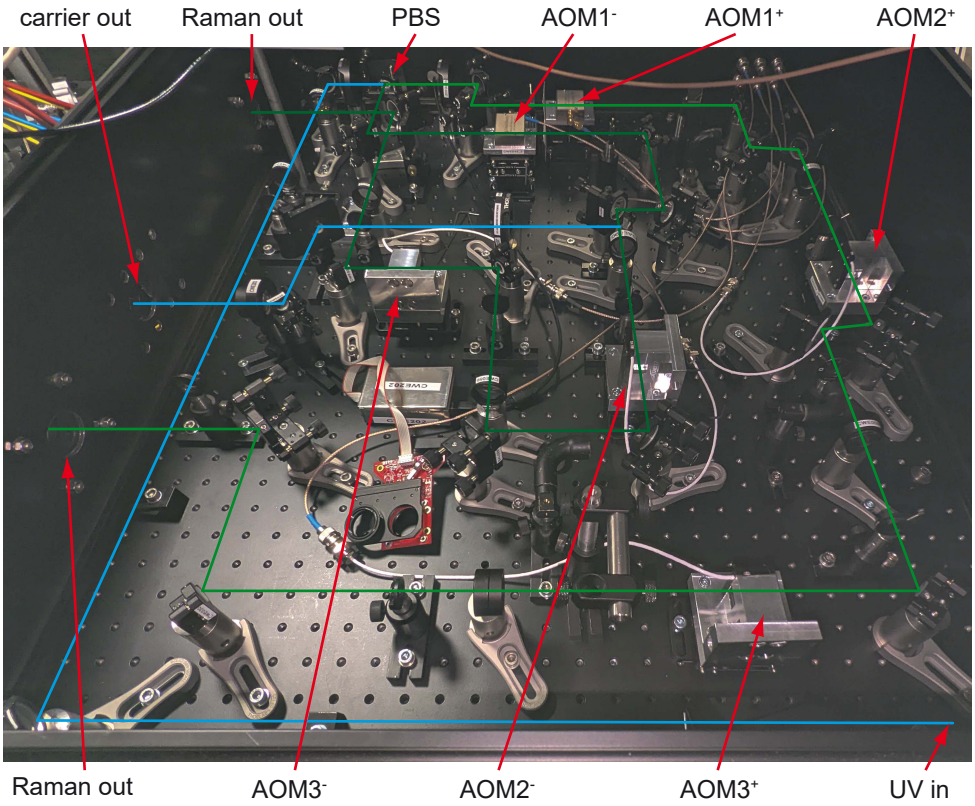

Figure 5.19.: *Raman* system: The explanation is in the main text.

To achieve the required polarisations, the σ^+ beam must be irradiated in the counter direction to the *Doppler* cooling beam, while the π beam is perpendicular to it. The corresponding wave vector points along the trap axis.

Optical Parametric Oscillator, *Topo* For precision spectroscopy, an optical parametric oscillator is needed, which should address three main applications: (i) non-destructive detection of the internal state of HD^+ by the optical dipole force (Section 9.1), (ii) internal state preparation of HD^+ and the homonuclear hydrogen molecule ions H_2^+ and D_2^+ (Section 8.4) and (iii) feasibility studies on novel transitions. The conception of these experiments (Section 9 and 8.4) and the application for the laser system (Toptica, DLC TOPO in combination with DLC CTL 1050) are part of this work, while the commissioning and implementation is part of another project.

To generate the running standing wave for the ODF, the two beams of the Topo are irradiated in counter direction at 67.5° to the trap axis.

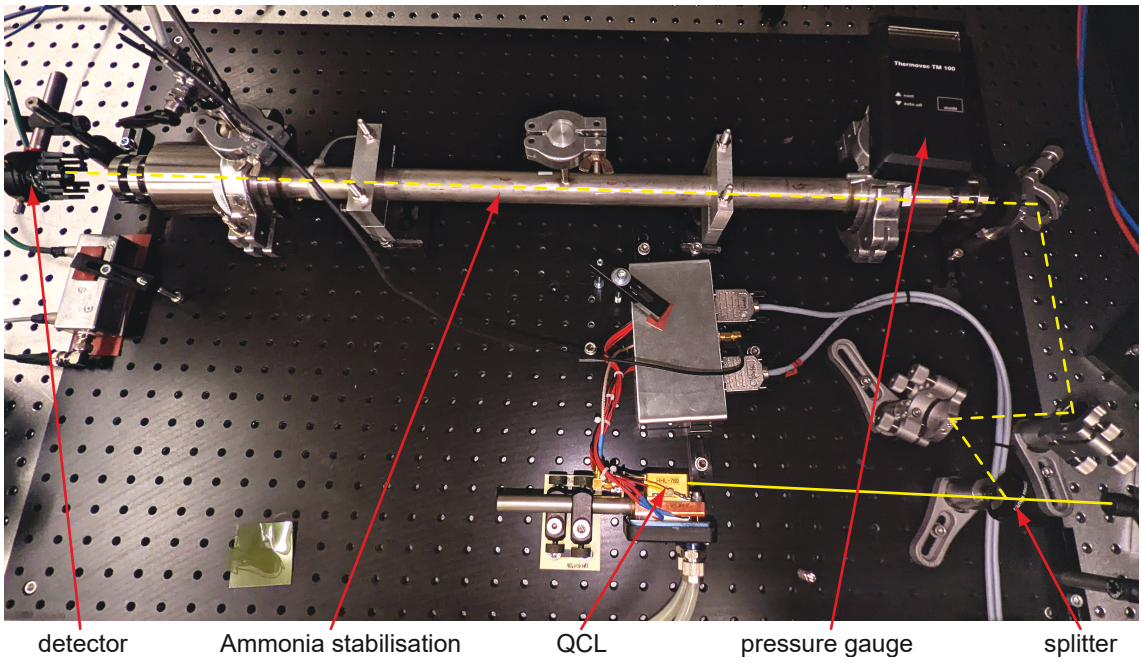

Figure 5.20.: QCL with gas cell for the iodine stabilisation: The dashed path is used to stabilise the QCL.

Rotational Cooling, *QCL* For quantum state preparation the rotational cooling $(v=0, L=2) \rightarrow (v=1, L=1)$ at 5.5 µm has to be implemented. A quantum cascade laser (QCL, Alpes Lasers, ALP-RT-CW-DFB-LP-SM) stabilised to an ammonia absorption line is used. The system is shown in Figure 5.20. The system was build by *G. Giri* and is shown here only for the sake of completeness.

Molecular Photodissociation, *266* From the fourth excited vibrational state $v=4$, HD^+ molecules can be efficiently excited into the anti-binding $2p\sigma$ state with 266 nm radiation. For this purpose, a commercial 532 nm source is resonantly doubled. The photodissociation is used to check the system's performance and is not intended for permanent use. Therefore, the radiation is coming free-space from the first ion trap experiment as indicated in Figure 5.1. The maximum intensity is limited to $I_{266} = 60\,\mathrm{mW/mm^2}$.

Laser for Spectroscopy, SL The laser is used to excite the HD^+ molecular state $(v=0, L=1) \rightarrow (4,0)$ at 1420 nm. A commercial diode laser is used for this purpose. The laser is actively broadened to a linewidth of approximately 50 MHz so that it can excite the most intense hyperfine components of the rovibrational transitions simultaneously. This fibre-coupled laser achieves an intensity $I_{1420} = 5\,\mathrm{mW/mm^2}$.

6. Experimental Procedures

At the start of each experiment, different ion species has to be loaded. A practical procedure is to load the beryllium ion first, as it cools the other species and is also used for diagnostic purposes. The necessary steps are explained in this chapter.

6.1. Beryllium Loading Schemes

The beryllium ion must be trapped and fluoresce so that it can be observed. This process is enhanced by *Doppler* cooling as the kinetic energy is reduced. Phase transitions occur and the previously diffuse distribution of the ion becomes increasingly localised. The ion crystallises and the fluorescence increases. Therefore, the choice of a suitable cooling and repumper scheme is crucial for the successful trapping of beryllium ions.

Four different scenarios are possible for the beryllium trapping, which are illustrated in Figure 6.1. Options A or C are the most commonly used.

Scheme A This scheme features a strong repumper (UV 3 carrier frequency). The EOM generates a weak sideband that is used for *Doppler* cooling. Because of the strong carrier's 1.25 GHz detuning, the hot and therefore energetic beryllium ions can be captured efficiently. Since a mode hop free tuning of the locked laser to scheme B is not possible, this scheme is suitable for the initial commissioning and alignment of the imaging optics. Scheme A is particularly useful because with the other schemes the ion must be very well controlled.
Due to the way the wavemeter is calibrated, there is a measurement error in the wavelength measurement. To adjust the laser to the atomic resonance frequency, the following procedure must be followed: If a laser (third harmonic, 574437.959 GHz) stabilised to the molecular iodine transition P58(2-49) is used to calibrate the wavemeter with its fundamental at 1.566 µm, then the UV 3 seed frequency should be set to 239348.9578 GHz.

Scheme B If the functionality of the sideband and the carrier are exchanged in comparison to scheme A, scheme B results. The scheme is an intermediate step to scheme C, as the EOM has a frequency dependent characteristic (Section 7.5).

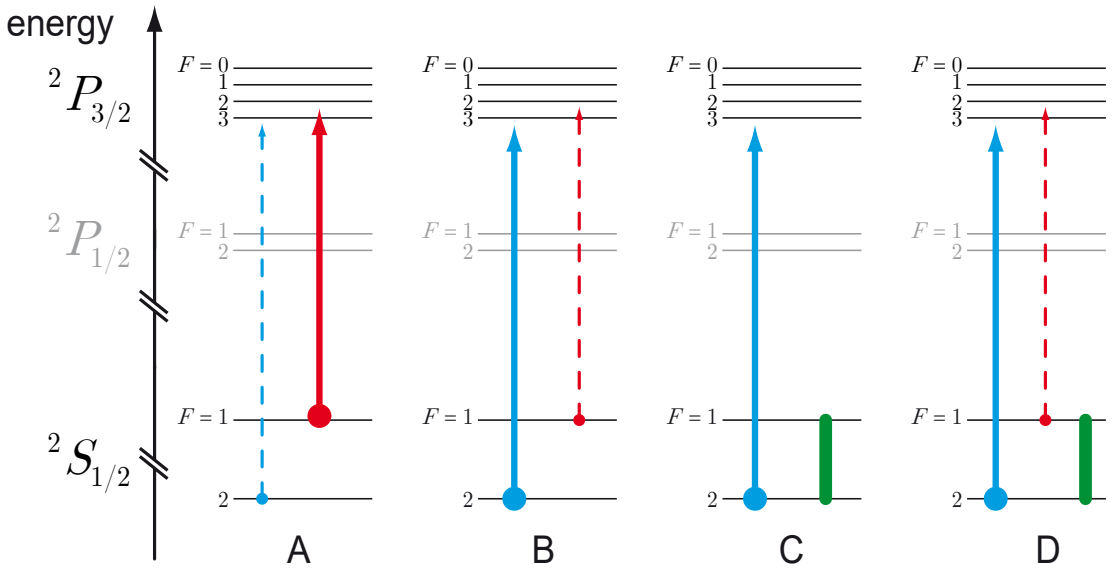

Figure 6.1.: Laser settings for different beryllium loading schemes (A to D): The continuous arrow symbolises the *Doppler* cooling or repumper transition (blue/red) driven by the UV 3 carrier frequency. Sidebands of the external EOM are shown with dashed lines. The microwave transition for repumping is shown in green.

The powerful carrier frequency drives the *Doppler* cooling transition, while the weak sideband of the EOM does the repumping. For loading, the seed laser frequency should be redshifted by about one trap frequency ($\tilde{\Omega}$ = 35.8585 MHz), although it is also possible (but slow) for a 10 MHz shift from the resonance frequency 239349.2856 GHz. A total power of 6 µW in front of the window is sufficient for trapping. Overall, this scheme is more susceptible to interference: The external magnetic field defining the quantisation axis must be carefully adjusted and a miscompensation of the trap will prevent successful trapping.

Scheme C Here, the sidebands (scheme B) are replaced by microwave radiation for repumping. Since the M1 transitions are very narrow-band, the microwave frequency must be well matched to the applied magnetic field strength. In order to be able to detect the effect of the microwave radiation, the *Doppler* cooling transition must not be driven too strongly (< 1 µW). Otherwise, the ion can be observed even without a repumper (for example, while loading; see scheme B). This scheme was used for the rf spectroscopy of beryllium.

Scheme D For efficient repumping, the microwave radiation and the sideband of the EOM can be used simultaneously.

6.2. Beryllium Trapping

To avoid unwanted stray charges, beryllium atoms should be ionised exclusively by photoionisation using BePhI (Section 5.6). The effect of a ten-second bombardment with the electron gun is illustrated in Figure 6.9. The initially small amplitude modulation of the fluorescence shown in the right sub-image has increased significantly afterwards (left). After using the gun, the trap must be compensated again (Section 6.5).

Neutral beryllium atoms are therefore ionised by a 2-photon process according to the procedure described in [67]. The atom is first resonantly excited from $2s^1S_0$ to $2p^1P_1$ with one photon (BePhI) and then ionised with a second photon of same wavelength.

After the loading process has been started, the beryllium oven heats up for 20 seconds before sufficient beryllium vapour is emitted. Then BePhI is activated through a shutter. The neutral beryllium can be loaded with at least 2.7mW (typically 4.7mW) measured behind the vacuum chamber within a few seconds (according to the selected loading scheme). Depending on the UV 3 red detuning and power, but also on the depth of the trap potential, the ion crystallises immediately and becomes visible on the CCD camera.

The trap potential should be first set so that $\omega_{x,y}^{(1)} = 2\pi \cdot 0.8\,\mathrm{MHz}$ and $\omega_z^{(1)} = 2\pi \cdot 0.2\,\mathrm{MHz}$. This corresponds to a monitor output $U_{\mathrm{Out\,A}} = 6.64\,\mathrm{V}$, $U_{\mathrm{Out\,B}} = 6.32\,\mathrm{V}$ and an end cap voltage $U_{\mathrm{ec}} = 3\,\mathrm{V}$. If the ion does not crystallise immediately, at least a slight increase in fluorescence can be detected with the PMT. In both cases, the loading process is stopped manually. The oven temperature slowly decreases and BePhI is paused. The crystallisation process can be supported by varying the trap parameters.

If a larger number of ions is trapped than required, it is possible to remove excess ions by reducing the radial trap potential. The equilibrium positions of the ions change from an axially oriented string to a string rotated by 90°. The ions located furthest away from the trap axis are heated the most due to the micromotion and can escape the trap potential. In about half of the cases, all but one beryllium ion can be removed in this way.

6.3. Secular Excitation

The secular excitation method is a powerful diagnostic tool. It can be used to measure the trap potential or to draw conclusions about the stored ion species.

By applying an alternating voltage of a few mV to one of the two end cap or compensation electrodes, the ion(s) can be excited to axial or radial oscillations. This requires

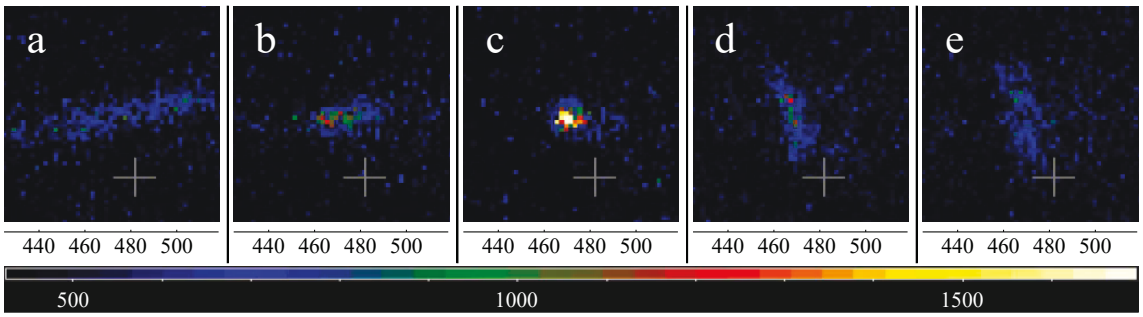

Figure 6.2.: Forced axial and radial secular oscillation for different excitation amplitudes (Figure 8 of [2], Appendix A). Explanation in the main text.

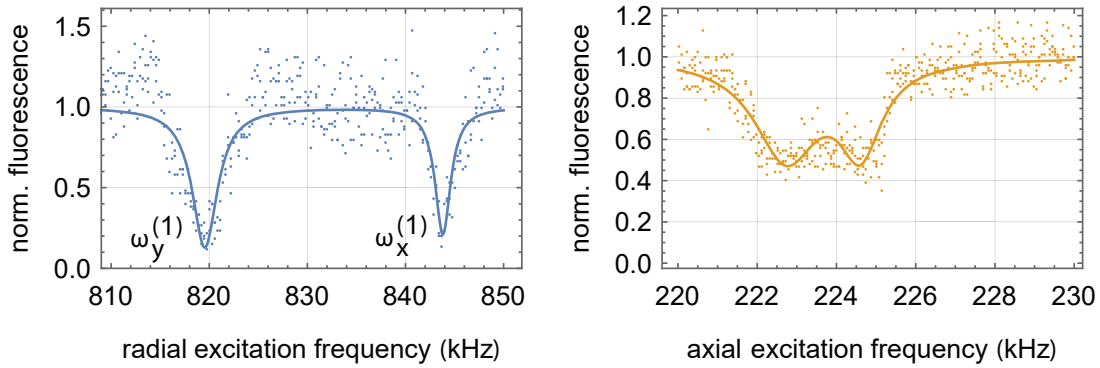

Figure 6.3.: Typical radial and axial secular scans of a single beryllium ion.

the ac voltage frequency to match the secular frequency of the ion (system). Figure 6.2 shows the axial and radial oscillatory excitation of a single beryllium ion for two excitation amplitudes. Panel c shows an overexposed ion at rest. Thus, in the case of oscillations, the much lower detected intensity per pixel is visible without adjusting the colour scale and a direct comparison of the different cases is possible. In panel a, the ion is excited to strong axial oscillations so that the fluorescence is reduced. It can be detected over a large pixel array. A weak excitation (b) is also easily detectable with the camera. Panels d (weak) and e (strong) show radial excitations. The weak oscillations b and d do not show up in a decreased fluorescence signal with the PMT, while the strong oscillations do due to the *Doppler* effect.

If the excitation frequency is scanned continuously in order to find the ion's resonance frequencies, this is referred to as a secular scan. Such a secular scan is shown in Figure 6.3. Each data point is the average over 100 ms of the PMT signal. Due to the design of the trap drive, the two radial secular frequencies are not degenerate. The axial line shape clearly deviates from the expectation. It appears as if there are two closely spaced axial resonance frequencies. The shape shown here is typical for the

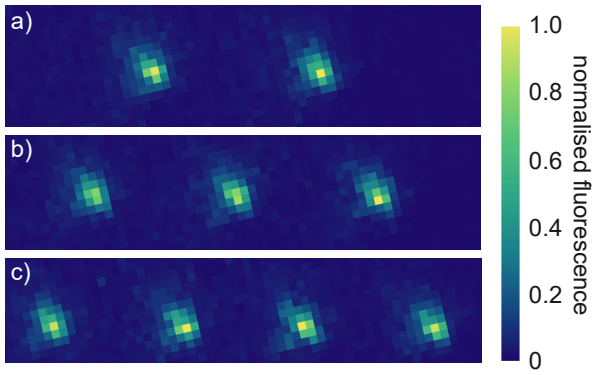

Figure 6.4.: Three typical beryllium ion strings for the same trap parameters. Cases a) to c) are normalised to its maximum fluorescence (Figure 4 of [2], Appendix A).

case	distance (pixel)	calc. distance for $\omega_z^{(1)}$ (µm)	fraction (µm/pixel)
a)	20.6(2.1)	11.389(21)	0.55(6)
b)	17.7(2.1), 17.5(2.1)	9.737(18), 9.737(18)	0.55(7), 0.56(7)
c)	15.5(2.1), 14.3(2.1), 16.5(2.1)	8.880(16), 8.215(15), 8.880(16)	0.54(7), 0.57(9), 0.54(7)

Table 6.1.: Calibration of the imaging unit with the help of Figure 6.4.

axial excitation in the new trap and leads to an enlarged uncertainty in the axial secular frequency $\omega_z^{(1)}$. Noticeable is also the large spread of the data points that will be discussed in Section 6.8.1.

6.4. Detection with the CCD Camera

The CCD camera images of three typical ion strings are shown in Figure 6.4. The ion positions are defined as the pixels with the locally highest intensity. The measurement uncertainty is estimated to be 1.5 pixels. To calibrate the imaging unit, the distance between the ions can be measured and compared with the calculated equilibrium positions (scaling factor $l = 9.039(17)$ µm, Equation 2.25). Here, the applied axial trap potential is determined by the oscillation frequency $\omega_z^{(1)} = 2\pi \cdot 727(2)$ kHz of a single beryllium ion. The evaluation is summarised in Table 6.1. This results in a mean conversion factor of 0.55(3) µm/pixel. In principle, spatial information can also be obtained from a calibrated PMT signal. This is possible because the number of beryllium ions determines the measured fluorescence intensity. In the case of two different stored ion species, their total number must be known. It can only be determined with the CCD camera: For this purpose, the ion positions of a pure beryllium string for different ion numbers must be matched with the positions of the visible beryllium ions of the mixed

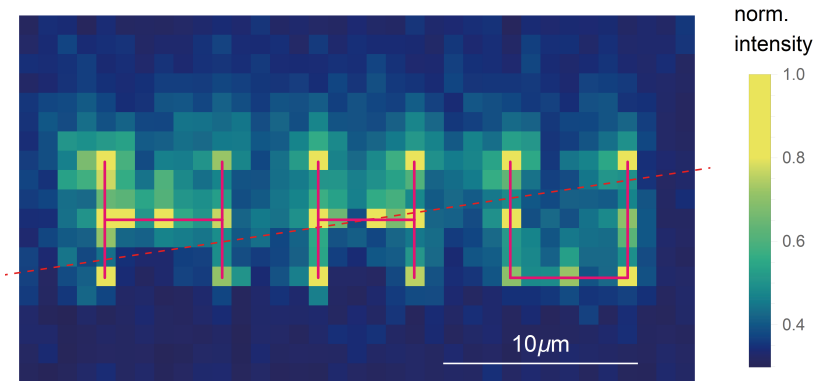

Figure 6.5.: *HHU* logo: Normalised image composed of 21 normalised images of a single beryllium ion. The trap axis is shown as a red dashed line.

string. If UV 3 does not illuminate the string uniformly, a specific fluorescence level can be assigned to each arrangement of ions. In practice, however, this complicates the evaluation of the secular scans. Figure 8.2 shows this using the example of a Be^+ - HD^+ system.

6.5. Compensation of Stray Charges

The ions can be displaced by applying a dc voltage to the compensation electrodes. When minimising the micromotion, the ions are pushed onto the trap axis by applying a compensation voltage. With the horizontal electrode, the ions can be moved in the image plane of the camera and with the vertical one perpendicular to it. Since the trap is described in a coordinate system rotated by 45°, both electrodes have a simultaneous influence on the ion position in respect to $u = x, y$. This fact complicates minimisation of micromotion. The compensation is achieved with a two-stage procedure in which the trap is first roughly compensated and then a fine compensation is carried out with a time-resolved evaluation of the fluorescence signal.

The effect of the electrodes is shown in Figure 6.5. If the end cap potential is also adjusted, the ion can be moved to any position within a certain volume. In this way, a lettering can be created. The letters *HHU*[1] is composed of 21 images of a single beryllium ion. Each individual image is normalised to the maximum of the fluorescence and added to the other images. The resulting image is normalised to its maximum. Since the camera orientation is slightly tilted to the trap axis, the latter is additionally indicated as a red dotted line. A total of two ions were used for the figure.

In terms of cooling efficiency and storage time, the ions should be pushed on the trap axis.

[1] Logo of the *Heinrich-Heine University*.

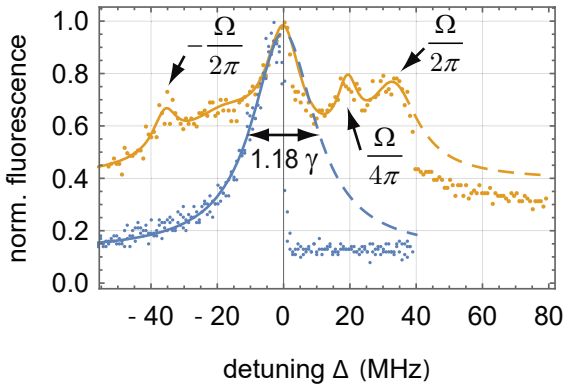

Figure 6.6.: Beryllium fluorescence for a well-compensated trap (blue) and for an uncompensated trap with sidebands at the trap frequency $\widetilde{\Omega}$ (orange). The detuning is defined in respect to maximum fluorescence (Figure 9 of [2], Appendix A).

6.5.1. Beryllium Fluorescence Pattern

The intensity pattern of a fluorescence spectrum for a beryllium ion in a compensated trap is *Lorentzian*-shaped. Depending on the laser power and ion temperature (as well as other factors), the line width may deviate from the natural line width of the P state. Figure 6.6 shows such a spectrum with a slight power broadening of 18 percent in respect to the natural line width (blue trace). For laser frequencies close to the atomic resonance frequency, the laser cooling is not efficient enough to keep the ion in a crystalline state. For positive detunings, the ion is heated. This leads to an abrupt change in fluorescence at $\Delta \lesssim 0\,\mathrm{MHz}$.

If the ion is not on the micromotion-free trap axis (Section 2.1.1), the fluorescence signal is superimposed by sidebands at the trap frequency $\widetilde{\Omega}$ (orange trace in Figure 6.6). The competition between cooling and heating leads to the spectrum shown. Here, the phase transition of the ion occurs for frequencies higher than the trap frequency. The sideband at $\widetilde{\Omega}/2$ is not fully understood and could be from a parametric excitation.

The aim of the trap compensation is to minimise those sidebands. This type of spectra gives a first indication of the trap's compensation status.

6.5.2. Radial Compensation - Rough Method

Initially, the ions are stored under extreme conditions (large q and a parameter, Equation 2.10) and both parameters are reduced in a controlled way afterwards. The former is done by lowering the trap voltage U_{rf} and the latter by lowering the end cap voltage U_{ec}. Figure 2.1 shows that the stability region becomes narrower for small voltages. This means that the ion can only follow a closed path in the trap when the potential

approaches the ideal (Equation 2.6). To compensate the trap, the first step is to maximise the trap voltage $U_{rf} > 500\,\text{Vpp}$ while keeping the end cap voltage U_{ec} as small as possible. At the same time, the ion position on the CCD camera is observed. Due to the high radial and low axial confinement, the ion occupies a strongly localised position in the quadrupole potential minimum, which might be slightly shifted by the end cap potential. This is important for the vertical alignment. The lens system must be shifted so that the ion is in focus. If the radial confinement is then released, the ion moves to a new position. In addition to the easily observed horizontal displacement, defocusing occurs. Next, the image is optimised by moving the ion back into focus with the vertical compensation electrode and then back to the position it occupied with the strong confinement with the horizontal compensation. If the radial potential is increased again, the shift of the ion position is significantly reduced. If necessary, the procedure must be repeated to iteratively eliminate the effect of the now changed compensation voltages.

6.5.3. Axial Compensation - Rough Method

After the radial compensation, the axial compensation can be carried out. This is more difficult from the beginning, as it is initially unclear how the end cap voltages must be chosen so that the ion is located in the geometric centre of the trap. Applying the voltage symmetrically is not necessarily ideal because of possible stray charges. As the end cap voltage increases, it becomes apparent that significantly higher vertical and horizontal compensation is required. It is an indication of radially asymmetrically mounted end cap electrodes. If these are oriented at an angle to the trap axis, this leads to a displacement of the ions from their optimal position, especially at high end cap voltages.

Example: With a symmetrically end cap voltage of $U_{ec} = 0.40\,\text{V}$, a horizontal compensation $U_H = 24.64\,\text{V}$ and a vertical $U_V = 3.70\,\text{V}$ are required, while at $U_{ec} = 280\,\text{V}$, $U_H = 19.30\,\text{V}$ and $U_V = 37.30\,\text{V}$ are already needed to push the ion back. However, with an asymmetric end cap voltage $U_{ec1} = 323\,\text{V}$ and$U_{ec2} = 316\,\text{V}$, storing an ion at $U_V = 19.30\,\text{V}$ and $U_H = 32.40\,\text{V}$ is possible.

The difference U_{ec1}-U_{ec2} mentioned here as an example is necessary due to intensive use of the electron gun, which has caused numerous space charges.

6.5.4. Time-Resolved Fluorescence Detection

A more sensitive methode of detecting mircomotion is by a time-resolved analysis of the fluorescence signal. In this time-consuming procedure, the micromotion is minimised iteratively by testing different compensation voltages as follows:

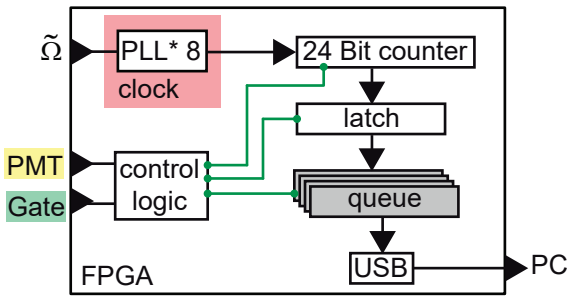

Figure 6.7.: FPGA schematic: A phase lock loop (PLL) generates the clock from the trap frequency $\tilde{\Omega}$ and synchronises the counter. If a gate signal is present and a PMT event is registered, the counter value is stored in the latch and transferred to the queue and the USB port.

With the help of a field programmable gate array[2] (FPGA), the photons are detected with a high bandwidth and mapped onto the phase of the trap electronics. The FPGA (Figure 6.7) has a bandwidth of 350 MHz, which means that 8 sample points can be recorded per trap drive periode. These are synchronised to the trap frequency $\tilde{\Omega}$ and phase. This clock signal ($8 \cdot \tilde{\Omega}$) defines the sample rate and thus the resolution.

The sample period is defined by the gate signal. If this is set to one tenth of the trap frequency, for example, then the events coming from the PMT are recorded for 10 trap cycles. Thus, a total of 80 sample points are recorded per gate period. Each data point consists of the event's rising edge time index related to the gate start time and is 4 bytes in length. The data transfer rate and the bandwidth are the limiting factor here. A gate frequency equal to one tenth of the trap frequency has proven to be practicable.

After events have been recorded for 10 trap cycles, the following 10 cycles are overlaid with the previously recorded ones and so on.

Figure 6.8 shows the result for a data acquisition time of 40 seconds for the three cases: uncompensated, partially compensated and almost entirely compensated trap. The relative fluorescence modulation with respect to the mean fluorescence can thus be significantly reduced by applying a few hundred mV to the compensation electrodes. For the change from the uncompensated to the partially compensated case, $\Delta U_{\mathrm{hor}} = -0.6\,\mathrm{V}$ and $\Delta U_{\mathrm{ver}} = +0.2\,\mathrm{V}$ have been applied, whereas for the almost compensated case it is $\Delta U_{\mathrm{hor}} = -0.2\,\mathrm{V}$ and $\Delta U_{\mathrm{ver}} = +0.2\,\mathrm{V}$. In the latter case, the modulation is 4(1) %.

In principle, the 10 cycles can be mapped to one cycle during the evaluation (Figure 6.9). A sinusoidal fit to the 8 data points leads to a relatively large inaccuracy in the trap frequency and is therefore not applied. A fit over 10 cycles reproduces it within a

[2] The software is based on a modified version of *Single Photon Counter* (NIST).

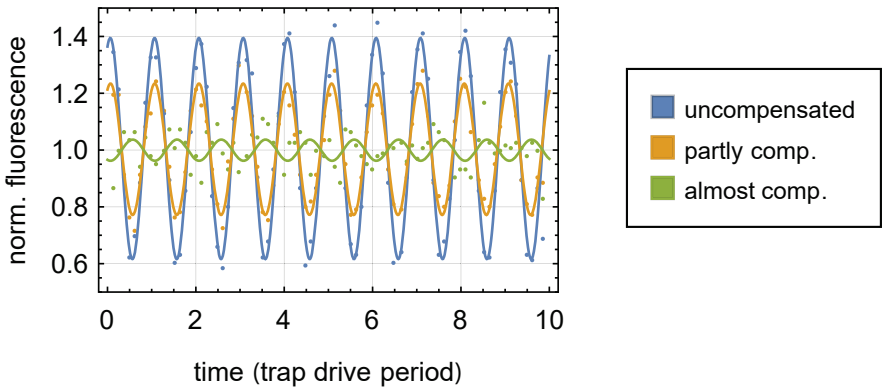

Figure 6.8.: Analysis of the micromotion for different compensation voltages. The lines are sinusoidal fits to the data (Figure 10 of [2], Appendix A).

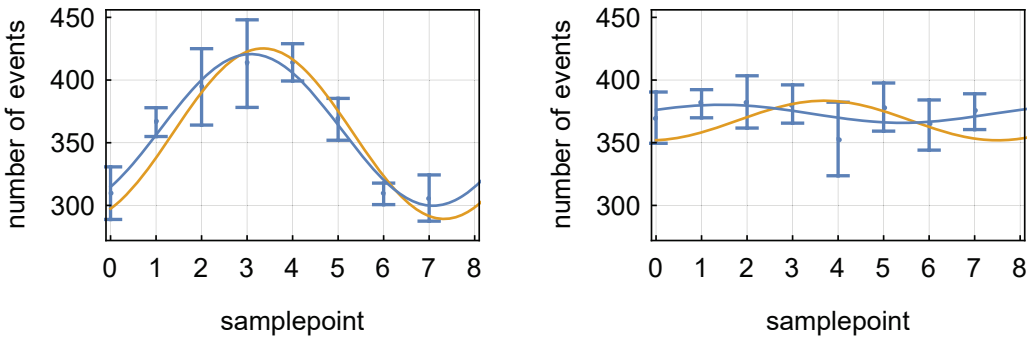

Figure 6.9.: Events mapped onto a trap cycle for an uncompensated (left) and very well compensated trap (right). A fit over several trap periods (blue, compare Figure 6.8) is plotted next to one for the raw data (orange).

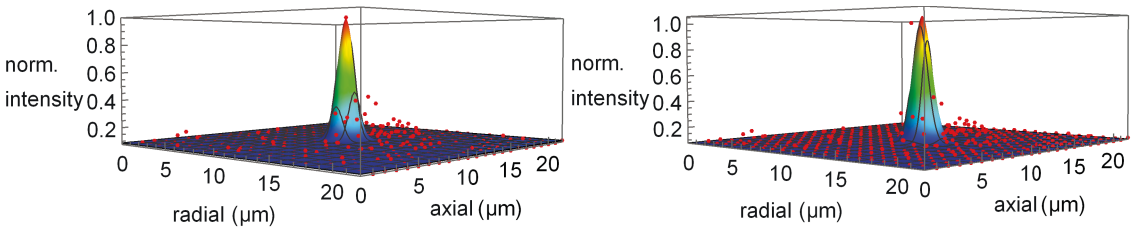

Figure 6.10.: Fit of a Gaussian distribution to the spatial intensity pattern (red dots) of the ion outlined in red in Figure 8.1. The left image corresponds to the beryllium ion on the left, respectively in the right image it is in its right place.

few 10 kHz. However, this depends on the compensation level. If the trap is very well compensated, the fit becomes less meaningful.

The frequency spectrum belonging to the right figure is shown in Figure 6.6 (blue).

6.6. Ion Temperature

A measure for the ion's kinetic energy is its temperature. It can be determined by the spatial imaging thermometry according to the method of [68]. For this purpose, a *Gaussian* distribution is fitted to the spatial distribution of the ion, as one would expect for thermal motion. As an example, the temperature for the two beryllium positions shown in Figure 8.1 is analysed and presented in Figure 6.10. Neglecting the imaging error (point spread function), this leads to an extension along the trap axis of 0.60(3) µm (left) and 0.72(2)µm (right). The extension perpendicular to it is accordingly 0.63(2) µm and 0.57(2) µm. The required root mean square width is conservatively overestimated by the FWHM width. Although the radial secular frequency is much higher, the expansion of the ion is similar to the axial one and therefore limited by the imaging system. For a more precise determination in the future, the sevenfold magnification triplet associated with the lens system must be used.

By substituting the thermal energy with the energy of the harmonic oscillator $\frac{1}{2}k_\mathrm{B}T = \frac{1}{2}m_\mathrm{Be}\left(\omega_{z,x}^{(1)}\right)^2 z^2$, the temperature T of the ions can be estimated. In this example it can be axially estimated as $T_{\mathrm{left},z} = 0.9\,\mathrm{mK}$ and $T_{\mathrm{right},z} = 1.3\,\mathrm{mK}$ (right). The temperature in radial direction is respectively $T_{\mathrm{left},x} = 1.0\,\mathrm{mK}$ and $T_{\mathrm{right},x} = 0.8\,\mathrm{mK}$. As expected, the effect of micromotion close to the trap axis is negligible.

In this case the analysis is of a single image. Along the trap axis there is a tail indicating high dynamics along the axis. This occurs when light molecules are stored next to beryllium (Section 8.1). An average over several images loses significance here. If only beryllium is stored, averaging over several images yields the axial temperature of 0.5 mK [2] indicating a very good *Doppler* cooling (Section 4.3.1). The averaged (axial)

motional state $\bar{n} \approx 5$ holds for ideal *Doppler* cooling. It can be calculated from the total oscillation energy in the (axial) trap potential, $E_{n,\mathrm{sec}} = \hbar\omega_{\mathrm{sec}}\left(\bar{n} + \frac{1}{2}\right) \stackrel{!}{=} k_B T_D$.

6.7. Mass Spectroscopy

The mass of co-trapped ion species can be deduced by a combination of the two detection methods, PMT and camera. In the first step, the number of stored ions has to be determined. For this purpose, the positions occupied by the beryllium ion are compared with the expected positions for two, three or a N-ion string (Figure 6.4). If the number is known, the expected secular frequencies can be calculated for different masses (Section 2.2.1) and compared with a secular scan.

An important example is discussed in Chapter 8.2.

6.8. Comments

To conclude this chapter, two points need to be made. Firstly, the cause of the fluorescence noise is unclear and should be discussed, and secondly, an increase in the signal to noise ratio should lead to a better fit result.

6.8.1. Fluctuation of the Detected Fluorescence

The fluctuation of the detected fluorescence can have a variety of causes, which must be excluded successively. The obvious explanation is a fluctuation of the laser power. The slow (internal) power stabilisation of the laser, as well as a fast stabilisation by using the AOM built into the *Raman* system does not show any significant improvement, at least not in the order of magnitude detectable here.

The trap drive in use could have a negative effect on the ions, which is noticeable in the modulation of the fluorescence. It was developed as a prototype for initial tests and should be replaced by a new one. The prototype's monitor output shows an imbalance of the trap voltage for the two branches, possibly because the resonant frequency of the circuit is different for the branches. An adjustment is not available due to its design. An example of a fit to the measurement data for five radial secular scans is shown in Figure 6.11. The higher frequency oscillation mode shows a larger linewidth (4(2) kHz) and a larger uncertainty in the centre frequency $\omega_x^{(1)} = 2\pi \cdot 617.9(7)$ kHz compared to the second radial mode ($\omega_y^{(1)} = 2\pi \cdot 563.6(3)$ kHz, linewidth 2.7(7) kHz) for a mean monitor output $U_{\mathrm{rf},x} = 4.60$ V and $U_{\mathrm{rf},y} = 4.28$ V.

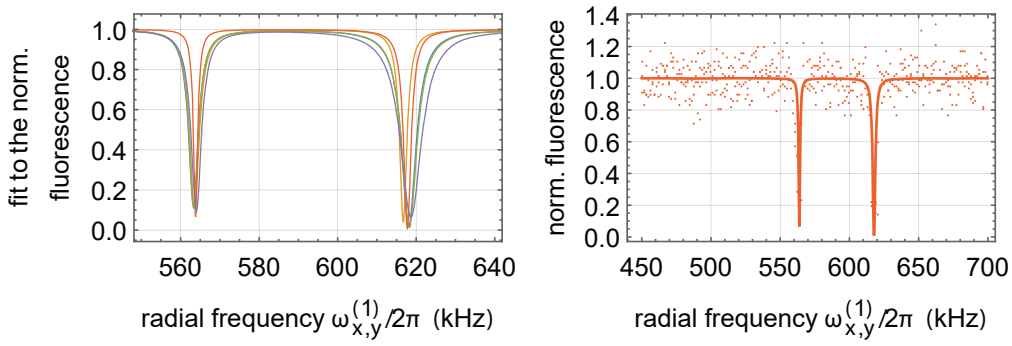

Figure 6.11.: Fit to five radial secular frequency measurements (left). The raw data and the fit for one of the cases are shown on the right.

The stored ions undergo chemical reactions, as shown for the case of the MHI (Section 8.3). This also applies to beryllium. A sudden disappearance of the beryllium ion does not necessarily mean a loss out of the trap. Sometimes it can be restored by a dissociation process using the UV 3 or BePhI laser at a high power. The influence on short time scales of the interaction with the residual gas on the fluorescence intensity is unknown.

6.8.2. Improvement of the Signal to Noise Ratio

At present, the scattered light coming from the experiment is split into two beams; one is used to image the ions with the camera, the other is detected with the PMT. The use of a latest generation camera with the possibility of single photon counting allows both detection methods with only one imaging path. This doubles the number of fluorescence photons. In addition, stray light from the trap structure can be masked by selectively reading out the pixels (region of interest). A significant improvement in data quality is expected.

7. Radiofrequency Spectroscopy of Beryllium

Hyperfine spectroscopy of beryllium is an important diagnostic tool to determine the magnetic field strength at the location of the ions. The results and experiences from beryllium spectroscopy are therefore of particular relevance for the upcoming precision measurements at the MHIs: The contribution of the *Zeeman* effect to the MHI is of comparable order to that for beryllium, since the spin of one unpaired electron is present in both ion species. Therefore, the beryllium spectroscopy serves as a test of the rf antenna and its settings. Here it is primarily necessary to measure the transition frequency, whereby the line width has a secondary relevance (precision measurements regarding this can be found in [69]).

7.1. Beryllium Hyperfine Transitions

The beryllium energy levels split in a magnetic field according to the *Zeeman* effect. The resulting transition frequencies between the two hyperfine states of the beryllium ion in the ground state can be calculated with the *Breit-Rabi* formula (Equation 4.1) as a function of the magnetic field strength. The calculation result is shown in Figure 4.2 for the relevant strengths of a few Gauss.

Normally three of the seven possible transition frequencies are detected. In rare cases, there may be four.

A spectrum with four transitions (A to D, example 1 in Table 7.1) for the coil currents $I_x = -500\,\mathrm{mA}$, $I_y = -470\,\mathrm{mA}$ and $I_z = 800\,\mathrm{mA}$ is shown in Figure 7.1. It is generated using the procedure from Section 7.2. The *Doppler* cooling beam wave vector is inclined at 45° to the x-, y-and z-axis. Here the selection rules $\Delta m_F = 0$ for $\boldsymbol{B}_{\mathrm{rf}} \parallel \boldsymbol{B}$ and $\Delta m_F = \pm 1$ for $\boldsymbol{B}_{\mathrm{rf}} \perp \boldsymbol{B}$ apply with the orientation of the rf magnetic field $\boldsymbol{B}_{\mathrm{rf}}$ in respect to the external magnetic field direction $\boldsymbol{B}$. The good signal to noise ratio is because in this case four trapped beryllium ions were examined.

line	frequency (MHz)	FWHM (MHz)	transition		rf polarisation
			$F' = 1$	$F = 2$	
example 1					
A	1250.15(7)	0.39(26)	$m_F = 0$	$m_F = 0$	π (weak)
B	1251.325(6)	0.336(19)	$m_F = -1$	$m_F = 0$	σ^-
C	1252.554(8)	0.380(28)	$m_F = -1$	$m_F = -1$	π (strong)
D	1253.820(21)	1.23(10)	$m_F = -1$	$m_F = -2$	σ^+
example 2					
E	1246.60(4)	1.12(16)	$m_F = 1$	$m_F = 2$	σ^-
F	1247.740(19)	0.22(6)	$m_F = 1$	$m_F = 1$	π
G	1248.961(8)	0.220(20)	$m_F = 1$	$m_F = 0$	σ^+

Table 7.1.: Evaluation of the spectrum shown in Figure 7.1 and 7.3. The transitions are illustrated in Figure 7.2.

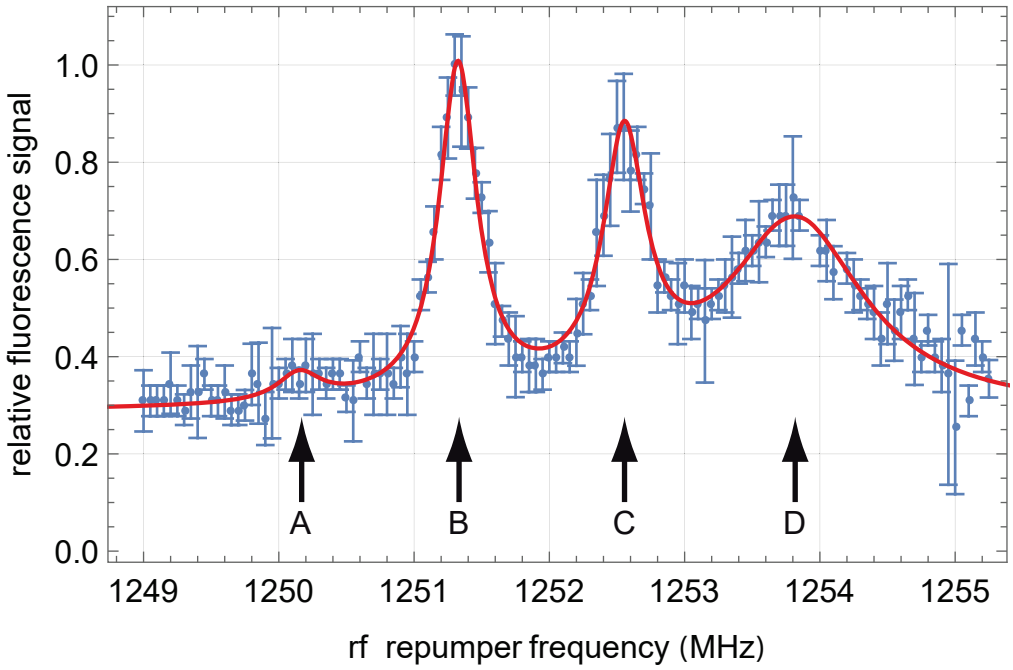

Figure 7.1.: Example 1: Spectrum of the M1 transitions for the hyperfine components of beryllium, which are separated in an external magnetic field. Four ions are stored in the trap for the measurements. A four *Lorentzian* fit to the data is shown in red (see also Table 7.1). The four detected lines are labelled A to D.

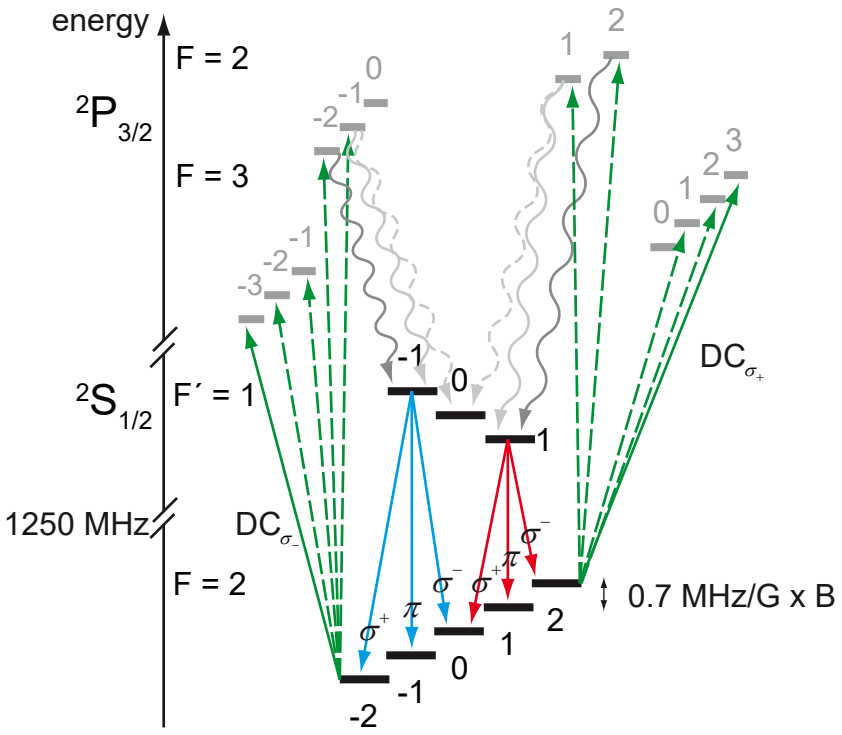

Figure 7.2.: Energy diagram and possible transitions for strong optical pumping into the states with maximum projection quantum number $m_{F=2} = \pm 2$: The *Doppler* cooling transitions (continuous green, dashed: further excitation possibilities for non-perfect polarisation) and the resulting rf spectrum (*Doppler* cooling polarisation σ^+(red), σ^- (blue)). Spontaneous emission from the states $^2P_{3/2}$ ($F = 2$) are shown in gray. The less frequent transitions are shown dashed. The three rf transitions starting from $(F' = 1, m_F = 0)$ are not shown for clarity.

The very weak line A (and the absence of the other transitions, not shown) indicates a very good optical pumping into the state with maximum projection quantum number $F = 2$, $m_F = -2$ (Figure 7.2). A general trend is that the line width becomes narrowest for the line closest to the clock transition (line A) and broader for the other. This applies analogously to the spectrum with a σ^+ *Doppler* cooling beam. Example 2 (Figure 7.3) shows the spectrum for a single beryllium ion and the coil currents $I_x = +570\,\mathrm{mA}$, $I_y = +670\,\mathrm{mA}$ and $I_z = 770\,\mathrm{mA}$. The reversed magnetic field direction changes the polarisation here. The interpretation has to be done with precaution: This power broadening is related to the transition matrix element. Nevertheless, the frequency-dependent contribution of the impedance mismatch of the rf source must be taken into account.

The relatively large line widths for an $^2S_{1/2} \rightarrow {}^2S_{1/2}$ transition have two underlying reasons: These measurements are performed for simplicity in a continuous mode

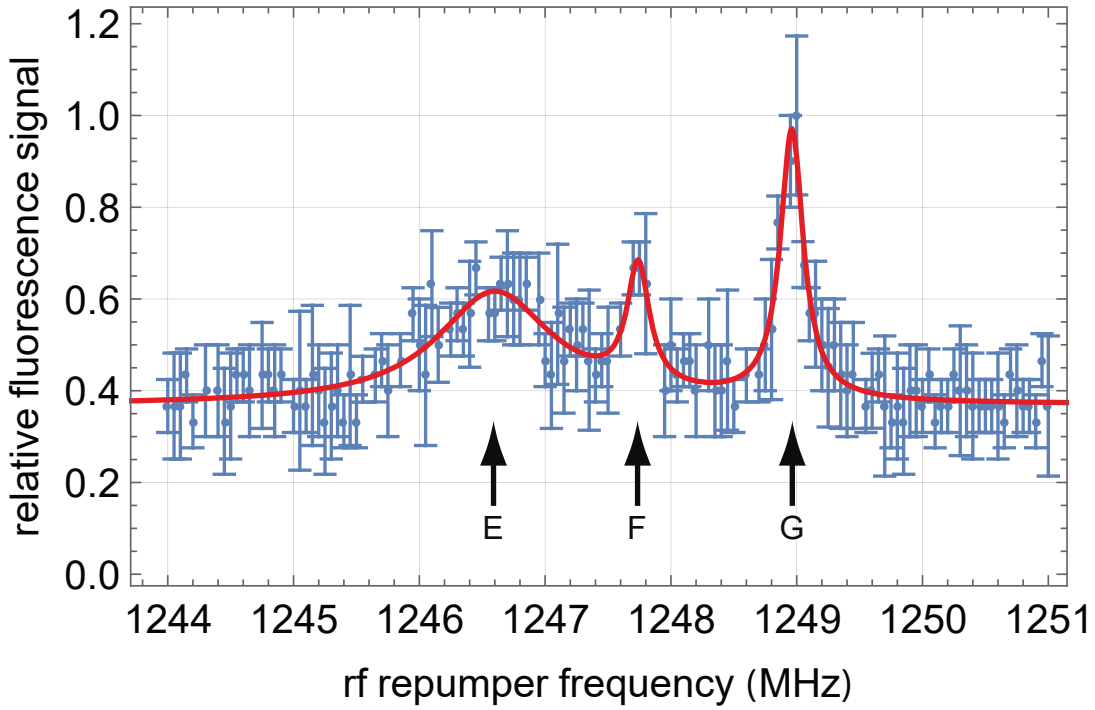

Figure 7.3.: Example 2: M1 transition spectrum for similar coil currents as in Figure 7.1, but with reversed x and y directions in case of a single beryllium ion. The evaluation is shown in Table 7.1.

where the rf frequency is swept in steps while simultaneously the fluorescence is detected (Section 7.2). If the objective is to measure the transition as narrow-band as possible, an interleaved measurement should be performed, as shown in [69]. Since the *Doppler* cooling beam is tightly focused, its power is increased in example 1 so that all four ions are sufficiently illuminated. In this way, line widths $\lesssim 200$ kHz can be achieved for a single ion at an adapted power level.

7.2. Recording the Spectra

Beryllium ions are stored in the trap according to Section 6.2 using scheme C. The coil currents are stabilised by the current source within a few milliamp accuracy, and the UV 3 laser is internally power stabilised. The latter is a slow stabilisation, as power fluctuations are measured with a photodiode and compensated by varying the amplifier power.

The data is recorded script-based. While the data of the PMT is continuously recorded with a time stamp and averaged over half a second, the script is executed as follows:

The rf synthesiser jumps to the start frequency, the time after setting the frequency is recorded in the logbook (timestamped). Afterwards, the frequency is held for a predefined period (usually 1.5 seconds) and then it is noted again in the logbook that the waiting period is over. The rf synthesiser jumps to the next frequency (usual step size 100 kHz) while the next logbook entries are made. This repeats until a final frequency is recorded.

To plot the spectrum, the PMT data is assigned to the frequencies recorded between the two logbook entries for that frequency and averaged again. The steady-state behaviour of the rf antenna can be taken into account by introducing additional waiting times later. However, it turns out that this is not required here. If there is a longer response time, the effect is hidden in the average.

7.3. Measurement of the Applied Magnetic Field Strength

If the frequencies determined from the spectrum are compared with the *Breit-Rabi* formula, the magnetic field strength can be calculated. It is accurate within a few hundred milligauss. In example 1, the centre frequency of line B and C is determined with 6 and 8 kHz precision respectively. The assumption that it is only known by the FWHM is too conservative according to the data. Nevertheless, the difference in the magnetic field strength due to the two lines is a few tens of milligauss and cannot be explained by the fit error.

For better statistics, spectra for different coil currents are evaluated. This also allows the zero field setting for the coils to be determined.

The magnetic field applied to the ion includes an external magnetic field $\boldsymbol{B}^{\text{ext}} = \left(B_x^{\text{ext}}, B_y^{\text{ext}}, B_z^{\text{ext}}\right)^T$ (earth's magnetic field, magnetisation of the experimental setup etc.) superimposed by the magnetic field of the coils $\boldsymbol{B}^{\text{coil}}$ that is a function of the three applied currents I_x, I_y and I_z. The unknown factors $\boldsymbol{k} = \left(k_x, k_y, k_z\right)^T$ for the conversion from current to magnetic field strength, the external magnetic field as well as an offset frequency ν_{offset} must be determined by a multi-branch fit. For this purpose, the data (the three currents and the measured transition frequency ν_{line}) are fitted to the functions

$$f_\xi\left(I_x, I_y, I_z, \nu_{\text{line}}\right) = \xi \cdot 1.4 \frac{\text{MHz}}{\text{G}} \sqrt{\left(k_x I_x + B_x^{\text{ext}}\right)^2 + \left(k_y I_y + B_y^{\text{ext}}\right)^2 + \left(k_z I_z + B_z^{\text{ext}}\right)^2} + \nu_{\text{offset}}$$

and the seven parameters are adjusted simultaneously. The multiplier ξ shall equal $\xi = 0$ for line A, $\xi = \pm\frac{1}{2}$ for lines B and G, $\xi = \pm 1$ for C and F, and $\xi = \pm 1.5$ for lines D and

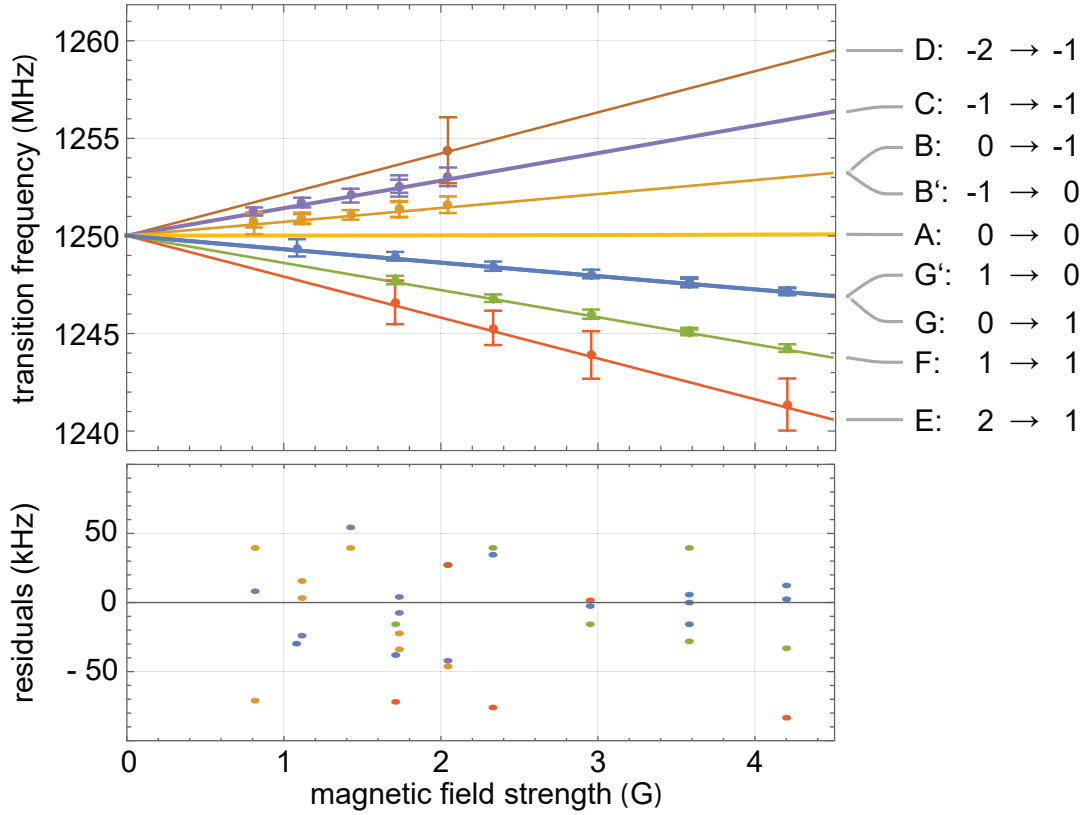

Figure 7.4.: Transition frequencies as a function of magnetic field strength. The data points of the various lines A to G (indicated with projection quantum number for the transition) are assigned to the magnetic field strengths according to the result of the fit (Table 7.2). The error bars correspond to the linewidth from the individual spectra (similar to Figures 7.1 and 7.3 and Table 7.1). The continuous lines correspond to the expected frequencies according to the *Breit-Rabi* formula. The deviation of the measured value from the latter is shown in the figure below.

E [70]. The result of a conservative fit, weighted by the linewidth, is shown in Figure 7.4 and Table 7.2. The apparently nice fit returns parameters with an unexpectedly large standard deviation, although some of the estimates are close to the results of a measurement with a magnetic field sensor ($k_{x,y}^{\text{sensor}} = 2.3\,\text{G/A}$). The latter does not hold for $k_z^{\text{sensor}} = 0.5\,\text{G/A}$.

Although in this model the deviation of the measured frequency from the theoretical value is only a few ten kHz, no trustworthy parameters can be extracted in this way. This method at best gives an indication of the magnitude of the magnetic field strength and seems to be another consequence of the inconsistent frequencies of the lines described earlier.

parameter	estimate	standard error
k_x (G/A)	2.36	16
k_y (G/A)	2.04	17
k_z (G/A)	-3.30	$5 \cdot 10^7$
B_x^{ext} (G)	-0.05	$2 \cdot 10^7$
B_y^{ext} (G)	-0.25	$3 \cdot 10^7$
B_z^{ext} (G)	2.54	$2 \cdot 10^7$
ν_{offset} (MHz)	1250.12	0.14

Table 7.2.: Table of fitted parameters.

7.3.1. Improvement of the Magnetic Field Strength Measurement

The measured transition frequencies between the hyperfine components cannot be assigned to a magnetic field strength without large tolerances. The steps discussed previously (Section 6.8) promise to improve the quality of the data and thus reduce uncertainties in the determination of the centre frequency.

Another aspect is the power supply. The current source for the coils is specified with a typical uncertainty of about ±3 mA. Assuming the model above, this converts into a variation of the magnetic field strength of about ±7 mG. Thus, the expected frequencies fluctuate around 10 kHz, 20 kHz and 30 kHz for lines B and E, C and F, and D and E, respectively.

Since the residuals also fluctuate by some tens of kHz (Figure 7.4), the contribution of the current noise is not negligible.

A frequency-dependent analysis of the magnetic field strength (ac magnetic field noise) could reveal further disturbing influences (for example from the pump or the 50 Hz mains voltage with harmonics, etc.).

7.4. Systematic Effects on the Spectrum

Various systematic effects and their impact on the lines in the beryllium spectrum are considered in this section. Especially with regard to MHI spectroscopy, these must be known in detail.

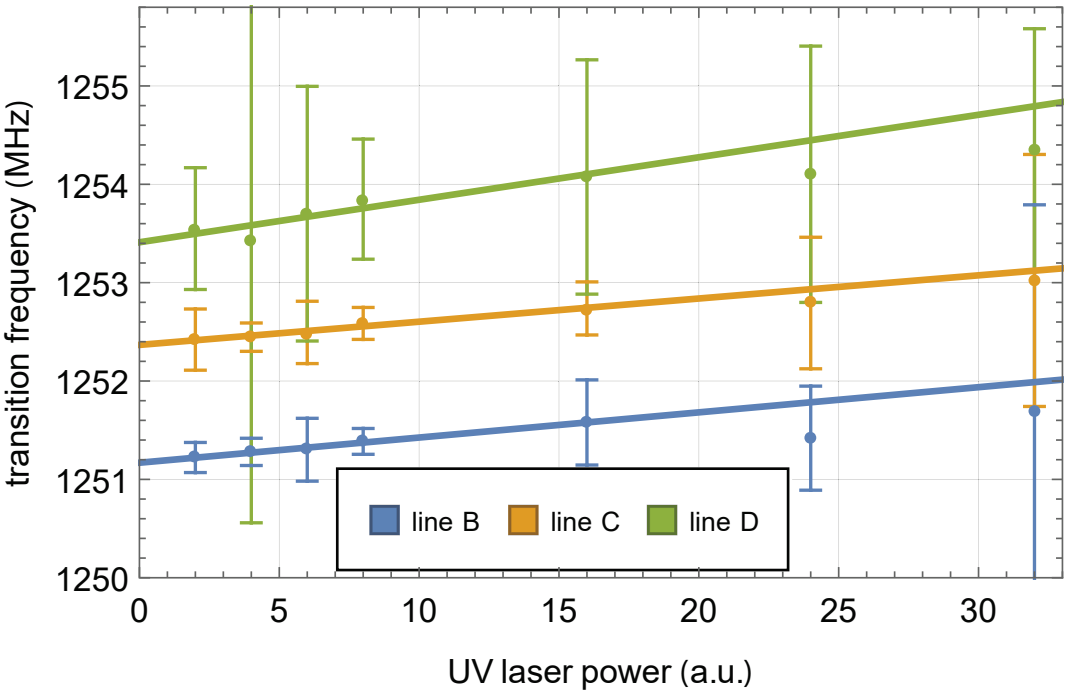

Figure 7.5.: Shift of the transition frequencies as a function of the UV 3 laser power in arbitrary units. The applied currents are $I_x = -1.50\,\mathrm{A}$, $I_y = 1.47\,\mathrm{A}$ and $I_z = 0.72\,\mathrm{A}$.

7.4.1. Frequency Shift due to UV 3 Laser Intensity

A shift in the beryllium transition frequency depending on the irradiated intensities can be observed. Figure 7.5 shows the ac *Stark* shift due to the polarisability of the ion. Each data point is composed of several individual measurements for one power level. For a repeated measurement of the transition frequencies, the spectra show the so far discussed jitter of the transition frequencies (Figure 7.6). In the case of example 3 it results in a mean frequency 1251.39(13) MHz for line B, 1252.59(16) MHz for line C and 1253.8(6) for line D.

A linear fit to the data for the different power levels allows the extrapolation for a measurement with zero power. The result for line B is 1251.169(12) MHz and a *Stark* shift correction of 25.6(1.4) kHz/power(a.u.), for line C it is 1252.367(18) MHz (24(2) kHz/power(a.u.)) and for line D it is 1253.51(8) MHz (27(4) kHz/power(a.u.)).

7.4.2. Effect of the UV 3 and rf Intensity

The influence of the rf and UV 3 powers on the single ion line shape is measured exemplarily for line B, ($I_x = -0.50\,\mathrm{A}$, $I_y = -0.47\,\mathrm{A}$, $I_z = 0.7\,\mathrm{A}$) (Figure 7.7). As a result (Table 7.3), a power broadening for UV 3 is detectable. This is particularly pronounced for 10 a.u. (rf power 31 or 28 dBm) compared to 8 a.u. (31 or 28 dBm). The 25 dBm power

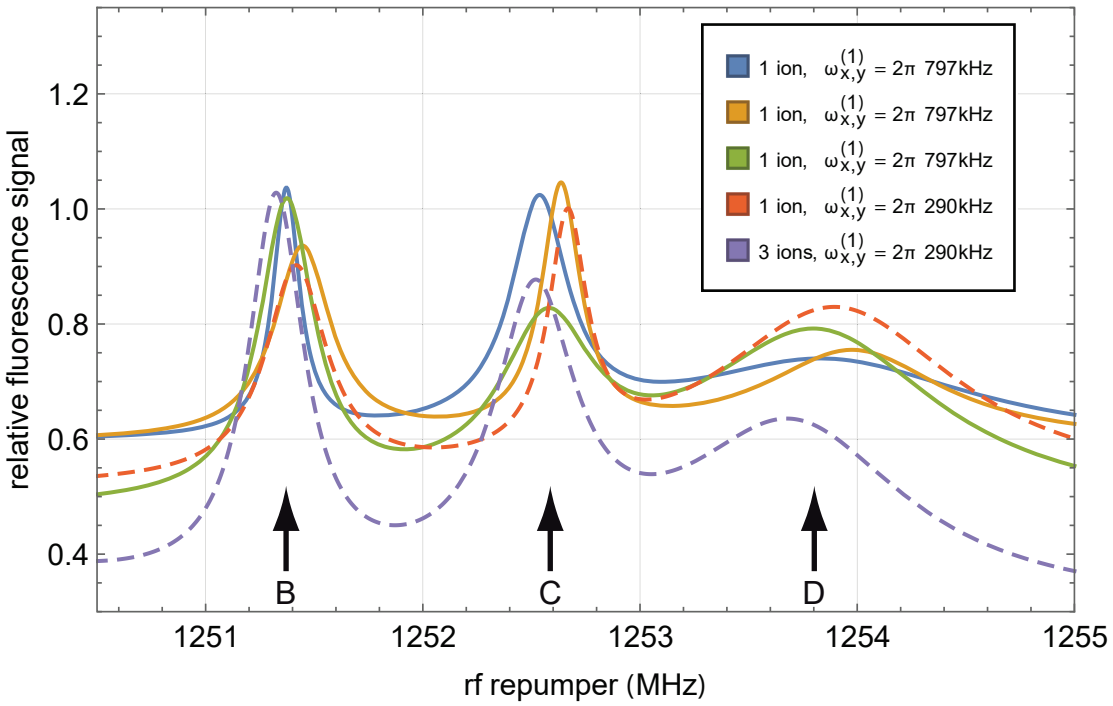

Figure 7.6.: Example 3: Fits to the data (not shown for clarity) taken at a power level of 8 a.u. for two different ion numbers and trap potential depths (coil setting: $I_x = -1.50\,\mathrm{A}$, $I_y = -1.47\,\mathrm{A}$ and $I_z = 0.72\,\mathrm{A}$).

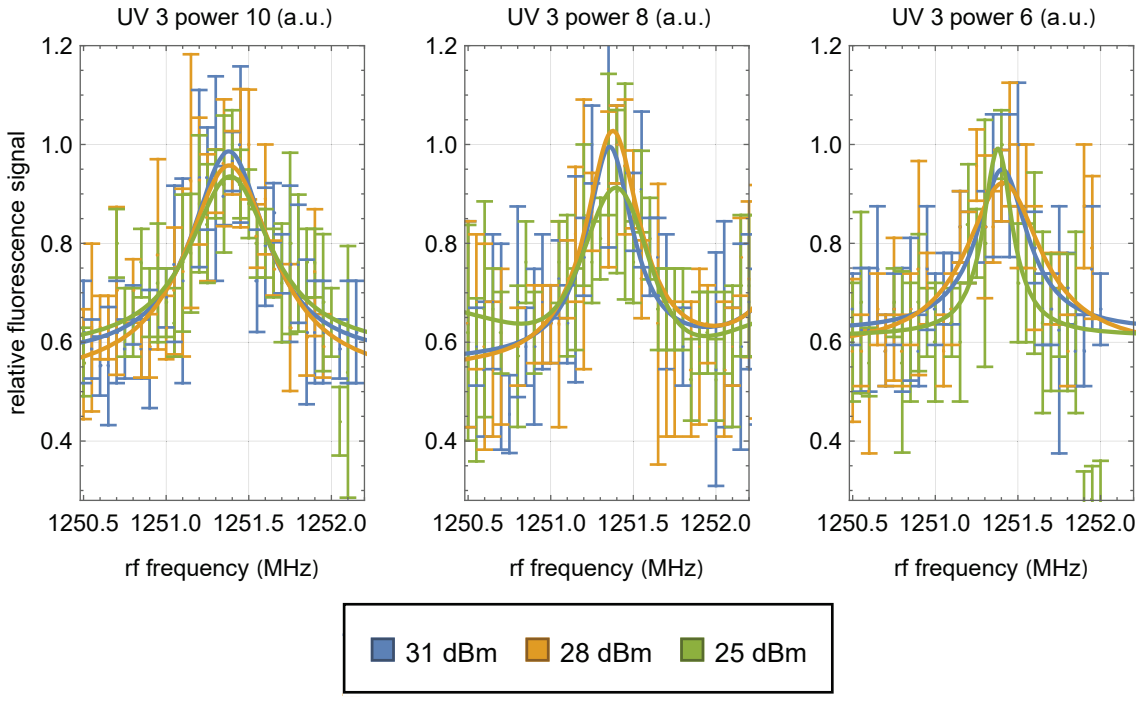

Figure 7.7.: Line shape for three UV 3 power levels and for three rf power levels each. A summary of the analysis is given in Table 7.3.

UV 3 power (a.u.)	rf power (dBm)	frequency (MHz)	linewidth (MHz)
10	31	1251.38(4)	0.55(18)
	28	1251.38(4)	0.55(18)
	25	1251.39(4)	0.61(19)
8	31	1251.375(18)	0.40(7)
	28	1251.36(2)	0.34(7)
	25	1251.39(3)	0.36(11)
6	31	1251.41(4)	0.38(13)
	28	1251.41(6)	0.6(3)
	25	1251.38(3)	0.21(9)

Table 7.3.: Overview of the determined centre frequency and linewidth as a function of the UV 3 and rf power.

has proved to be unsuitable in experiments, as its repumping effect is not sufficiently strong and therefore heating effects are increased. As the UV 3 power increases, the effect of the antenna's signal decreases until UV 3 alone is sufficient to take over the repumping.

On the other hand, recording the rf spectrum for low powers is problematic because the cooling power for a frequency detuned repumper is not sufficient to avoid a phase transition of the ion. In addition, the signal to noise ratio becomes small, so that a fit to the data is increasingly defective. The beginning of the latter can be seen for the power level 6 a.u. A changed line shape due to the rf power cannot be identified here.

A good setting for the analysis of beryllium is 400 nW UV 3 power in front of the vacuum window and an rf power of 28 dBm. Due to the non-optimal impedance matching, 1 part rf power out of 3 is reflected back.

7.4.3. Effect of the Trap Potential

To investigate the influence of the trap potential, lines B and C are analysed (coil current $I_x = -500\,\text{mA}$, $I_y = -470\,\text{mA}$ and $I_z = +0.72\,\text{mA}$) for different trap potentials (Figure 7.8 and Table 7.4).

For the same reason as described above, the centre frequency can only be determined within a few hundred kHz (FWHM). A potential influence of the trap on the transition frequency is not detectable within these limits. An extrapolation of the frequency values for a vanishing trap potential cannot be given here.

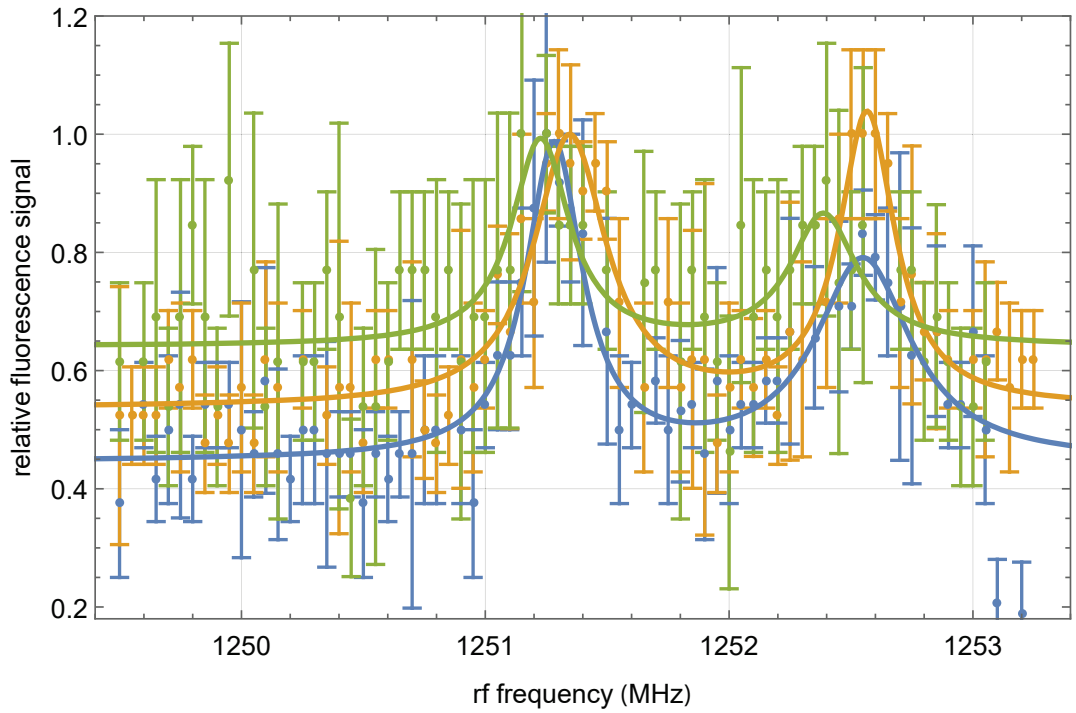

Figure 7.8.: The spectra of lines B and C for 400 nW UV 3 power and 28 dBm rf power for different trap potentials: $\omega^{(1)}_{x,y} = 2\pi\,0.8$ MHz (blue), $\omega^{(1)}_{x,y} = 2\pi\,0.4$ MHz (orange) and $\omega^{(1)}_{x,y} = 2\pi\,0.2$ MHz (green).

trap potential	line B		line C	
$\omega^{(1)}_{x,y}/2\pi$ (MHz)	frequency (MHz)	FWHM (MHz)	frequency (MHz)	FWHM (MHz)
0.8	1251.282(16)	0.28(6)	1252.55(6)	0.48(12)
0.4	1251.347(16)	0.36(6)	1252.566(13)	0.28(5)
0.2	1251.23(3)	0.29(12)	12525.39(6)	0.33(19)

Table 7.4.: Frequency line widths of lines B and C as a function of the trap potential.

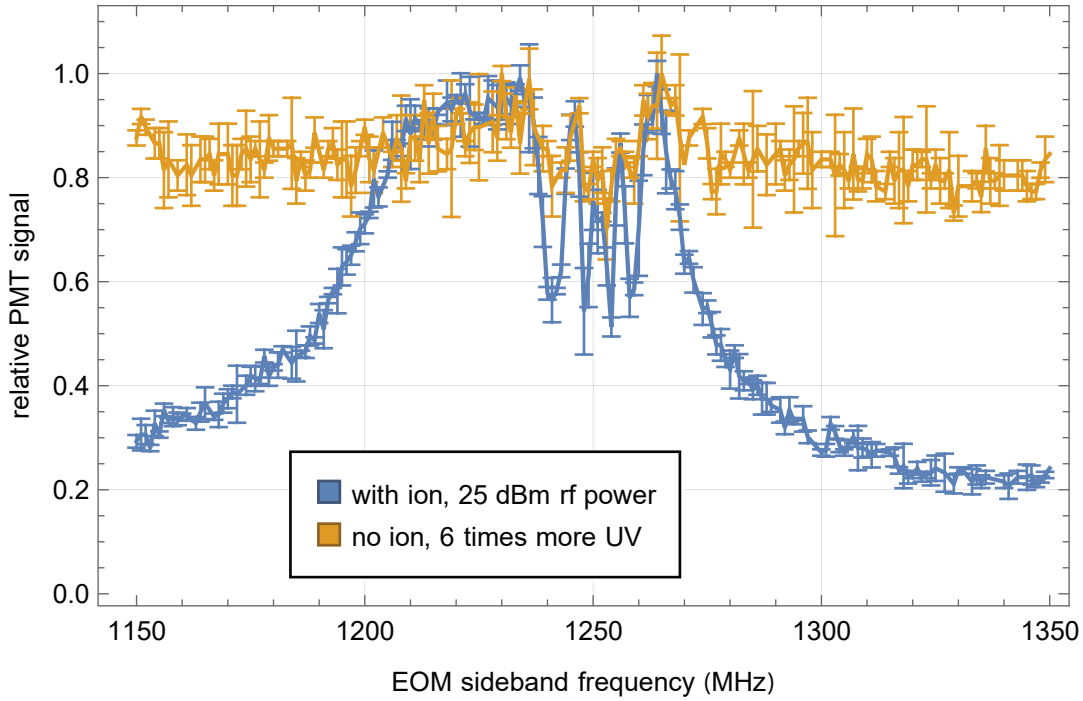

Figure 7.9.: Frequency dependence of the EOM. These characteristic features are detectable in the the scattered light from the trap as well as in the fluorescence of the ion.

7.5. Measurement with the EOM

The EOM, which produces sidebands at 1.25 GHz and is used for scheme B (Section 6.1), has a unfavourable characteristic. Especially at the relevant frequency around 1250 MHz, it shows a strong frequency-dependent effect at the required 25 dBm rf power level (Figure 7.9). This can be observed even in scattered light for 33 µW, i.e. without any stored ion. A fluorescent ion enhances this effect and makes it more obvious.

In order to observe a shift in the transition frequency due to the *Zeeman* effect, the rf power must be reduced to 8 dBm anyhow. Since the relative sideband strength is now too weak, the total UV 3 power must be increased to 11 µW. The spectra recorded in this way for different coil currents are shown in Figure 7.10. Due to the EOM properties shown, the rf antenna is more suitable for measuring the magnetic field strength.

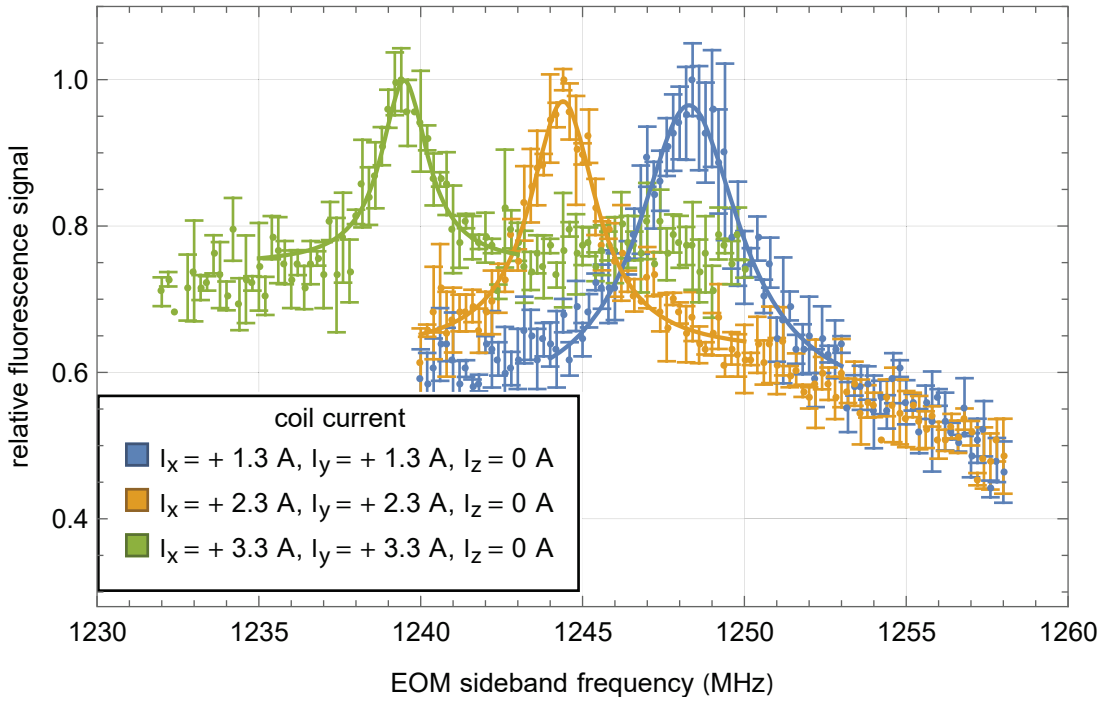

Figure 7.10.: Spectra recorded for different coil currents according to scheme B. It is remarkable that only one component can be detected, which is clearly broadened due to the relatively high power. The frequencies and linewidths are: 1248.29(6) MHz and 3.9(5) MHz (blue), 1244.40(4) MHz and 2.5(3) MHz (orange) and 1239.49(6) MHz and 1.75(19) MHz (green).

8. Studies on MHI

The heteronuclear hydrogen molecular ion HD^+ exhibits dipole-allowed transitions. In contrast to the homonuclear species, it is therefore easier to study experimentally. Representative for the MHI, general techniques and results for HD^+ are discussed in order to apply them later to the homonuclear MHI. In particular, the remarkably high chemical reactivity of this molecular ion is addressed. The methods developed so far are extended to the two-species case.

All multispecies studies were performed using scheme A (Section 6.1).

8.1. MHI Trapping

Before the MHI is loaded, a single beryllium ion must be stored in the trap. It is needed to detect the successful trapping of an MHI. During the MHI loading process, the beryllium ion is heated by the electron bombardment. The injected neutral gas has a (short-term) negligible influence. To counteract the heating, the UV 3 power is increased to 150 µW. Since the electron gun is a universal ionisation device and thus also ionises the residual gas in the chamber (Section 8.6), the trap potential is reduced to $U_{\mathrm{rf}} = 40\,\mathrm{V}$. This means that heavier ions than beryllium no longer fulfil the stability condition, or are practically no longer trapped.

The electron gun is set to the values given in Table 5.1. As discussed in Section 6.5, the electron gun can destroy the compensation of the trap within a few seconds. Its emission time must be reduced to a minimum. For this purpose, the external magnetic field is left switched on during the heat-up phase and so the electron beam is deflected away from the trap. After 8 seconds, a uniform emission is achieved (Figure 5.12). The magnetic field is switched off so that the beam is directed to the centre of the trap and molecular hydrogen is simultaneously injected at a pressure of 3.8×10^{-10} mbar.

During the loading process, at first the fluorescence decreases, the expansion of the beryllium ion increases and its equilibrium position shifts under the influence of the electron beam. The capture of an ion often shows up in a spike in the fluorescence signal or in a sudden change in the beryllium behaviour, which can be seen in various forms on the camera. The loading process is then terminated immediately, stopping

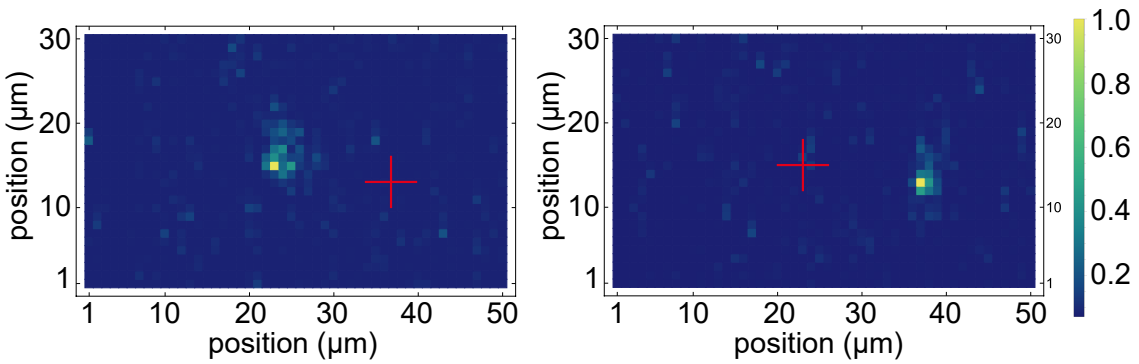

Figure 8.1.: Two equilibrium positions of a beryllium ion after a second species has been added. The red cross marks the other position (Figure 12 of [2], Appendix A). In Section 8.2 it will be proved to be HD^+.

the gas injection and switching off the electron gun. One of the following three cases occurs:

1. Ideally, the added ion crystallises immediately. The beryllium jumps to the equilibrium position for a two-ion crystal. A high dynamic of the ion system can be observed afterwards.

2. If no crystallisation occurs, this indicates the capture of several ions.

3. The loading process fails, either because the beryllium behaviour was misinterpreted and the loading process was wrongly aborted, or because the ion that was initially actually trapped is able to escape.

The following further procedure has proven to be favourable experimentally: Except for case 3, the trap voltage is slowly increased to $U_{\mathrm{rf}} = 70\,\mathrm{V}$ to ensure a better confinement of the ions. For case 1, the rate at which the ions change places slows down until it comes to a stop. In the Figure 8.1, two new equilibrium positions of beryllium are juxtaposed. The cross marks the respective other equilibrium position where an unknown ion species is located. The positions correspond to those of a two ion string. There are no other ions trapped whose position are not temporarily occupied by the beryllium.

The same applies to case 2, whereby the crystallisation process can be observed for a two-ion system when the voltage is increased. If required, the UV 3 power must be increased by a factor of 10 for this purpose. If no crystallisation occurs despite all this, more than one ion has been added. The procedure described in Section 6.2 for beryllium can now be used to remove excess ions. If the trap voltage is lowered to $U_{\mathrm{rf}} = 27\,\mathrm{V}$, the string rotates 90° with respect to the trap axis, resulting in an ion loss. Alternatively, an attempt can be made to remove excess ions by secular excitation. For this, a radial

mode frequency	HD^+			$^9Be^+$			mode type
$\omega^{(p)}/(2\pi)$ (kHz)	$b_x^{'(p)}$	$b_y^{'(p)}$	$b_z^{'(p)}$	$b_x^{'(p)}$	$b_y^{'(p)}$	$b_z^{'(p)}$	
1860.17	0.9999	0.0000	0.0000	0.0119	0.0000	0.0000	$\omega_x^{(1)}$ IP
1699.74	0.0000	0.9999	0.0000	0.0000	0.0143	0.0000	$\omega_y^{(1)}$ IP
599.93	0.0119	0.0000	0.0000	-0.9999	0.0000	0.0000	$\omega_x^{(2)}$ OP
543.71	0.0000	-0.0143	0.0000	0.0000	0.9999	0.0000	$\omega_y^{(2)}$ OP
532.57	0.0000	0.0000	0.9365	0.0000	0.0000	-0.3507	$\omega_z^{(2)}$ OP
240.93	0.0000	0.0000	0.3507	0.0000	0.0000	0.9365	$\omega_z^{(1)}$ IP
617.90±0.70		-		1	0	0	$\omega_x^{(1)}$
563.56±0.28		-		0	1	0	$\omega_y^{(1)}$
207.11±2.98		-		0	0	1	$\omega_z^{(1)}$

Table 8.1.: Measured (lower part for a single beryllium ion) and calculated (upper part for the Be^+ - HD^+ system) frequencies of the normal modes. The components of the eigenvector are mass-weighted, indicated by the dash. IP (OP) denotes an in-phase (out-of-phase) oscillation (Table 1 of [2], Appendix A).

frequency sweep of 1 to 5 MHz with a high amplitude is applied. As can be seen in Table 8.1, this leads to high oscillation amplitudes for the light ion species at $\omega_{x,y}^{(1)}$, while those for beryllium are 49-fold and 40-fold smaller, respectively.

8.2. MHI Detection

After the MHI loading process is completed, the added species must be identified. For the method presented here, the secular frequencies $\omega_u^{(1)}$ of a single beryllium must be known, which allows the frequencies for an HD^+ - Be^+ ion system to be calculated. In general, the frequencies for ion systems with different masses are calculated and compared with the experimentally determined ones.

A list of the measured beryllium frequencies (lower part) and the expected ones for a system of Be^+ and HD^+ (upper part) is shown in Table 8.1.

The secular scan for the single beryllium ion and for the ion system is shown in Figure 8.2. Here, the measured resonance frequency is $\omega_{\text{Be-Ion},z}^{(1)} = 241.2(3)$ kHz and clearly shifted from that of a single beryllium ion. It corresponds to that of a Be^+ - HD^+ system. Thus, the second ion species shown in Figure 8.1 is proofed to be HD^+.

During the axial excitation, both ions change places with each other three times. This can be seen from the fact that the two different beryllium positions fluoresce with

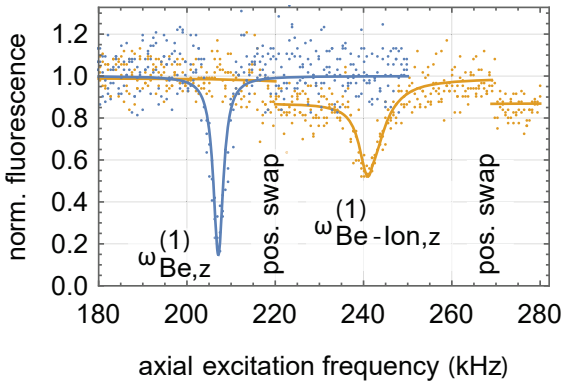

Figure 8.2.: Axial secular scan for a single beryllium ion (blue) and for a two ion system of beryllium and an unknown species (orange). During the scan, the ions have changed places twice, as can be seen from the different fluorescence levels (Figure 11 of [2], Appendix A).

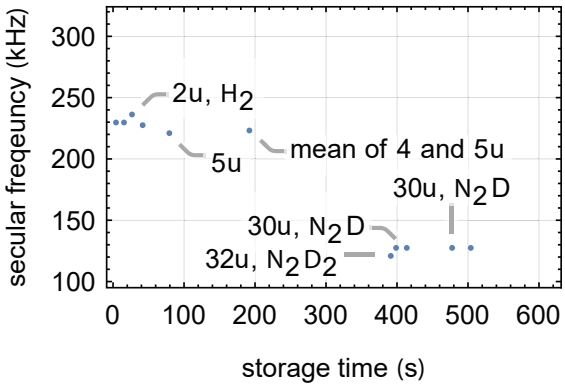

Figure 8.3.: Chemical reactions of a single MHI over time: In the frequency analysis, the measured values are assigned a corresponding theoretical mass and possible corresponding substances. Initially, there is an HD^+ ion trapped. After 25 seconds, the deuteron is replaced by a proton. A nitrogen molecule is trapped later on. The mechanism is explained in the main text.

slightly different intensities, as indicated by the fit. It is assumed that the ions also change places when the resonance condition is fulfilled.

8.3. Chemical Reactions

A special MHI feature is that they have a particularly high reactivity with the residual gas in the chamber. For a continuously performed mass spectroscopy (Section 6.7), a temporal variation of the co-trapped particle mass can be measured (Figure 8.3). As discussed in Section 8.1 the observations of the beryllium ion with the CCD camera initially show high dynamics of the ions. The two ions rapidly exchange their positions and there is repeated heating and recrystallisation of the ion system, which complicates the interpretation of the secular scan. Apart from this, the axial secular frequency

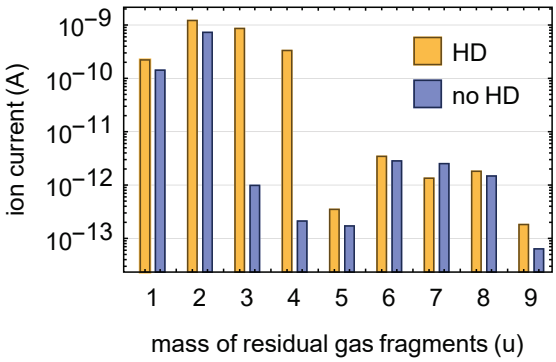

Figure 8.4.: Residual gas analysis for light particle fragments. In addition to HD, D_2 is also present in a relevant quantity in the gas bottle. Here HD was admitted with a pressure of $7 \cdot 10^{-10}$ mbar. The small differences for the other masses are related to a longer outgassing time of the RGA filament between the two measurements.

fluctuates by a few kHz for unknown reasons (Section 6.8.1). Especially for a fast scan over a large frequency range, a mass difference of 1u may be misinterpreted. A compromise must be found between the detectable mass interval and resolution. In the time between time index 200 s to 380 s, no mass is registered because the relevant secular frequency range had to be determined anew. The frequencies found in Figure 8.3, which correspond to an average mass, are insofar the result of two effects: the chemical reaction in progress or an exchange of particles through charge transfer and the fluctuation of the resonance frequency. It turns out that the capture of a heavy nitrogen molecule significantly slows down or stops this dynamic process.

The presence of the species involved in the reaction is shown by the residual gas spectrum (Figure 8.4): there is always hydrogen gas H_2 present with which the ions can react chemically. When HD gas is admitted, a substance with mass 4 u is also injected in a similar amount. Presumably this is D_2. The amount of nitrogen in the chamber, which is also relevant, is not shown in the spectrum. An explanation for this is the repeated flooding of nitrogen during maintenance work.

A kinematic study of ion-neutral collision processes describes the reaction processes [71]: For the homonuclear species it is

$$\begin{aligned} H_2^+ + H_2 &\rightarrow H_3^+ + H \\ D_2^+ + D_2 &\rightarrow D_3^+ + D\,. \end{aligned}$$

For the heteronuclear HD

$$HD^+ + HD \rightarrow \begin{cases} H_2D^+ + D \\ HD_2^+ + H \end{cases} \tag{8.1}$$

there are two possible channels. This explains the presence of masses 2 to 5 u shortly after the neutral gas was injected. The capture of a heavy species usually occurs at a later time, if it has not been ionised directly with the electron gun.

8.4. Concept of State Preparation

Ionisation by electron impact leaves the MHI in a random rovibrational state. Excited vibrational states of the heteronuclear HD^+ molecule decay to the ground state of vibration within a few 10 ms [72]. Rotational transitions in the vibrational ground state $v = 0$ are driven by the blackbody radiation. At room temperature (300 K), the states $L = 1, 2$ and 3 are most likely to be populated [73]. Depending on the chosen spectroscopy scheme, it is possible to wait for the molecule to be occasionally in a certain initial state. Otherwise, the population probability of a desired initial state can be increased through a selective state preparation. The latter is required if a non-destructive spectroscopy is performed.

In the case of homonuclear MHIs, a different approach must be taken because their state does not change after ionisation. Its state preparation will be considered later.

In general, the procedure must be individually adapted to the MHI species and transition that is studied.

8.4.1. HD^+ Molecule

The concept of state preparation for HD^+ to the ground state ($v = 0$, $L = 0$) is shown in Figure 1.2. This is of particular interest for a number of spectroscopy schemes, since the $L = 0$ state has only four hyperfine levels. An instructive candidate for spectroscopy is the transition (0, 0) to (5, 1) with a spectroscopy laser at 1.15 µm (Section 9.2).

If the HD^+ is initially in the first rotational excited state (0, 1), it is excited further to (2, 0) with a laser at 2.7 µm (red arrow). By spontaneous emission it either ends in state (0, 0) or (0, 2) (grey dashed arrows). The second excited state $L = 2$ is depleted with the QCL through (1, 1) from where it can spontaneously decay to the ground state (purple and grey dashed arrow). The comparatively short-lived states $L \geq 3$ are not considered in this scheme.

A successful population of the ground state (0, 0) can be verified with an optical dipole force (ODF, Section 9.1). Afterwards the state preperation can be terminated. The ion system will be heated by the ODF and must be therefore *Doppler* and/or sideband cooled again. When the state of the ion is initialised, the spectroscopy can be carried out. If this is done with a non-destructive state detection method, the initial state must be restored in the same way before the next run.

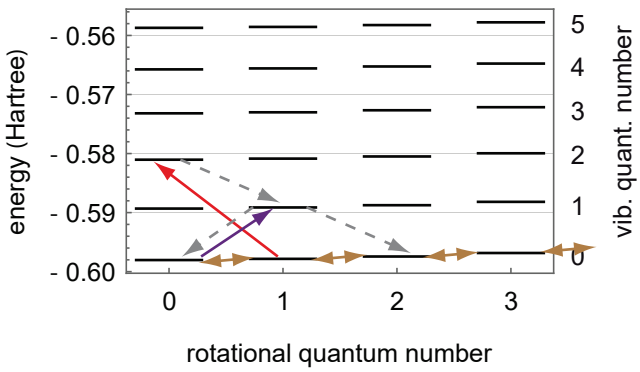

Figure 8.5.: State preparation of $(0, 2)$: States $(0, L \geq 3)$ are ignored. The state $L = 1$ is depopulated with 2.7 µm radiation (red) and $(0, 0)$ by a 5.12 µm QCL (purple). In the vibrational ground state, the rotation levels are coupled by the blackbody radiation (brown). Energies are from [30, 31].

The preparation to the another initial state (0,2) occurs again by the transition (0,1) to (2,0) (red arrow) and (0,0) to (1,1) at 5.12 µm (Figure 8.5). Other states can be prepared in a similar way.

8.4.2. State Distillation of H_2^+ and D_2^+

Instead of HD, the gases H_2 and D_2 can also be injected into the chamber and ionised with the electron gun. The electron impact causes this ion to be in a random rovibrational state, which does not spontaneously decay to the ground state as in the HD case, since all transitions are almost completely dipole forbidden. This also presents a special challenge to the spectroscopy lasers in terms of performance, because only electric quadrupole (E2) or other weak transitions are allowed. Therefore, the desired initial state must be established in another way.

The concept is to load an ensemble of several MHIs so that one is randomly in the required initial state. This one ion is now to be filtered out by dissociating all other ions. This process is called state distillation.

For these two homonuclear species, the ground state $(0, 0)$ is again of particular interest for spectroscopy. By absorbing one or two photons, the ion is excited from the ground state $(0, L > 0)$ into a corresponding vibrational state $v \geq 1$ from which it can be dissociated with the 235 nm BePhI radiation. From this level, the MHI can be dissociated by the 235 nm-BePhI radiation. As shown in Figure 3.4, these wavelengths are in the range of 2.35 to 2.38 µm for H_2^+ and between 3.24 and 3.26 µm for D_2^+. The Topo laser can target these wavelengths.

In principle, there is also a small dissociation cross section for the states $v = 1$ with BePhI. However, it might be too small. To speed up the dissociation process, the ions

can be excited to state $v' = 3$ with the Topo (Section 3). This type of state distillation can be further simplified by half of the transitions, if a nuclear spin-prepared (para- or ortho) H_2 or D_2 gas is used from the beginning.

The method still needs to be tested experimentally. For this purpose, procedures must be developed with which the Topo can quickly and precisely reach the required wavelengths. In addition, the number of MHIs to be trapped must be determined so that an ion is present in the desired initial state. The irradiation durations and powers for the state distillation must also be determined.

In principle, the hydrogen ion can be transferred to the ground state by buffer gas cooling with neutral helium. The procedure is described in [74] and the references therein. However, chemical reactions are possible with the additionally admitted gas, which must be avoided, as already discussed in Section 8.3.

By avoiding the electron impact ionisation, the H_2^+ ion can also be produced in a selected state by a 3+1 resonance-enhanced multiphoton ionization (REMPI) of the neutral molecule [75].

8.5. Spectroscopy of a Single Ultracold MHI

For demonstration purposes of a single ultracold HD^+ molecule spectroscopy, the transition (0, 1) to (4, 0) has been chosen. This is a very simple spectroscopy scheme with a total of only three laser sources: the *Doppler* cooling laser, the spectroscopy laser and the laser for photodissociation. Therefore it is very robust against errors. On the one hand, the initial state $L = 1$ is relatively frequently populated, so that a state preparation can be omitted here. On the other hand, the final state $L = 0$ has the simplest hyperfine structure splitting. The artificially broadened spectroscopy laser (Section 5.6, *Laser for Spectroscopy*) can thus robustly drive the transition (Figure 8.6). For the sake of simplicity, the destructive state detection of HD^+ by means of photodissociation from $v = 4$ is used here. If the spectroscopy laser is detuned by +10 GHz from the transition frequency, the HD^+ cannot be excited to the vibrational level from which it can be dissociated.

The photodissociation laser electronically excites the HD^+ molecule from the binding $1s\sigma$ state into the anti-binding $2p\sigma$ state with an theoretical cross-section $8.5 \times 10^{-18}\,\mathrm{cm}^2$ [76]. Here, the molecular system reaches an energy minimum for large distances between nuclei. It breaks apart through two different decay channels:

$$HD^+ (v = 4) + \hbar\omega_{266} \rightarrow \begin{cases} H(1s) + D^+ \\ D(1s) + H^+ \end{cases}$$

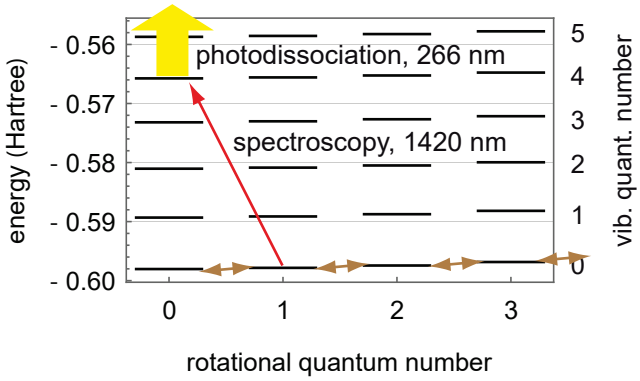

Figure 8.6.: HD^+ spectroscopy: The spectroscopy laser (red, 1420 nm) excites the ion, which is occasionally in the initial state (0, 1), to (4, 0), from where it can be dissociated by 266 nm UV radiation (blue). Energies by [30, 31].

In the process, the remaining ion can only occasionally leave the trap, which leads to a sudden jump of the beryllium to the new equilibrium position. Presumably, the remaining ion reacts quickly with the residual gas or a charge exchange occurs. This assumption is supported by the observation of low secular frequencies. Basically, a laser-induced photodissociation event cannot be distinguished from a chemical reaction described in Section 8.3 without UV laser. This requires a statistical evaluation of many events. Anyhow, the time scale on which the chemical reactions occur without photodissociation seems to be slower.

The time sequence of the individual steps for the spectroscopy of a single HD^+ is shown schematically in Figure 8.7. A single beryllium ion is stored as described in Section 6.2 (in deviation, a *Doppler* cooling power of 60 µW is used). Then a single HD^+ is added according to the procedure in Section 8.1. In order to perform the spectroscopy always under the same conditions, the UV 3 power is increased to 450 µW. This power boost leads to a crystallisation. Otherwise, the ion must be reloaded. An initial fast axial secular scan (6 seconds, 100 kHz span) confirms the presence of HD^+ followed by ten seconds of spectroscopy laser irradiation and simultaneous photodissociation. A second fast axial secular scan probes the resonance frequency of the Be^+ - MHI system. If it is not present, the run is registered as a successful excitation. By selecting the scan range, the reactions of type Equation 8.1 can be identified. A second irradiation with the spectroscopy laser and the photodissociation laser follows - this time for 20 seconds, followed by another check of the resonance frequency. Finally, a run for 30 seconds and the last test are performed.

If the latter shows that it is still HD^+, the blackbody radiation does not seem to populate the required initial state in a sufficiently short time to be able to exclude chemical reactions with the residual gas. Therefore, the ion is removed from the trap by a strong

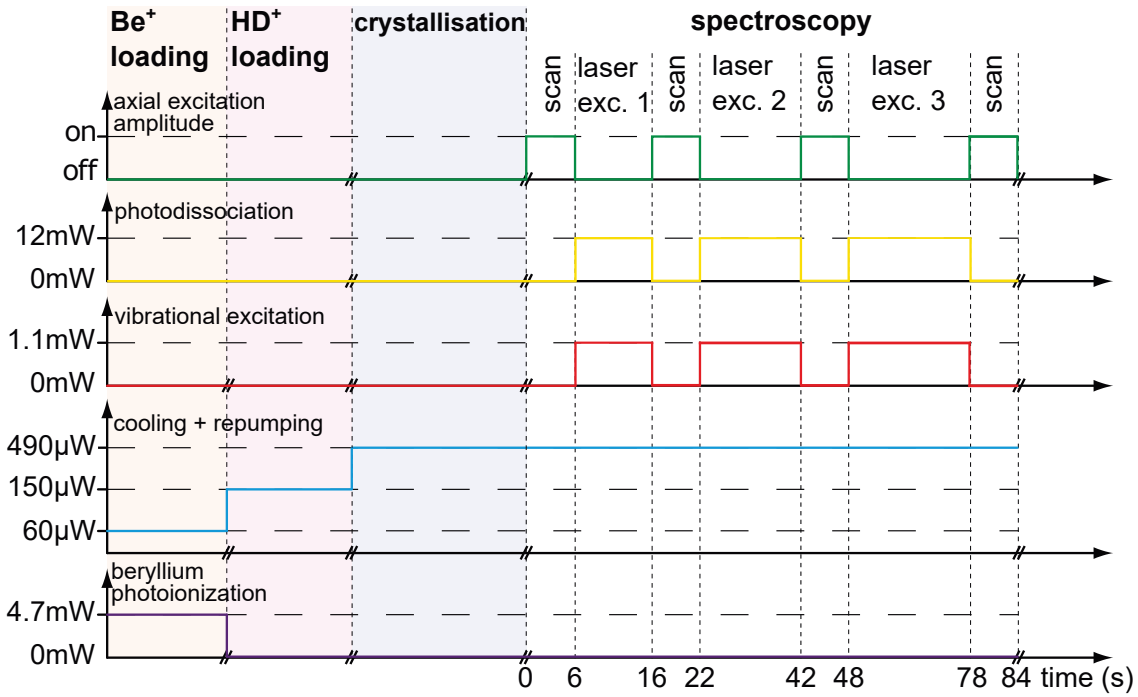

Figure 8.7.: Time sequence of a spectroscopic run (Figure 14 of [2], Appendix A). Details in the main text.

radial secular excitation at $\omega_x^{(1)}$ and a new HD^+ ion is loaded. A complete run including ion preparation takes about 2 minutes.

Figure 8.8 shows the continuous fluorescence signal during a run. After 10 seconds of spectroscopy time (laser exc. 1), the first secular scan is started (start trigger: continuous orange line). The scan range is chosen ±50 kHz around the $\omega_z^{(1)}$ resonance frequency, so that after half the scan time (3 seconds) the HD^+ signal is expected (trigger signal, dashed orange line). By centring the frequency range around the expected value, it is possible to quickly assess whether HD^+ is still trapped. Towards the end of the second laser excitation (laser exc. 2), two dips in the signal occur in quick succession. The beryllium shows a high dynamic here, which indicates dissociation. It is likely that this is a dissociation event followed by the capture of a heavy particle. The second scan confirms this, as the resonance frequency has shifted by more than 50 kHz. During the last excitation phase (laser exc. 3), as expected, no change in the signal can be recognised.

In this way, 27 MHIs have been studied. Of these, 18 where the spectroscopy laser was set to the transition frequency and 9 where it was +10 GHz out of tune. In the first case, 5 dissociation events could be detected during the first ten-second excitation, four more during the second 20-second phase and again 4 during the 30-second phase. In contrast, for the detuned case, no dissociation could be detected during the first and second phases. Only one event was detected in the last phase. Since an MHI has been

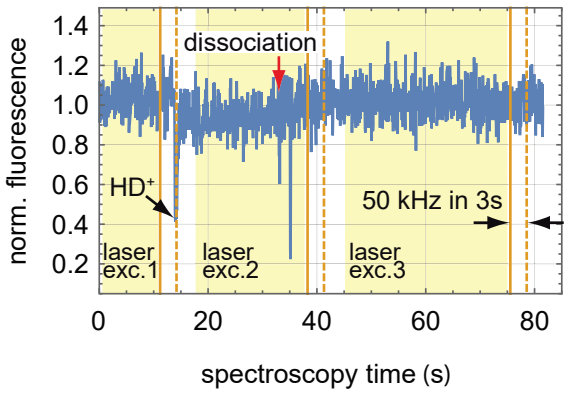

Figure 8.8.: Continuous fluorescence signal during a spectroscopy run. The three time slots of laser excitation are shown (yellow areas). The secular scan is started at the times marked with a continuous orange line. After half the scan period (dashed orange line), the resonance frequency of the Be^+ - HD^+ system is reached.

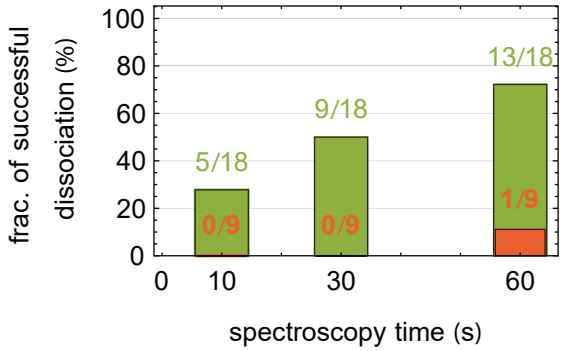

Figure 8.9.: Summary of the HD^+ excitation. The dissociation events are added up and plotted as a fraction against the total irradiation time. Green for the spectroscopy laser set to resonance and red for a +10 GHz detuning (Figure 15 of [2], Appendix A).

used here for several runs and thus for a relatively long time, it is probably a chemical reaction that cannot be assigned to the interaction with the lasers.

These results are summarised in Figure 8.9. The ion loss under resonance conditions is significant.

This spectroscopy finally demonstrates the overall functionality of the system.

8.6. Other Ion Species

In principle, gases of any kind can be injected into the chamber through the leak valve and ionised with the electron gun. As long as they fulfil the stability condition for the *Paul* trap, they can also be stored. In the case of a nitrogen-beryllium ion pair, the residual gas in the vacuum chamber can be ionised and stored without an additional

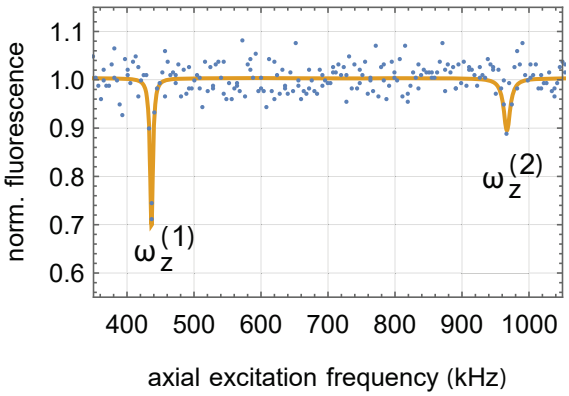

Figure 8.10.: Axial frequency spectrum identified as a system Be^+ - N_2^+ for $\omega_{\mathrm{Be},z}^{(1)} \approx 2\pi \cdot 652\,\mathrm{kHz}$ (Figure 16 of [2], Appendix A).

gas feeding if the trap potential is not lowered (Section 8.1). Otherwise, the procedure is identical to the loading of an MHI. This means that even if neutral molecular hydrogen is added without lowering the potential, nitrogen will always be trapped.

The variation in the stored particle mass over time shown for the MHI case (Section 8.3) can also be observed for other ions, as shown below.

8.6.1. Charge Exchange

During the experiment, there is often an exchange of charge between the stored particles and those present in the residual gas (Figure 8.3). The axial COM mode frequency decreases by this process and the unknown species can be identified. For example, a spectrum with the axial mode frequencies $\omega_z^{(1)} \approx 2\pi \cdot 436.7\,\mathrm{kHz}$ and $\omega_z^{(2)} \approx 2\pi \cdot 967.1\,\mathrm{kHz}$ (Figure 8.10, $\omega_{\text{Be-Be},z}^{(1)} \approx 2\pi \cdot 652\,\mathrm{kHz}$) can be identified as reactions of charged beryllium ions with the residual gas of type $Be^+ + N_2 \rightarrow Be + N_2^+$. The two calculated values $\omega_z^{(1)} \approx 2\pi \cdot 431.5\,\mathrm{kHz}$ and $\omega_z^{(2)} \approx 2\pi \cdot 986.9\,\mathrm{kHz}$ show a few ten kHz deviation from the measured frequency, which has been discussed in detail in another context (Section 7). Conversely, for species lighter than beryllium, the frequency would increase. If only smaller frequencies ($<\omega_{\mathrm{Be},z}$) are scanned, the Be^+ - HD^+ system under investigation remains unaffected by the detection method (Section 6.3).

9. Non-Destructive Detection of the MHI State

In all previous HD^+ spectroscopy experiments, the state has been detected in a destructive way. Since a single ion is studied, a new one must be loaded after each successful excitation, which is demonstrated by the destruction of the molecule. In this regard, non-destructive state detection is desirable.

There are various methods that can be used to detect the rotational and vibrational state of the MHI even without destroying the ion. However, the proposals based on quantum logic ([23, 22]) require a sophisticated experiment. For example, the ion system must be prepared in the ground state of the motional mode $\omega_z^{(1)}$ using *Raman* sideband cooling (within this work, a corresponding laser system has been set up) as the cooling method to achieve a small *Lamb-Dicke* parameter. If the molecule is excited during the spectroscopic run, this event is mapped to the excitation of mode $\omega_z^{(1)}$, which in turn must be detected.

These methods can be implemented in the future if necessary. First, the non-destructive HD^+ state detection by means of an optical dipole force should be considered.

9.1. Detection by an Optical Dipole Force

Another method for HD^+ with less stringent requirements is based on an idea for atoms [77] and has been extended to molecules [25]. Here, a running standing wave is used whose optical frequency is non-resonantly coupling two molecular states. If the molecule is in one of the two states, the standing wave causes an optical dipole force (ODF) that excites the mode $\omega_z^{(1)}$ (Section 2.2), whereby the rovibrational molecular state is not changed (non-destructive detection).

In contrast to the methods based on quantum logic, the ion pair does not necessarily have to be in the ground state of mode $\omega_z^{(1)}$. If the laser used to generate the ODF has a sufficiently high intensity, this still leads to an enlarging of the ion's extend that can be

identified on a CCD camera. The idea has been demonstrated as feasible on an atomic system [26].

In the following, two relevant transitions are analysed with regard to the ODF using a Wolfram Mathematica script [78]. These always include a state with $L = 0$. However, since the Topo has a large tuning range, transitions $(\nu, L \neq 0)$ to $\left(\nu', L' \neq 0\right)$, can also be taken into account for spectroscopy. The evaluation of the ODF is based on an extension of [79] and a publication from the Willitsch group at the University of Basel for the N_2^+ molecule ion [80].

The two counter-propagating beams of the Topo (Figure 5.16) create a running standing wave with an intensity pattern that corresponds to half of the wavelength. In order to excite the axial oscillation, the two beams must have a frequency difference $\Delta\omega = \omega_z^{(1)}$, which leads to a time-dependent force acting on the ion. For this purpose, the beam at freqeuncy ω is split and the two branches are $\pm\omega_z^{(1)}/2$ frequency-shifted with one AOM each. It is assumed that the waists w_0 of both beams overlap in the centre of the trap. Even with the strong focussing of the beams assumed in the following, the *Rayleigh* length $z_R = \pi w_0^2/\lambda > 2\,\mathrm{mm}$ $\left(w_0 > 50\,\mu\mathrm{m}\right)$ holds, so that plane wave fronts can be expected at the ions' locations.

As a consequence, the axial

$$E_{\mathrm{ax},\pm}\left(z, t; \omega, \Delta\omega, \Delta\phi, \alpha\right) = E_0 \exp\left[i\left(\pm k_\pm \cos\left[\alpha\right] \cdot z - \left(\omega \pm \Delta\omega/2\right) \cdot t + \Delta\phi\right)\right]$$

and radial

$$E_{\mathrm{rad},\pm}\left(u, t; \omega, \Delta\omega, \Delta\phi, \alpha\right) = E_0 \exp\left[i\left(\mp k_\pm \sin\left[\alpha\right] \cdot u - \left(\omega \pm \Delta\omega/2\right) \cdot t + \Delta\phi\right)\right]$$

electrical field components are given as a function of $k_\pm = \frac{\omega \pm \Delta\omega/2}{c}$, the peak intensity $I = \frac{2p_0}{\pi w_0^2}$ depended electrical field strength $E_0 \equiv E_\pm = \sqrt{2\mu_0 c I}$ and the incidence angle α. To simplify matters, an identical waist and power p_0 is assumed for both beams.

This gives the spatial and temporal intensity distribution

$$I_{\mathrm{ODF}} = 2I\left(1 + \cos\left[\left(2k_+ - \Delta\omega/c\right)\left(\cos\left[\alpha\right] \cdot z - \sin\left[\alpha\right] \cdot u\right) - \Delta\omega \cdot t + \Delta\phi\right]\right)$$

of the two beams that leads to an ac-*Stark* shift of the molecular states.

The optical dipole force is a radiation force associated with the gradient of an energy U,

$$\boldsymbol{F}_{\mathrm{ODF}} = -\nabla U\,,$$

here caused by the *Stark* effect (in Joules). It is given for the state i by

$$\Delta E_{\mathrm{ac}}^{(i)} = \frac{I_{\mathrm{ODF}}}{2\varepsilon_0 \hbar c} \sum_j \sigma_j^{(i)} \frac{\left|\langle j|\boldsymbol{\mu}|i\rangle\right|^2}{\Delta_j^{(i)}},$$

with the transition dipole matrix element $\langle j|\boldsymbol{\mu}|i\rangle$, $\sigma_j^{(i)} = \pm 1$ for $E^{(i)} \lessgtr E^{(j)}$ and the laser detuning $\Delta_j^{(i)} = \omega - \omega_j^{(i)}$ to the transition frequency [80].

In order to calculate the transition matrix element for the various HD^+ cases, the reduced dipole transition moments $\langle iL_i \| d^{(1)} \| fL_f \rangle$ required for this are computed from the oscillator strengths $f_{i\to f}^{(1)}$ given in [81] and the relationship

$$f_{i\to f}^{(1)} = \frac{2}{3}\left(E_i - E_f\right) \frac{\left|\langle iL_i \| d^{(1)} \| fL_f \rangle\right|^2}{2L_i + 1}$$

from [82].

9.1.1. ODF for $(v = 0, L = 0) \leftrightarrow (v' = 2, L' = 1)$

As an example, the ODF is analysed for the ground state ($v = 0,\ L = 0$) and state (2, 1), which should be implementable with the Topo that is detuned by 2 GHz from resonance. The population of the ground state has to be specifically probed later (Section 9.2).

Depending on the intensity of the counter-propagating laser beams I at 2.65 µm, an axial ODF, $F_{\mathrm{ODF},z} = -\frac{\partial \Delta E_{\mathrm{ac}}^{(i)}}{\partial z}$, for ions on the trap axis ($u = 0$) of several 10 yocto-newtons $\left(10^{-24}\,\mathrm{N}\right)$ can be expected [78]. It is assumed that $\omega \gg \Delta\omega$ holds and that the detuning $\Delta_j^{(i)}$ is large for all other transitions except the one under consideration. This drives the ion oscillation and leads to an increasing spatial expansion of the ions along the trap axis. As can be seen in Figure 9.1, a previously resting beryllium ion driven by the ODF oscillates after about 11 ms with the maximum displacement of 5 µm (the case shown here is analogous to Figure 2.3).

For a single ODF beam power of 300 mW (focused to 100 µm diameter), "heating" rates of about $10\,\hbar\omega_z^{(1)}$/ms are obtained for the Be^+ ion (Figure 9.1), which is higher than the background heating rate. Forced axial secular oscillations on a CCD camera can be seen in Figure 6.2a and b. As can be seen in Figure 9.1, half of the kinetic energy is obtained after 5.2 ms ODF interaction time, which corresponds to a beryllium ion spread of 3.4 µm. According to Section 6.4, this is equivalent to imaging the ion with six pixels instead of one.

As a result, a camera with a frame rate of 120 Hz is sufficient to capture the effect of the ODF.

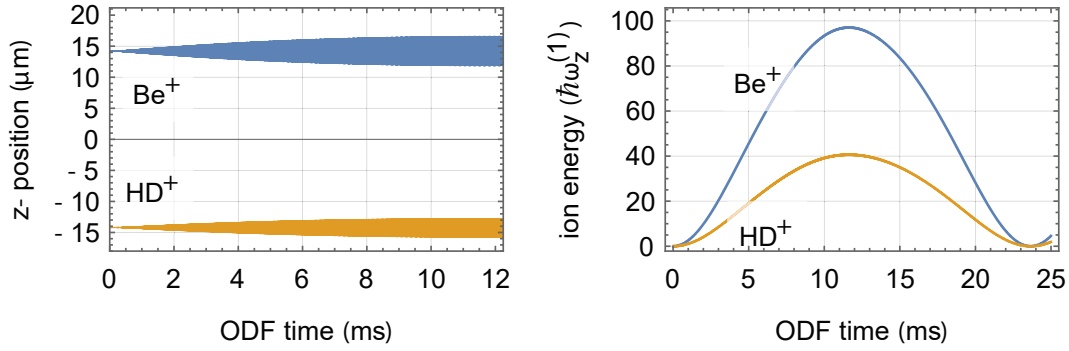

Figure 9.1.: Ion positions (left) and energies (right) as a function of ODF time in a typical trap potential. Each beam's power is 300 mW. The elongation of the ions increases continuously during the first 11 ms (left). The energy evolution of the ions in mode $\omega_z^{(1)}$ as a function of time is shown to the right. Half of the maximum energy is reached after 5.2 ms.

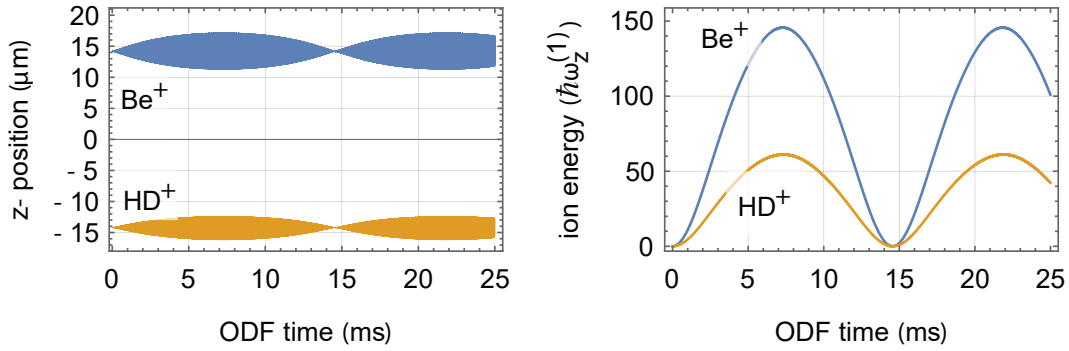

Figure 9.2.: Ion positions (left) and energies (right) as a function of ODF exposure time for transition $(v = 3, L = 0) \rightarrow (v' = 5, L' = 1)$.

9.1.2. ODF for $(v = 3, L = 0) \leftrightarrow (v' = 5, L' = 1)$

For the second transition considered in section 9.2, $(v = 3, L = 0) \leftrightarrow (v' = 5, L' = 1)$ at 3.11 µm, the ODF is larger (about 200 yocto-newtons) because the transition-line strength is stronger here. Consequently, the beam diameter can be increased to 200 µm to obtain a maximum elongation of the Be^+ ion (5 µm) after about 7.3 ms and again after 21.8 ms (Figure 9.2). In this simulation, all other parameters have remained the same for better comparability with the other transition. Now the heating rate is $23\,\hbar\omega_z^{(1)}$/ms. The radiative lifetime of state (5, 1) is 16 ms [72], so a high-speed camera is required for detection.

With a frame rate of 120 Hz, it should be possible to capture the excitation of the oscillation even allowing for minor synchronisation problems. If necessary, the experimental parameters can be slightly adjusted to optimise the detection. In principle, a magnification triplet (factor 7) belonging to the lens system used can be implemented in order to be able to detect the oscillation in a better way.

9.2. Radiofrequency Spectroscopy of HD^+

Radiofrequency state manipulation of HD^+ is an important tool and should be performed in combination with the ODF detection to validate the status of the state preparation process.

For spectroscopy on a single MHI, this means that a preparation to the ground state ($v = 0$, $L = 0$) is of special interest since it has a relatively simple hyperfine structure. Its maximum spacing is about 1008.3 MHz at zero magnetic field strength [55]. Assuming a magnetic field perfectly compensated to zero Gauss, the four hyperfine states can be coupled by simultaneously applying three rf frequencies (Figure 9.3). The initial state is randomly populated at some point in time. In this way, a continuously irradiating spectroscopy laser can excite the MHI. For a not perfectly compensated magnetic field, the rf frequencies can be scanned. Because of the absence of a magnetic field, a pure polarisation of the cooling laser cannot be achieved. Under these circumstances, the state detection by means of ODF is not possible. For the state detection, the magnetic field must first be switched on and the ion system cooled before the ODF can be applied. For this reason, it could be advantageous to work with an existing magnetic field from the beginning.

Thus, the rf spectroscopy of a single MHI is always associated with a rovibrational transition. Depending on the application, either the radio frequency or the frequency of the excitation laser is kept constant. The procedure is explained using the example of the fourth overtone spectroscopy but can be adapted for other scenarios.

9.2.1. Fourth Overtone Spectroscopy with a Single Ion

The fourth overtone transition $(v = 0, L = 0) \rightarrow (v' = 5, L' = 1)$ at 1.15 µm [Kortunov 2022] has been studied on trap 1. A recoil shift has been found. A complementary measurement at trap 2 could provide an indication of its origin.

Therefore, the ion must be prepared to $(0, 0; F = 1, S = 2, J = 2, m_J = 0)$ or $(0, 0; F = 0, S = 1, J = 1, m_J = 0)$. In this case the degeneracy is lifted by a magnetic field and the transition $m_J = 0$ to $m'_J = 0$ for $(5, 1; F' = 1, S' = 2, J' = 1, m'_J = 0)$ or $(5, 1; F' = 0, S' = 1, J' = 2, m'_J = 0)$ is analysed.

The four (0, 0) hyperfine states split into a total of 12 *Zeeman* components, where each individual one must first be transferred to the initial state (Figure 9.3).

A controlled method is a sequence starting with the detection that the MHI is in the $(0, 0)$ state. Next, the MHI is assumed to be in the initial *Zeeman* component of the ground state (about 8 % probability). The excitation laser is irradiated, followed by a $(0, 0)$ state detection (Section 9.1.1). If the MHI is no longer in the initial state, the

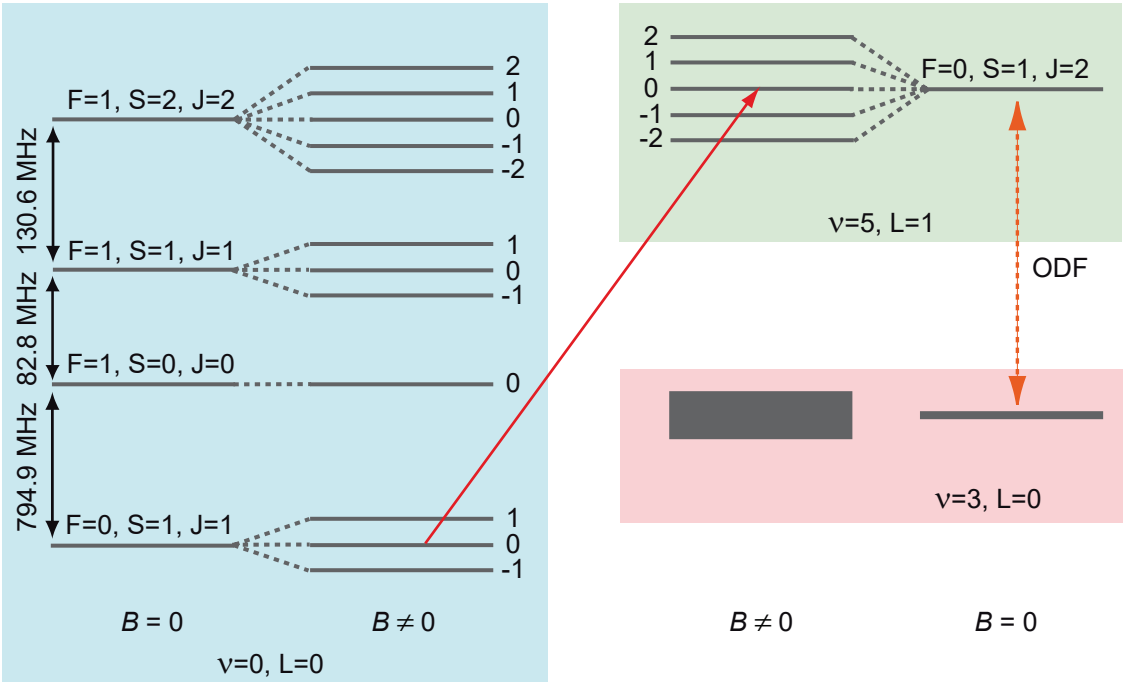

Figure 9.3.: Spectroscopy and detection scheme for the transition $(0,0;0,1,1,0)$ to $(5,1;0,1,2,0)$. A successful excitation with 1.15 µm (red arrow) is proved by an ODF due to the $(v=3, L=0)$ and $(v'=5, L'=1)$ states.

excitation was successful under ideal conditions and the sequence can be aborted. If the ion is still in the initial state, the excitation frequency and timing was not optimally chosen or the ion was in the wrong state from the very beginning.

A series of one or more radiofrequency π-pulses successively transfers the population of the other states to the initial state, always followed by excitation, state detection and cooling phase. It is important that the degeneracy is lifted by applying a magnetic field so that a specific transition can be targeted. On the other hand, the magnetic field strength must be known very precisely in order to predict the resonance frequency and thus enable a complete population transfer by the π-pulse.

Another approach consists in probing the final state population simultaneously with a continuous radiofrequency operation. Since the antenna emits all three polarisations simultaneously, the states $(0,0;1,1,1)$ and $(0,0;0,1,1)$ could be coupled by approximately 877.7 MHz for small magnetic field strength, for example, so that with 50 % probability the initial state is achieved at some point in time from where the excitation laser drives the transition to the final state. In order to recognise the excitation of the common mode by the dipole force in the radiative lifetime of 16 ms [72], a suitable method is needed with which the 120 images per second can be evaluated in such a way that the one image (or at most the two images) of interest are extracted.

As this might be associated with some difficulties, it is preferable to proceed first sequentially: The state shown in red in Figure 9.4 is continuously depopulated with

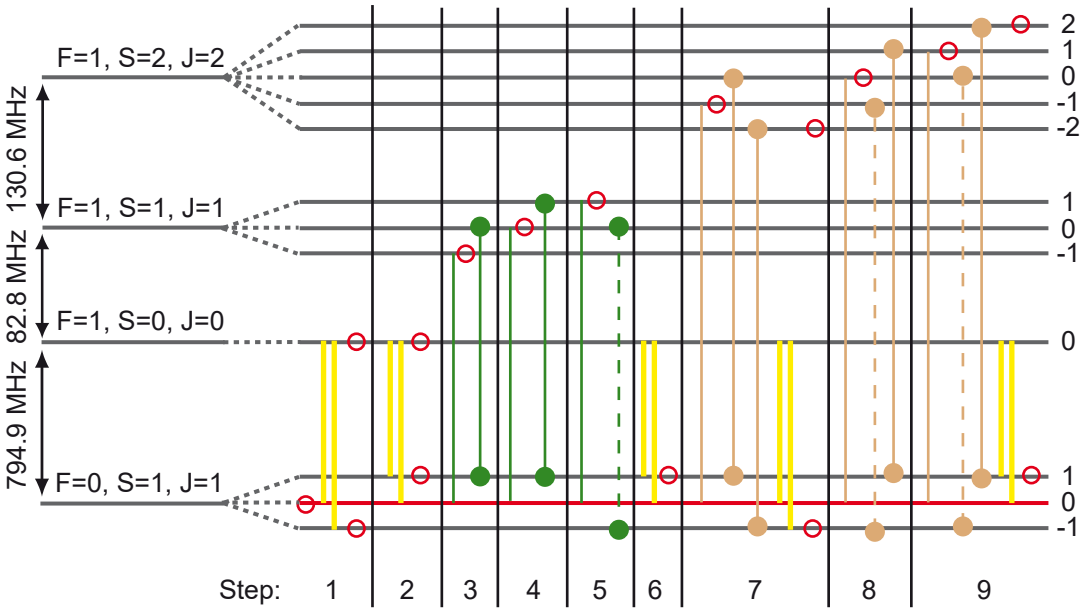

Figure 9.4.: Sequential population transfer to state $(0,0;0,1,1)$ (red line) with three rf frequencies 794.9 MHz (yellow), 877.7 MHz (green) and 1008.3 MHz (brown). Description in the main text.

the excitation laser. The population of the final state is monitored by the ODF. Thus, the MHI is not in this state at the beginning (marked by an empty red circle). In the first step, two radio frequencies of approximately 794.9 MHz (yellow) are continuously applied, which depopulate the states $\left(F=0,S=1,J=1,m_J=-1\right)$ and $(1,0,0,0)$. Next, the frequency is adjusted so that state $(0,1,1,1)$ is depopulated via $(1,0,0,0)$. By applying approximately 877.7 MHz (green), state $(1,1,1,-1)$ is depopulated in step three. However, if the MHI is initially in state $(1,1,1,0)$, then state $(0,1,1,1)$ could now be populated again (full green circles). In the fourth step, the transition between the last-mentioned state and $(1,1,1,1)$ is driven, while at the same time state $(1,1,1,0)$ is depopulated. The last *Zeeman* component of this hyperfine state $(1,1,1,1)$ is depopulated in step 5. Theoretically, a second transition would also be driven (green dashed), but the two connected states are no longer populated by the previous procedure. With the sixth step, which is identical to step 2, the states $F=0$, $S=0$ and $S=1$ are depopulated.

The depopulation of state $S=2$ is shown in the steps 7 to 9 (brown) with approximately 1008.3 MHz radiation. In step 7, three frequencies must be irradiated simultaneously. State $(1,2,2,-1)$ is depopulated while states $(0,1,1,1)$ and $(0,1,1,-1)$ are populated. The latter is depopulated via state $(1,0,0,0)$. Thus, state $(1,2,2,-2)$ is also depopulated. State $(1,2,2,0)$ is depopulated in step 8. Finally (step 9), the three remaining states $(1,2,2,1)$,$(1,2,2,2)$, and $(0,1,1,1)$ are depopulated.

After these steps have been completed while the resonance frequencies have been applied continuously, the MHI has been excited once. It must be reinitialised to the

state ($v = 0$, $L = 0$) using the schema in Figure 1.2 and probing the state (Section 9.1.1) again. If the excitation is not successful, at least one frequency is out of tune.

9.3. Candidate transitions for Spectroscopy

Another candidate for spectroscopy is the transition (0, 0) to (1, 1) at 5.1 µm. With its 59 ms radiative lifetime [72], this state is noticeably longer-lived than (5, 1) and decays only into the initial state or the state (0, 2). In the latter case, the QCL can be used for reinitialisation. This offers a high repetition rate.

With the same ODF source, a pure rotational transition (0, 0) to (0, 1) or highly excited rovibrational transitions (0, 0) to (12, 1) can be studied in a similar way.

Also interesting are the transitions (0, 2) to (5, 1) and (0, 2) to (12, 1). In this case, the ODF could be applied on to the transition (0, 2) to (2, 1) corresponding to 2.75 µm.

10. Summary

In this work, a fully functional system for the spectroscopy of individual MHIs is presented. The system stands out for its versatility. Different ion species have been trapped and studied together with beryllium ions. The beryllium ion serves as a diagnostic tool. Due to its fluorescence, it can be observed directly with a PMT or a camera. The number of stored ions, including invisible species, can be deduced from the positions of the beryllium ion in the trap. By analysing the fluorescence under the influence of a secular excitation, the trap potential can be measured or the mass of the trapped ion species can be determined. By spectroscopy of the beryllium ground state, the local magnetic field strength can be inferred with an uncertainty of a few milligauss at the location of the ion. Systematic effects have been investigated for the characterisation of the system, such as the frequency shift due to the laser or rf intensity as well as the influence of the trap potential depth. It is noticeable that all measurements are limited by a fluctuation of the measured frequencies or by a too small signal to noise ratio. The former could be due to an instability in the homemade trap electronics or the source of the coil current and the latter can be fixed by removing a beam splitter for simultaneous use of the PMT and the camera.

To trap the molecular ion species, the optimal trapping parameters and procedures have been determined for the individual species. Since the HD^+ molecule is to be investigated in the near future, a laser for the quantum state preparation for this MHI has been integrated into the system. Until now, an ion system has been cooled close to the *Doppler* limit. This enables time-resolved observation of chemical reactions between the ion species and the residual gas that are in principal undesirable for spectroscopy. Therefore, a spectroscopy method has been developed that takes this disadvantage into account. The functionality of the method has been demonstrated with a simple destructive spectroscopic measurement: The molecule is dissociated if the wavelength of the spectroscopy laser is resonant with a rovibrational transition. Detuning the laser by 10 GHz prevents this.

For the upcoming precision spectroscopy of any transition, the destructive method on a single ion is impractical. Therefore, non-destructive state detection methods have been prepared. The sophisticated variants using quantum logic and the required

preparation of the ion system into the ground state of the oscillation are postponed in favour of a method using a state-dependent optical dipole force. The laser system for sub-*Doppler* cooling required for both scenarios has been developed and set up. The effect of the ODF is discussed using the example of the fourth overtone spectroscopy of HD^+. A simulation shows that its state can be read out with a high-speed camera using the system developed here.

The results of the hyperfine quantum state preparation of beryllium have to be adapted for the spectroscopy of a single HD^+ ion. A possible scheme has been discussed in detail.

11. Outlook

The completion of the new system enables future interesting comparative measurements between ions in the cluster regime (trap 1 in the previous system) and with single ions (trap 2 in the new system). Both systems are located in the same laboratory and are subject to the same external influences and use the same laser resources, allowing a direct comparison of the trap-induced effects. The repetition of the previous measurement of the $(v = 0, L = 0) \rightarrow (v' = 5, L' = 1)$ transition in MHIs in trap 1 with a single MHI in trap 2 has a clear benefit, as suggested in Section 9.2. After implementation of the non-destructive state detection, these comparative measurements can be carried out in a short time.

In order to make the measurements more efficient, the lifetime of the stored ions must be increased. The limiting factor is currently the high rate of chemical and charge exchange reactions with the residual gas. A further reduction of the pressure should slow down these reactions. To achieve this, the volume of the vacuum chamber must be reduced. This will be done as follows.

With a small modification, the large pipe to the pump station can be removed and the turbomolecular pump can be mounted directly onto the vacuum chamber. This has the additional advantage that the injected molecular hydrogen gas can be pumped out more quickly, reducing one of the most important chemical reactants. The titanium sublimation pump or alternatively another ion pump must then be mounted in place of the electrical feedthroughs of the integrated particle detector. The latter has become obsolete due to mass determination by means of secular excitation. In this way, a lower final pressure is expected with the same pumping capability.

In addition, the imaging unit will be upgraded. Currently the ion fluorescence is divided by a beam splitter to a PMT for fast detection and a camera for imaging. By installing a high-speed camera, we can avoid splitting the signal and improve the signal-noise ratio. A new camera has already been procured and is awaiting installation.

As a final improvement, the trap electronics should be replaced by more stable electronics that has more options for adjusting trapping parameters.

After these steps, new transitions can be investigated on the hetereonuclear HD^+, and the homonuclear isotopologues H_2^+ and D_2^+ can be investigated for the first time

in the trapped and laser-cooled regime. Since the latter are loaded in the same way as HD^+, storing them in the trap should be straightforward. However, it remains to be experimentally determined to what extent these ions are in the initial state for spectroscopy, or how many molecules must be trapped so that on average one survives the state distillation process (Section 8.4).

In the case of HD^+, the transitions (0,0) to (5,1) and (0,0) to (2,2) are suitable for the first studies, since the required laser systems are available. Independent of the species and transition, the dc *Zeeman* effect can then be determined by frequency measurements for different magnetic field strengths. A shift of the measured transition frequency caused by the trap frequency is not expected for a well-compensated trap, but must nevertheless be proven for different potential depths. On the other hand, a frequency shift due to the dc *Stark* effect is expected. The MHI can be shifted out of the trap's centre by applying different voltages to the compensation electrodes. The shift of the measured frequencies due to the laser powers applied during the spectroscopy (ac *Stark* effect) can be calibrated by measuring the transition frequencies with different powers.

It is interesting to see whether the recoil shift observed in trap 1 (but not explained) is no longer present at trap 2.

Appendix

A. Article: Controlled Preparation and Vibrational Excitation of Single Ultracold Molecular Hydrogen Ions

Acknowledgment: This is an article published by Taylor & Francis in Molecular Physics on 17 Nov 2021, available at www.tandfonline.com/10.1080/00268976.2021.2001599: Christian Wellers, Magnus R. Schenkel, Gouri S. Giri, Kenneth R. Brown & Stephan Schiller (2021), "Controlled preparation and vibrational excitation of single ultracold molecular hydrogen ions", Molecular Physics, DOI: 10.1080/00268976.2021.2001599

A.1. Authors' contributions

The experiment was designed by me. All tests and placing into operation of the components were conducted by me. The initial operation of the trap was done in collaboration with Kenneth R. Brown. Under my supervision, Magnus R. Schenkel built the photoionisation laser and the optical detection system. The minimisation of the micromotion was done jointly by Gouri S. Giri, Magnus R. Schenkel and myself. Together with Magnus R. Schenkel, I have loaded the Be^+-N_2^+ system. Gouri S. Giri and I performed the spectroscopy of the hydrogen molecule. The project is based on the ideas of Stephan Schiller. He has been the overall supervisor.

All authors contributed to the analysis, the discussion and presentation of the data and preparation of the manuscript.

A.2. Copyright

The article is exclusively licensed to Taylor & Francis for publishing. I have the right to include the article in my non-commercially published dissertation. In accordance with the agreement, the previous publication in the journal is indicated above.

MOLECULAR PHYSICS e2001599
https://doi.org/10.1080/00268976.2021.2001599

Taylor & Francis
Taylor & Francis Group

L. WOLNIEWICZ SPECIAL ISSUE

Check for updates

Controlled preparation and vibrational excitation of single ultracold molecular hydrogen ions

Christian Wellers [a], Magnus R. Schenkel [a], Gouri S. Giri [a], Kenneth R. Brown [b] and Stephan Schiller [a]

[a]Institut für Experimentalphysik, Heinrich-Heine-Universität Düsseldorf, Düsseldorf, Germany; [b]Departments of Electrical and Computer Engineering, Duke University, Durham, NC, USA

ABSTRACT

A single, trapped and ultracold molecular hydrogen ion is an attractive quantum system for exploring various aspects of fundamental physics, such as the determination of fundamental constants and testing their time-independence. Here we demonstrate, for the first time, controlled loading, sympathetic cooling, mass spectrometric identification, and vibrational excitation of ultracold single HD^+ ions trapped in a tightly confining radiofrequency trap using single laser-cooled Be^+ ions for sympathetic cooling. The apparatus can be used also for preparing other single ions, both lighter and heavier than the coolant ion.

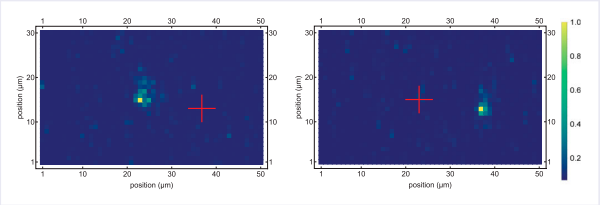

ARTICLE HISTORY
Received 17 September 2021
Accepted 29 October 2021

KEYWORDS
Single-ion trapping; molecular spectroscopy; sympathetic cooling; molecular hydrogen ion

1. Introduction

Trapped ultracold molecular ions are an emerging class of systems allowing highly precise spectroscopic measurements that have relevance in fundamental physics (for a general introduction to low-energy experiments in fundamental physics, see [1,2]). Such measurements enable tests of quantum electrodynamics (QED) of three-body systems [3–5], the determination of some fundamental constants of atomic physics, and searches for physics beyond the Standard Model [4]. As a future perspective, molecular ions could become ideal systems suitable for testing the constancy of the electron-proton mass ratio [6–11].

The fundamental technique for providing the required ultracold molecular ions is the sympathetic cooling of these ions by suitable laser-cooled atomic ions. This technique is very general and powerful, allowing to cool ions of masses 1 u [12] up to masses of several hundred u [13] when applied in the regime where a large number of atomic ions serves as coolant ions ('cluster regime'). Several sympathetically cooled molecular ion species have already been studied spectroscopically by different groups. In the cluster regime, these include the molecular hydrogen ion HD^+ (see below), N_2^+ [14], CaH^+ [15,16], and SiO^+ [17].

Following Dehmelt's paradigm of trapping and spectroscopy [18–20] of a single atomic ion, thereby achieving the best control over environmental conditions and permitting internal state detection, a remarkable effort has been undertaken by several groups to establish similar methods for molecular ions. These efforts have been crowned with notable success. The first quantum-optical manipulation of a single molecular ion was performed on an Mg^+–MgH^+ ion pair. The molecular ion's quantum state was read out, neither destroying the molecule nor its quantum state, by exploiting the strong Coulomb coupling between the two ions [21]. Other investigated two-ion systems, composed of one atomic and one molecular ion, have been Ca^+–CaH^+ [22] and Ca^+–N_2^+ [23]. In the former, coherent control and manipulation of molecular

CONTACT Christian Wellers christian.wellers@hhu.de

© 2021 Informa UK Limited, trading as Taylor & Francis Group

quantum states was demonstrated utilising a variant of quantum logic spectroscopy [24,25]. In the latter, a non-demolition state detection protocol based on coherent motional excitation [26,27] was used. Other systems of interest that bridge the gap between the cluster regime and the two-ion narrative are ion strings composed of two atomic ions and one molecular ion, such as Ca^+ and CaH^+ in [28].

A fascinating family of molecular ions are the molecular hydrogen ions (MHI). These are the simplest molecules, containing a single electron that binds two singly-charged nuclei. Over the last two decades, the precision physics of MHI has made great advances, with improvements in both experimental and theoretical precision by factors in the order of 10^6. The precisions have now reached the fractional level of 10^{-11}–10^{-12} [3–5,29].

Still, there remains a clear potential for further vast improvements. Detailed theoretical studies have predicted that the spectroscopy of MHIs could reach fractional uncertainties at the 10^{-17} level [9,10]. Advancing towards this level requires application of the established techniques of atomic ion clocks. So far, the precision spectroscopy experiments on MHIs were performed in the cluster regime. One important shortcoming of these experiments is the destructive internal state detection technique employed: the spectroscopic excitation of molecular ions is detected by dissociating them into two atoms [30]. This approach leads to a very slow rate of acquisition of spectral data, due to the need to repeatedly refilling the coolant ion cluster with molecular ions. Other disadvantages of experimentation on clusters are the incomplete control over micromotion and the presence of inhomogeneous frequency shifts of the molecular ions in the ensemble. Experimentation with a single trapped and motionally well-controlled MHI holds the promise to circumvent these disadvantages and enable substantial further improvements in spectroscopic precision.

In this work, we lay the foundation toward ultra-high resolution, ultra-high precision spectroscopy of single MHIs. We demonstrate stable trapping and sympathetic cooling of a single MHI in a tightly confining linear ion trap, using a single Be^+ ion as a coolant ion. The focus is on a simple spectroscopy test experiment on single sympathetically cooled HD^+ ions, but the apparatus should be equally suitable for H_2^+ or D_2^+. Additionally, we also show single-molecular ion trapping of another species, N_2^+, in order to demonstrate the flexibility of the apparatus to trap and sympathetically cool molecular ion species that are notably heavier compared to the coolant ion, here by a factor of three. $^{14}N_2^+$ has been identified as a promising candidate for a molecular ion optical clock [8].

The paper is structured as follows: In Section 2 we give a detailed overview of the experimental apparatus. We describe in Section 3 procedures and results on the trapping and laser cooling of the coolant and spectroscopy ions. Section 4 is dedicated to the methods underlying the spectroscopic technique and discussion of the first spectroscopic results. In Section 5 the findings are summarised and an outlook is presented.

2. Experimental setup

2.1. Concept and overview

The apparatus was designed with the goal of sympathetically cooling a few or a single low-mass (< 30 u) molecular ions. In this mass range, molecules are mostly diatomics, but a number of polyatomics are also available, the lightest of which is H_3^+. Of particular interest to our work are the MHIs. The non-radioactive members of this family are H_2^+, HD^+, and D_2^+, with masses 2−4 u. Due to its comparatively low mass, Be^+ is the only practical atomic ion for sympathetically cooling the MHIs. Concerning the low-mass end of the mass spectrum coolable by Be^+ we point out that sympathetic cooling of protons and H_2^+ by a laser-cooled Be^+ ion cluster has been shown in our group in the past [12,31]. On the high-mass side, an experiment at NIST achieved maintaining a single Mg^+ ion (24 u) cold by interaction with a single laser-cooled Be^+ ion, after both ions were individually laser-cooled [32].

In order to achieve one-photon spectroscopy without first-order Doppler broadening, the molecular ion confinement in one spatial direction has to be approximately equal to the wavelength of the spectroscopy radiation or smaller (Dicke condition) [33]. For vibrational spectroscopy of HD^+ or H_2^+ ions, in particular, the wavelengths range from relatively large values, 4–5 μm for the fundamental transitions, to moderately large values for overtone transitions, e.g. 1.4 and 1.1 μm for a fourth- and fifth-overtone transition in HD^+, respectively. This regime has recently been explored in the context of molecular ion strings [3] and it has been shown that a resolved carrier transition could be detected and precisely measured.

Beyond the Dicke condition, the quantum Lamb-Dicke regime has been of central importance in quantum optics of trapped atomic and molecular ions. Here, a substantial reduction in the probability of producing recoil effects upon photon absorption is achieved if the classical oscillation frequency of the trapped ion along the direction of the spectroscopy wave exceeds the recoil energy. Equivalently, the wavelength of the spectroscopy radiation should be much larger than the spatial

width of the vibrational ground state wavefunction in the given trap potential. Then, it is possible to suppress the occurrence of a motional vibrational excitation or deexcitation concomitant with the internal excitation of the molecular ion. Considering transition wavelengths as small as 1.1 μm, with a recoil frequency of approximately 50 kHz for HD^+, one, therefore, must aim for an ion oscillation frequency of 500 kHz or higher, along the axis parallel to the spectroscopy wave vector. An additional condition for achieving high spectral resolution is that the linewidth of the transition is much smaller than the oscillation frequency. Quite generally, for molecular transitions between rovibrational levels in the electronic ground state, the natural linewidths do satisfy this condition. For example, in HD^+, even a high overtone transition such as the fifth overtone exhibits a linewidth of less than 100 Hz.

We designed our apparatus to be able to support different spectroscopy techniques, e.g. destructive detection [30], detection based on applying a near-resonant and therefore internal-state-dependent optical force [21,23,27,34], and quantum logic [22,25].

Figure 1 shows a scheme of the overall system that we have developed. This tabletop setup is capable of producing the required single Be^+ ions routinely by photoionisation, and single molecular ions from electron-beam ionisation of a controlled inlet of gas. One of the important aspects in the apparatus layout is to provide optical access for multiple laser beams from multiple directions, not only transverse and under 45°, but also axially. Another goal is to allow imaging with high spatial resolution. For this purpose, the laser-excited Be^+ ions can be imaged by a lens mounted close to the trap centre in a reentrant window. Our apparatus is equipped with a set of three pairs of Helmholtz coils that allow a precise control of the magnetic field at the location of the ions. This is important in the precision spectroscopy of MHI, especially if the absolute frequency of the transition is in the mid-infrared or THz range [3,4].

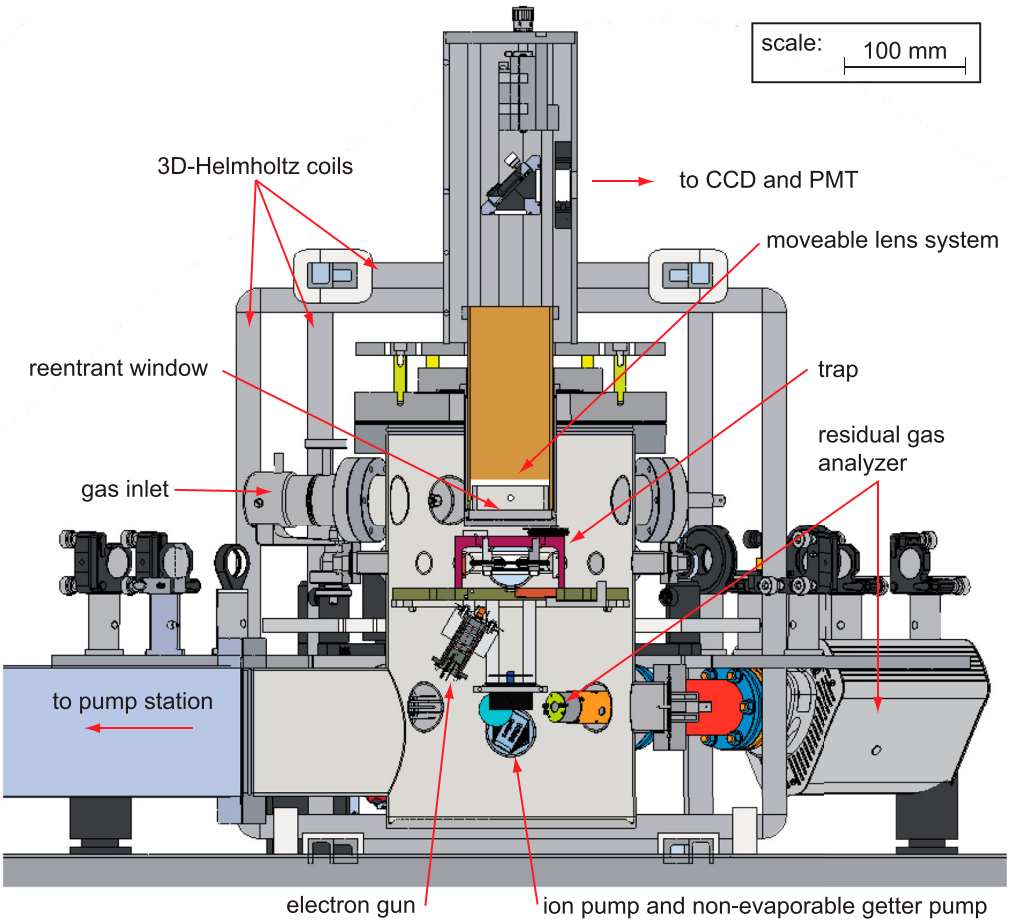

Figure 1. Scheme of the vacuum and imaging system. In the shown perspective, the beryllium ovens are not visible. They are located next to the trap.

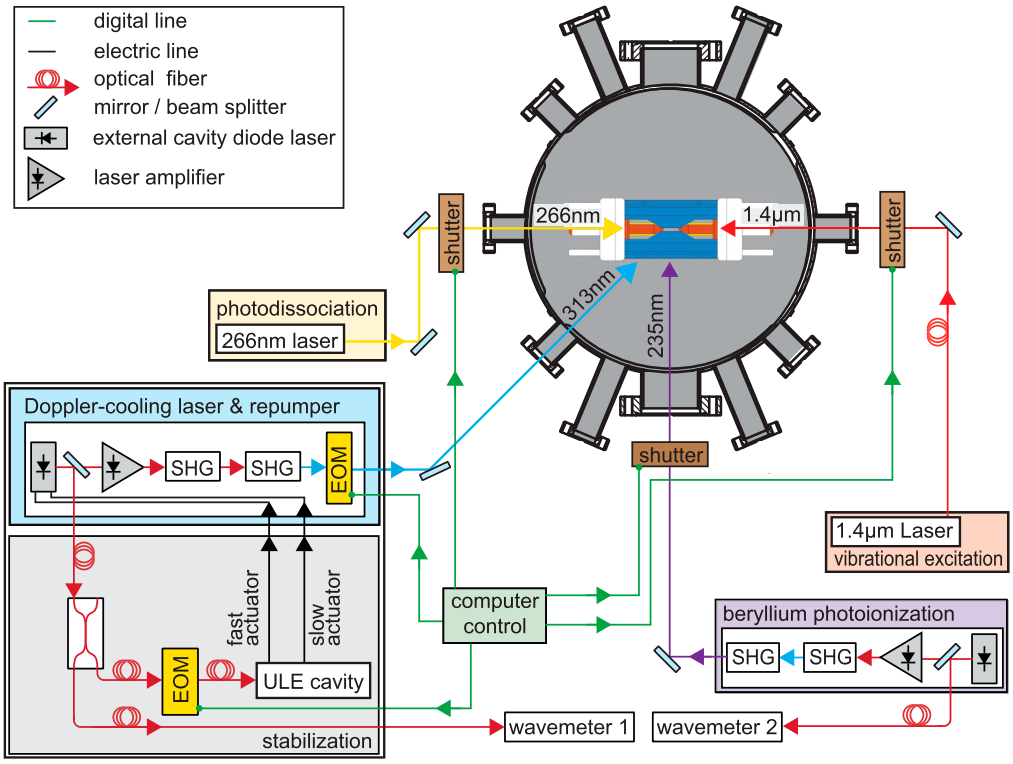

Figure 2. Overview of the laser system and the beam irradiation directions into the trap. EOM: electro-optic modulator; SHG: resonant second-harmonic generation; ULE: ultra-low-expansion glass.

The overall system including the lasers is depicted in Figure 2. At the current stage of development and use, there are four laser systems, the Be^+ cooling laser (blue) together with its frequency stabilisation unit (grey), the beryllium photoionisation laser (purple), the HD^+ vibrational excitation laser (red), and the photodissociation laser (yellow). Power and/or frequencies of all laser waves are computer-controlled (green).

2.2. Trapping apparatus

2.2.1. The trap

We developed a compact linear radiofrequency (rf) trap suitable for the tight confinement of ions (Figure 3). The design was adapted from a design developed at the Universität Innsbruck. It provides optical access from 13 directions (6 axes plus 1 line of vision) and additional non-optical access for the electron gun, ion detector, oven, etc.

The trap is characterised by short distances from the trap symmetry axis to its quadrupole (blade) electrodes, $r_0 = 0.8\,\text{mm}$, and by a short distance of 2.5 mm from the trap centre to the two axial endcap electrodes. The quadrupole electrodes have half-circular ends with a diameter of 0.4 mm. The ions' confinement is realised by applying dc voltages U_{ax} to both endcaps (up to 150 V) and an rf modulation with amplitude U_{rf} (up to 550 V)

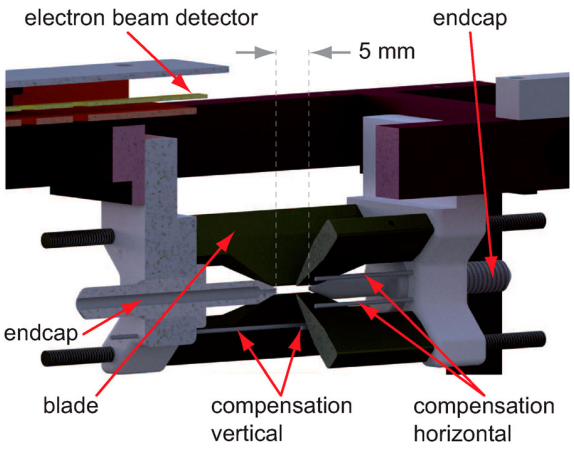

Figure 3. The compact rf trap. Dark green: the four quadrupole electrodes (blade electrodes) for the radial confinement. Grey: the axial 'endcap' electrodes for the axial confinement. Also shown in grey are two sets of two rod electrodes for compensating horizontal and vertical displacements of the ions.

at a frequency $\Omega/(2\pi) = 35.9\,\text{MHz}$. We have developed electronics that allows fast switching of these voltages so that the trap's stability parameters can be changed rapidly. This is useful for the purposes of removing undesired ion species from the initially loaded ion crystal, supporting the ion crystallization process, and adjusting the ions' secular frequencies.

2.2.2. The vacuum system

The trap is mounted in the vacuum system as shown in Figure 1. The trap size with its numerous optical access directions, including the imaging direction and additional non-optical access for the electron gun, ion detector and two beryllium ovens requires a medium-sized vacuum chamber. We opted for an imaging system located in the air. Because it has to provide high spatial resolution, the required high-quality but bulky objective had to be placed very close to the trap centre, inside a reentrant window.

To achieve an ultra-high vacuum condition with a pressure below 10^{-10} mbar, a turbo-molecular pump with a connection flange of 100 mm diameter and an ion pump with additional non-evaporable getter material is used. Additionally, a titanium sublimation pump is occasionally used to remove residual getterable gases and to enhance pumping efficiency. A shutter interfaces the mechanical pumps to the main system, allowing to shut them off, and thereby minimise disturbing vibrations. A quantitative analysis of the composition of the residual background gas is performed on a regular basis using a residual gas analyser.

Two custom-built beryllium ovens are placed close to the trap centre. A slit cover placed 10 mm in front of each oven guides the atomic beam to the trap, avoiding deposition of beryllium on the electrodes. The ovens are attached to a vacuum flange, and therefore can easily be exchanged or maintained by removing the flange.

The alignment of the custom-built electron gun through the trap centre is crucial to avoid an accumulation of stray charges on the trap structure. The alignment can roughly be adjusted by observing a voltage induced by the electron beam on a pair of electrodes placed opposite to the electron gun. One electrode is small, so it provides a signal when hit by electrons passing close to the geometrical trap centre. If the electron beam is misaligned or not well focused, the electrons are detected and blocked by the second large electrode, which also partially protects the reentrant window. To obtain a good alignment, we adjusted the Einzel lens and deflection voltages in the electron gun so as to maximise the voltage appearing on the circuit containing the small electrode, while minimising the voltage on the large-electrode circuit. A fine adjustment is done by observing the effect of the electron beam on a single Be^+ ion: a displacement of the ion is induced and observed on the CCD image, if the electron beam hits some parts of the ion trap. If this occurs, the ion position can be reset by the photoionisation laser, as described below (see Section 3.1).

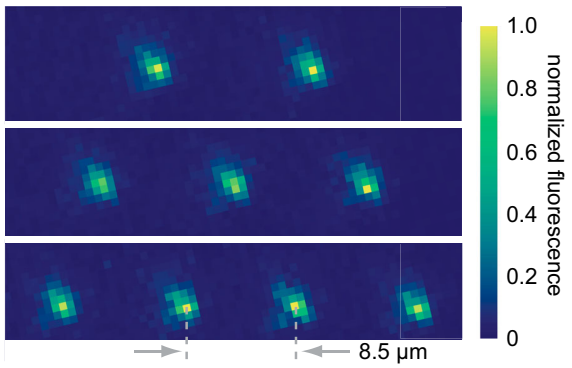

Figure 4. CCD image of small ion strings. For these particular images, the 313 nm cooling laser power was set above the saturation intensity. The trap centre is halfway between the outer ions. From a calibration measurement, one pixel corresponds to 0.55(3) μm.

2.2.3. The detection system

An objective lens system of 50 mm diameter consisting of five lenses and having a focal length of $f = 36$ mm is mounted at that distance from the stored ions, imaging them to infinity. The objective efficiently collects the ion's fluorescence with a good numerical aperture (compare Figure 1). It is mounted inside a reentrant window that is coated on the vacuum side with indium tin oxide (ITO), so as to minimise the effect of stray charges that reach it. The optical path of the light collected by the objective is divided into two branches by a beam splitter, one going to an intensified CCD camera and the other to a photomultiplier tube (PMT).

The objective magnification is 10. We calibrated the magnification by comparing the image of a beryllium ion string with the ion-ion separation distances calculated from the curvature of the axial potential as determined from the axial secular frequency (see Figure 4).

2.3. Laser system

2.3.1. Photoionisation laser

Neutral beryllium atoms in the atomic beam are photoionised close to the trap centre by a 235 nm laser beam, in a 2-step excitation process [35]. The radiation is provided by a commercial 470 nm laser that is resonantly frequency-doubled in a custom-built bow-tie cavity containing a beta barium borate (BBO) crystal (Figure 5). The maximum achievable output power is around 12 mW, however, for reliable operation around 5 mW is sufficient.

The 235 nm output power stability is ±10%, as can be seen in Figure 6. This power level is sufficient for loading a single Be^+ ion within a few seconds. The 940 nm external cavity diode laser inside the 470 nm laser system is

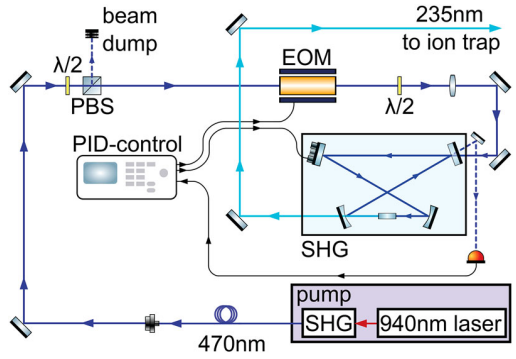

Figure 5. Photoionisation laser. PID-control: proportional-integral-derivative servo system that acts on the cavity length. PBS: polarizing beam splitter cube.

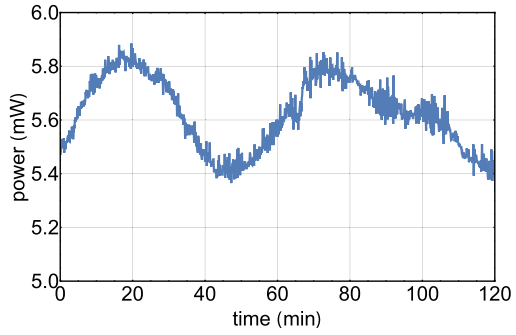

Figure 6. Power stability of the beryllium photoionisation laser output (235 nm). Each point plotted is an average of 50 data points measured.

once tuned to the correct atomic transition wavelength. There is no need to control the laser frequency actively since the Doppler broadening of the beryllium transition is large compared to the frequency drift range of the 940 nm laser.

2.3.2. Cooling laser

The 313 nm laser for cooling Be^+ ions is a commercial resonantly quadrupled amplified diode laser (1252 nm), emitting up to 300 mW at 313 nm. We measured the 1252 nm external cavity diode laser's linewidth by beating against an ultrastable frequency comb. When free-running, the full width at half maximum (FWHM) is approximately 500 kHz.

We have actively frequency-stabilised the 1252 nm laser to an ultra-low expansion (ULE) reference cavity. We use the cavity that was also used in Ref. [36]. For this purpose, a fraction of the laser radiation is phase-modulated by a fibre-coupled waveguide electro-optic modulator (EOM) to imprint sidebands. The modulation frequency is chosen in such a way that the first-order sideband matches the frequency of the TEM00-mode of the reference cavity. A double-modulation technique [37]

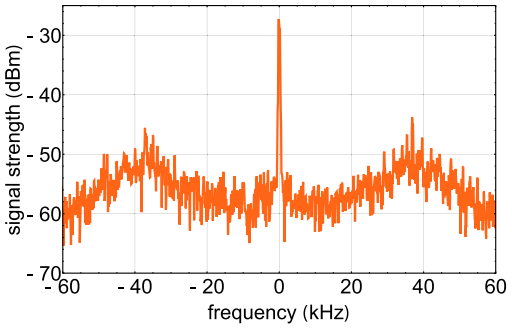

Figure 7. Beat of the frequency-stabilised 1252 nm laser with a mode of an optically stabilised frequency comb. The central peak has a linewidth of 0.4 kHz, due entirely to the 1252 nm laser. The resolution bandwidth is 100 Hz.

allows locking the sideband to the cavity, rather than the carrier, and also enables a fine and precise tuning of the laser by adjusting the sideband frequency. The overall sideband tuneability range is 30–800 MHz. Continuous tuning in the locked state is 20 MHz. The Be^+ atomic transition resonance happens to be at a modulation frequency of 743 MHz. Figure 7 shows the beat of the stabilised 1252 nm laser with the frequency comb. The linewidth is 0.4 kHz and the drift is negligible. Usually, the laser stays in a lock for a whole working day, even when the sidebands are tuned in 200 kHz steps (corresponding to 800 kHz in the UV).

Laser cooling of Be^+ requires a repumper in addition to the Doppler cooling beam. The repumper must be detuned by 1.25 GHz to the red of the actual Doppler cooling transition $^2S_{1/2}(F = 2, m_F = 2) \rightarrow {}^2P_{3/2}(F = 3, m_F = 3)$. These two waves are generated by amplifying and frequency quadrupling the major part of the diode laser wave (1252 nm) and sending the fourth harmonic (313 nm) through a bulk EOM that generates first-order sidebands at 1.25 GHz.

We tune the diode laser frequency such that the (strong) carrier frequency at the fourth harmonic acts as the repumper, depleting the metastable 'dark' state $^2S_{1/2}(F = 1)$ while the blue sideband drives the Doppler cooling transition. By changing the modulation depth, i.e. the rf amplitude applied to the EOM we can easily adjust the power of the Doppler cooling wave. Both repumper and Doppler cooling waves are σ^+-polarised by a waveplate and injected into the trap at 45° with respect to the trap axis, so as to enable Doppler cooling of the ion in all three degrees of freedom. To reduce the background signal on the PMT due to cooling laser light scattered off the trap components, the laser beam is tightly focused. Its FWHM diameter at the ion's position is 46 μm, measured by recording the variation of the fluorescence intensity along a string of beryllium ions as follows. First, the laser beam's focal spot is aligned to

a single trapped ion to achieve maximum fluorescence. Then additional ions are loaded to form a string. Using the fluorescence levels of the outer ions and their theoretically calculated distances from the trap centre, the FWHM diameter of the laser beam is estimated.

2.3.3. Laser for spectroscopy

For vibrational excitation of the HD^+ ion, a commercial 1.4 μm diode laser is employed. Its wavelength can be tuned to the $(\nu = 0, L = 1) \rightarrow (\nu = 4, L = 0)$ transition at 1420 nm. Here, ν is the vibrational quantum number and L is the rotational quantum number. The laser's linewidth is actively broadened to approximately 50 MHz, allowing to cover all intense hyperfine components of the rovibrational transition. To make sure that the HD^+ ion is indeed in the path of the laser beam, the beam is coupled into the trap axially through the endcaps. From theoretical knowledge of the sensitivity of the transition frequency on external fields, we are certain that the frequency shifts from the so far uncontrolled magnetic field or other potential line shifts are well within the linewidth. Using the laser powers measured before the beam enters and after it exits the vacuum system, and approximating the beam waist as the diameter of the holes on the endcap electrodes that guide the laser beam axially, we estimate an intensity of $I_{1420} = 5\,\mathrm{mW/mm^2}$ at the ion's location.

2.3.4. Laser for molecular photodissociation

The photodissociation from the $\nu = 4$ level is performed with a continuous-wave 266 nm laser. The radiation is produced by resonantly doubling 532 nm radiation from a commercial laser in a custom-built cavity. The 266 nm radiation is transported to the trap in free space. The wave is coupled into the trap through the endcap electrodes as well, but counter-propagates with respect to the spectroscopy wave. We infer in the same way as for the spectroscopy laser an intensity of $I_{266} = 60\,\mathrm{mW/mm^2}$ at the ion's position.

3. Ion production and laser cooling

3.1. Beryllium ion preparation

In order to produce an atomic beam, a current is applied to one of the ovens and ramped up slowly to 0.68 A. After 20 s heat-up time, the photoionisation laser beam is unblocked. A typical power of the 235 nm laser measured behind the vacuum chamber is 4.7 mW. The Doppler cooling laser frequency is red-detuned by 10 MHz (Section 3.3) and the beam power is set to 60 μW. Typically, a single Be^+ ion is trapped within 15 s or less, and subsequent ions are loaded every few seconds, using a trap voltage $U_{\mathrm{rf}} = 70\,\mathrm{V}$. Simultaneous loading of two or three ions is observed when the cooling laser frequency is further red-detuned by an additional 4 MHz, the beam power is higher (0.5 mW) and the trap voltage is increased to $U_{\mathrm{rf}} = 100\,\mathrm{V}$.

In order to load a single Be^+ ion, the current to the oven is turned off manually and the photoionisation laser beam is blocked as soon as the first ion is observed on the CCD image or PMT. Even if the ion is initially hot and thus cannot be seen on the CCD image, a small increase in fluorescence level can be detected with the PMT and the loading process can be stopped. In the rare cases when two or more Be^+ ions are trapped during this procedure, the trap's rf amplitude is subsequently reduced to a value where the quasipotential curvature in one radial direction is smaller than the axial curvature, causing a reorientation of the ion string by 90°, from axial to radial. Now, the ions are no longer in the node line of the rf potential and therefore exposed to higher micromotion heating. In approximately half the applications of this procedure, all but one Be^+ ion leave the trap. When this is observed, the trap's rf amplitude is restored to its nominal value.

A single Be^+ ion typically remains trapped for several tens of minutes. Repeated loading of HD^+ ions using the electron gun (see Section 3.5) results in charging of the trap electrodes and a gradual deterioration in the lifetime of a single Be^+ ion is observed. Nevertheless, a maximum storage time of 85 min has been observed for a single Be^+ ion which was exposed to several HD^+ loading attempts and a total of 16 spectroscopy cycles (see Section 4).

The photoionisation laser at 235 nm also causes reversible charging of the trap electrode. Its effect appears to counteract that of the electron gun. After multiple HD^+ loading attempts, a drastic shift in the position of the Be^+ ion from the trap centre is observed on the CCD image. In extreme circumstances, a substantial drop in the Be^+ ion's fluorescence level is detected in the PMT signal. A short exposure of the trap structure to the photoionisation laser beam appears to restore the ion's position. Therefore, when necessary, we unblock the photoionisation laser beam for 3–5 s prior to a molecular spectroscopy cycle.

3.2. Secular excitation

Successful loading and cooling of a single Be^+ ion is verified in real time by observing the ion's position and fluorescence level on a CCD camera and on a PMT. Subsequently, an rf signal with an amplitude on the order of millivolts and a frequency sweep around the axial secular frequency ω_1 may be applied to one of the endcap electrodes to excite the ion's axial oscillatory motion.

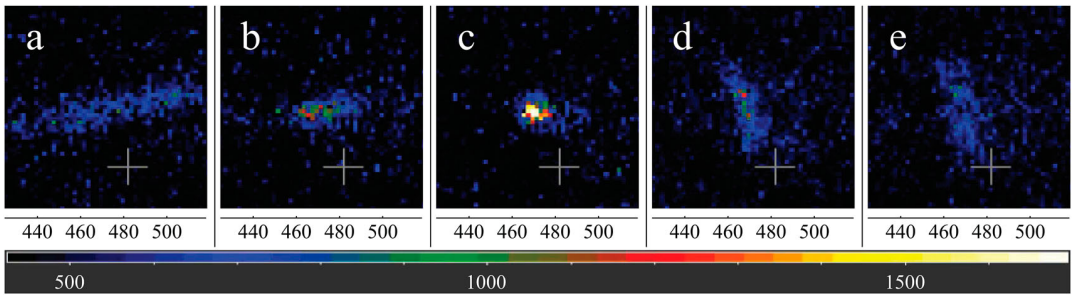

Figure 8. Forced axial and radial secular oscillations of a single beryllium ion under typical laser cooling conditions. The centre CCD image (c) shows the ion when no excitation voltage is applied. The amplitude for axial excitation increases from (b) to (a). Panels (d) and (e) show a weak and strong radial excitation, respectively. The axes units are in pixel (0.5 μm). The crosshair cursor in each panel is a reference point. The colour spectrum is the fluorescence signal level.

Table 1. Normal modes and eigenfrequencies of an HD^+–Be^+ pair (predicted) and of a single Be^+ ion (measured).

			HD^+		$^9Be^+$				
	Mode α	Frequency $\omega_\alpha/(2\pi)$ (kHz)	$e'_{x,\alpha}$	$e'_{y,\alpha}$	$e'_{z,\alpha}$	$e'_{x,\alpha}$	$e'_{y,\alpha}$	$e'_{z,\alpha}$	Mode type
Predicted	6	1860.17	0.9999	0.0000	0.0000	0.0119	0.0000	0.0000	Radial (x) in-phase
	5	1699.74	0.0000	0.9999	0.0000	0.0000	0.0143	0.0000	Radial (y) in-phase
	4	599.93	0.0119	0.0000	0.0000	−0.9999	0.0000	0.0000	Radial (x) out-of-phase
	3	543.71	0.0000	−0.0143	0.0000	0.0000	0.9999	0.0000	Radial (y) out-of-phase
	2	532.57	0.0000	0.0000	0.9365	0.0000	0.0000	−0.3507	Axial out-of-phase
	1	240.93	0.0000	0.0000	0.3507	0.0000	0.0000	0.9365	Axial in-phase
Measured	3	617.90(70)		–		1	0	0	Radial (x)
	2	563.56(28)		–		0	1	0	Radial (y)
	1	207.1(3.0)		–		0	0	1	Axial

Notes: The frequency values for a single Be^+ ion (bottom three rows) are experimentally measured and those for the HD^+–Be^+ pair are calculated. Here, $e'_{i,\alpha}$, $i = x, y, z$, are the eigenvectors in a mass-weighted coordinate system, defined as $x' = \sqrt{m}\,x$, etc., where m is the mass of the respective particle [38].

When the applied excitation frequency approaches the secular frequency ω_1, the amplitude of the ion's motion increases resulting in an increase in the ion's extent as detected on the CCD camera. Figure 8 shows typical scenarios. The small oscillation amplitudes (cases (b) and (d)) are observable on the CCD image, but are not detectable on the PMT signal – there is almost no change in fluorescence level.

The increased motional energy of the ion also reduces its mean fluorescence level when it is irradiated by the red-detuned Doppler cooling light. This fluorescence is detected by the PMT and represents a signal that can be recorded as a function of the excitation frequency. This procedure will be referred to as a secular scan in the remainder of the paper. Figure 11 (blue) shows a typical secular scan when a single cold beryllium ion is present in the trap. The axial resonance frequency is clearly observed. For an endcap voltage $U_{ax} = 3$ V the resonance frequency is measured to be $\omega_1(Be^+)/(2\pi) =$ 207 kHz (compare Figure 11, blue data).

Secular scans are also applied when a single Be^+ ion is paired with another ion. To interpret the spectrum, it is essential to know the eigenmode frequencies of such a system. They are easily calculated, see e.g. [38]. Generally, the axial potential curvature and the ions' mass and charge are the input parameters that determine the axial single-ion, axial ion-pair and also axial ion-string mode frequencies. Those parameters plus the radial rf pseudopotential curvature then determine the radial eigenfrequencies of ion chains. Conversely, the experimental result for the single-ion $\omega_1(Be^+)$ provides us with the axial potential curvature and thus we can predict the two axial eigenmode frequencies ω_1, ω_2 of a Be^+–HD^+ ion pair, see Table 1. From a measurement of the radial single-Be^+ secular frequencies, we obtain the radial pseudopotential curvature and can then compute the radial eigenfrequencies of the ion pair. Both the measured single-ion and calculated ion pair frequencies are reported in Table 1.

3.3. Micromotion minimisation

In the regime of efficient Doppler cooling (weak intensity) we expect the fluorescence spectral lineshape to be a Lorentzian, whose linewith is due to spontaneous emission, and only a small contribution from power broadening. We indeed find that the spectrum of a single ion is well described by such a profile, see blue data and fit in Figure 9. The fit gives a FWHM of 23 MHz, to be compared to the natural FWHM of 19.4 MHz. This shows that little power broadening is present. In order to achieve

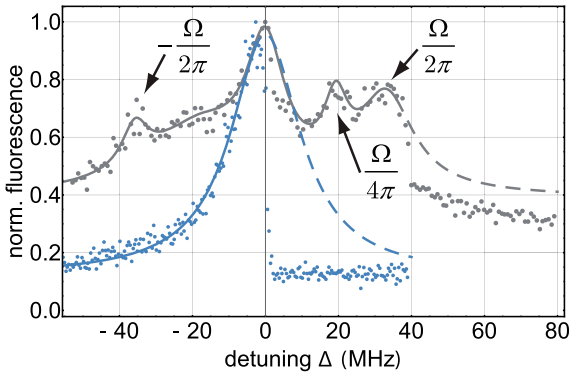

Figure 9. Optical resonance of the 313 nm transition of a single laser-cooled beryllium ion. A well-compensated trap shows a clean resonance (blue); in the opposite case (grey), optical sidebands appear. The zero of the indicated detuning values Δ of the cooling laser frequency has been set at the point of maximum fluorescence. Each data point is a 0.1 s average of the PMT signal. The blue line is a Lorentzian fit; the grey line is a fit using 5 Lorentzians.

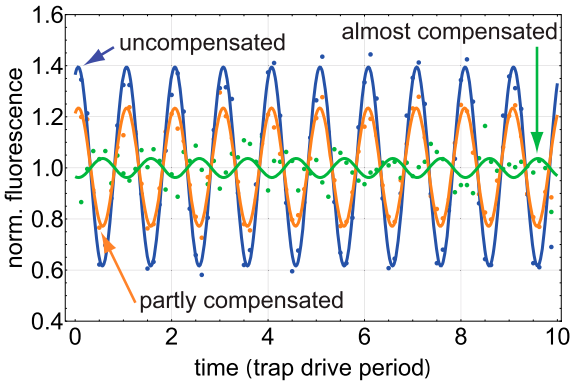

Figure 10. Micromotion of a single Be^+ ion. Green: in an almost-compensated trap, a micromotion-induced fluorescence modulation does almost not appear in the fluorescence signal. For different settings of the compensation voltages, a modulation is discernible. Orange: partly compensated trap; blue: uncompensated trap. The lines are sinusoidal fits to the data.

the best laser cooling efficiency, we detune the laser frequency to the point of maximum slope of the profile. In this case, it is $\Delta_{opt} = -10$ MHz. As is well-known, when the laser frequency is blue detuned, the ion is heated and the fluorescence drops. In our experiment, the drop is as low as the background PMT counts level and occurs at a detuning very close to that of maximum fluorescence. These observations hold for a well-compensated trap.

If a stray static electric field, especially the stray field caused by the electron beam having charged the electrodes or other parts of the trap structure, is present in the trap centre (i.e. the trap is not well compensated), a single or multiple ions will experience considerable micromotion. This shows up as sidebands in the optical spectrum (grey). The interaction between the ion and the single-frequency cooling laser is now more complex, with a competition of cooling and heating on the various sidebands and carrier taking place. As a result, we find that overall heating of a single ion occurs only when the laser detuning is equal to the blue micromotion sideband at $\Delta = +35.9$ MHz. The seeming appearance of a resonance at $\Omega/4\pi$ is not fully understood and is likely caused by some parametric excitation.

The strength of the micromotion sidebands compared to the mean fluorescence of an ion not experiencing micromotion can be determined also in the time domain [39]. We record the PMT counts with high bandwidth using a field programmable gate array (FPGA). Afterwards, we map the times of photodetection events to the phase of the trap rf drive. In Figure 10 40 s of acquired data are mapped onto 10 trap periods. An uncompensated trap leads to a fluorescence modulation of ±40% (blue). An adjustment of the applied compensation voltages by $\Delta U_{hor} = -0.6$ V and $\Delta U_{ver} = +0.2$ V led to a reduction of modulation by approximately a factor of 2 (orange). For the settings $\Delta U_{hor} = -0.2$ V and $\Delta U_{ver} = +0.2$ V (green) the fluorescence modulation is reduced further to 4(1) %.

The above time-correlation method can be applied to minimise the micromotion amplitude by optimising the compensation voltages. This results in shifting the ion's position to the rf node line and to the axial potential minimum. The ion's position for a well-compensated trap is then marked on the CCD image. When introducing new stray charges or fields e.g. due to electron beam-induced ionisation of HD, a shift of the ion's position and a blurring of its image occurs. In such circumstances, a quick but rough micromotion compensation may be performed, as opposed to a careful measurement of rf-photon correlation described above. This is achieved by altering the compensation voltages and visually controlling the CCD image, with the goal to push the ion back to the marked position on the CCD image. This procedure looks similar to the change from (d) to (c) in Figure 8, with the spatial spread of the Be^+ ion image being noticeably reduced.

3.4. Ion temperature

The ion's translational temperature may be determined by the method described in ref. [40]. Assuming an ion's spatial distribution as a normal distribution, as one would expect from thermal motion, and neglecting the contribution due to imaging errors of the imaging system (the point spread function), the axial temperature is estimated to be 0.5 mK. Here, the influence of micromotion for oscillations along the trap axis is neglected and the required Gaussian root mean square (RMS) width

is obtained by averaging the fluorescence data collected by the CCD and fitting a Gaussian distribution function to the averaged data. The same procedure is followed also for the radial direction and a temperature of 8 mK is estimated.

3.5. Molecular ion preparation

There are two basic approaches to the production of positively charged ions: electron impact ionisation and photoionisation. Laser-induced photoionisation is a 'clean' technique since charging of the surrounding materials can generally be avoided with modest efforts on beam shaping and alignment. The photoionisation of MHI requires a complex laser system tuned to specific wavelengths in the UV region [41–44], but has the advantage of producing the ions in a small range of rovibrational states. Different states can be produced by driving appropriate rovibrational components of electronic transitions.

In contrast, ionisation by electron impact is a very general technique and of great simplicity. Any kind of molecule can be ionised, with the disadvantage of a wide probability distribution in terms of rovibrational levels. This is especially relevant and perhaps problematic in the case of homonuclear diatomic molecular ions (e.g. H_2^+, N_2^+) in the ground electronic state: the vibrationally excited levels are metastable. Thus, the preparation of such molecules in the ground vibrational state is a challenge, so that electron impact ionisation may have to be complemented by buffer gas cooling [45]. On the contrary, for heteronuclear MHI (e.g. HD^+), the lifetime of the excited rovibrational levels is in the order of 10–50 ms (Figure 13). Therefore, within a short time, decay to the ground level $\nu = 0$ occurs, since blackbody excitation from that level to higher vibrational levels is negligible. However, several rotational levels are occupied under steady-state condition, where spontaneous emission balances blackbody excitation. The steady-state is reached in a few minutes, an acceptable duration in experiments undertaken so far.

The HD^+ loading follows the trapping of a single Be^+. Referring to Figure 14, the cooling laser power is increased to 150 μW and the trap drive rf amplitude is decreased to $U_{rf} = 40$ V. This corresponds to a level at which species of mass larger than beryllium are not trapped stably or the capturing probability is practically zero. Then, a magnetic field is applied, for the purpose of deflecting the electron beam away from the trap during the electron gun's filament warm-up period. After 8 s, the applied magnetic field is switched off, returning the electron beam to the trap centre. At the same time, a small amount of the molecular gas is introduced by a piezo-electric leak valve, whereby we allow the pressure to rise to 3.8×10^{-10} mbar. Since the shutter to the pump station is open, a continuous flow of HD gas is needed. On the CCD camera, a shift in the position of the Be^+ ion can be observed, caused by electrode charging effects. As a consequence, the PMT records a decreasing fluorescence.

A trapping event is indicated by a spike in the fluorescence signal. Three cases must be distinguished: (i) the captured ion crystallizes immediately and a jump of the Be^+ position can be observed on the CCD, followed by multiple fast position swaps during the sympathetic cooling process. (ii) the captured ion does not crystallize immediately. This indicates more than one captured molecular ion and (iii) the capture failed and the molecular ion is lost. But the Be^+ ion position has nevertheless changed and the ion's image spread is larger due to heating effects.

For the cases of successful loading (case i and ii) the Be^+–HD^+ system needs to be cooled efficiently, for which the following procedures have been experimentally verified. In all cases, the trap rf drive amplitude is slowly increased over the course of a few seconds to restore the nominal value of 70 V. For case (i) the swapping rate decreases and the ions come to rest. The same is true for a previously non-crystallized ion pair. If needed (case ii), the cooling laser power is increased by a factor of 10. If this still does not show any effect, the trap drive amplitude is decreased to 27 V. This leads to a reorientation of the ion pair or string by 90°, from axial to radial, resulting in an ion loss as described in Section 3.1 for beryllium. Alternatively, a 1 to 5 MHz radial secular scan with high amplitude is applied. In this way radial oscillation modes having high amplitudes for the molecular ion are excited. For example, in the case of a two-ion system, as shown in Table 1, this scan would excite the two radial in-phase modes $\omega_5/(2\pi) = 1700$ kHz and $\omega_6/(2\pi) = 1860$ kHz, whose Be^+ oscillation amplitudes are 49 and 40 times smaller than the one of HD^+, respectively. This will remove some or all molecular ions of the trap.

The effect of this procedure is verified by an axial secular scan (180 to 280 kHz in 30 s). Figure 11 shows in red a typical scan of a Be^+–HD^+ pair. For the given trap settings, the axial in-phase mode resonance of the Be^+–HD^+ pair is predicted at $\omega_1/(2\pi) = 241$ kHz, see Table 1; it is measured to be 241.17(30) kHz.

The axial excitation is large enough for the two ions to swap their positions during the scan, before and after the in-phase resonance (but not on-resonance). This is because the scan heats the ion pair, in most cases close to its 'melting point', followed by a re-crystallization that may be accompanied by a swap of ion positions. Figure 12 shows an example. The effect is observable

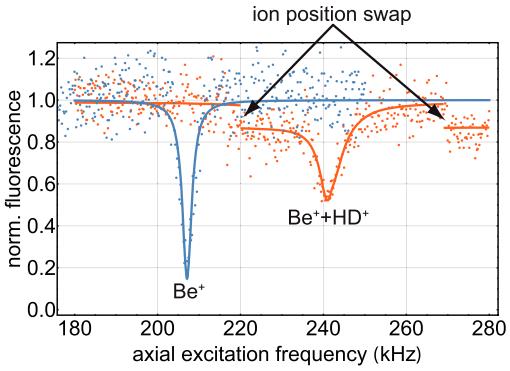

Figure 11. Axial in-phase secular scans for a single Be^+ ion (blue) and a Be^+–HD^+ pair (red), measured in different experiments. In the latter case, the ions exchanged their positions twice.

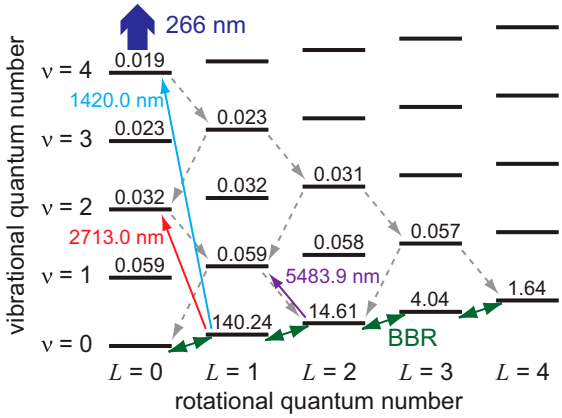

Figure 13. Partial rovibrational energy scheme of HD^+ (not to scale). In thermal equilibrium, the lower spectroscopy level ($v = 0, L = 1$) is populated by 300 K blackbody radiation (BBR, green) that continually induces transitions between the rotational levels of the ground vibrational state. Simultaneously, spontaneous emission processes $L \to L - 1$ take place (not shown). The lower spectroscopy level can be excited to the level ($v = 4, L = 0$) by 1420 nm radiation (light blue). An ion in that upper level can be dissociated by 266 nm radiation (dark blue) or it decays back to the vibrational ground state via spontaneous emission within less than 1 s, reaching first one of the rotational states $L = 0$, 2 or 4. Grey dashed arrows show the dominant spontaneous emission processes. BBR and spontaneous emissions within the $v = 0$ manifold eventually lead to occasional population of the lower spectroscopy level $L = 1$. The numbers are the natural lifetimes of the levels, in seconds [46].

with the PMT, because at the two positions of the Be^+ ion a 10% difference in the mean fluorescence level is observed, a change that can be resolved. Usually, the Be^+ and HD^+ ions do not change places once they are crystallized and no scan is applied. If an axial frequency different from 241 kHz is measured in a secular scan, this indicates that an undesired second ion has been trapped. This ion is therefore removed with the methods explained above.

Sometimes, (case iii), the single Be^+ ion's image in the imaging plane is located at one of the two positions of a two-ion string after a failed capture or even after the loss of the molecular ion. This is a result of the charging of trap electrodes by the electron beam. A short exposure of the trap structure to the photoionisation laser restores the ion's original position. We observed that this procedure shrinks the ion's spread, indicating a reduction in heating effects.

4. Spectroscopy

The energy levels relevant to this work are displayed in Figure 13. We choose to address a transition that starts from the rotational level $L = 1$ in the vibrational ground level because this has the near-maximum theoretical occupation probability in thermal equilibrium, $p(v = 0, L = 1) = 0.25$ [47]. We choose ($v = 4, L = 0$) as the upper level because the corresponding transition wavelength (1420 nm) is easily available, and because the zero rotational angular momentum simplifies the hyperfine structure. The spectroscopic procedure is portrayed in Figure 14.

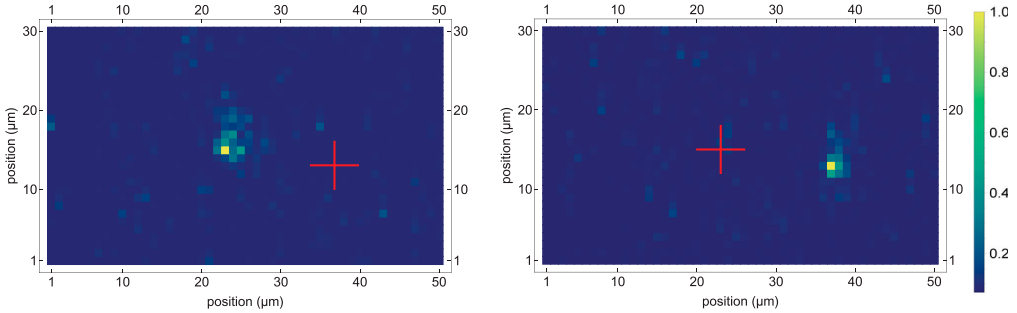

Figure 12. CCD images of a Be^+–HD^+ pair. The Be^+ ion can be seen at the two positions of the ion pair. The red cross serves as a guide to the eye and is located at the assumed position of the MHI. The right image is taken after the HD^+ ion is loaded. The left image is taken immediately after a position swap has been observed, shortly after a secular excitation scan. 3V are applied both endcaps. The apparent difference in the Be^+ ion image extension is attributed to the charging of trap electrodes due to the use of the electron gun for HD^+ loading.

After loading and verifying the presence of a single co-trapped HD^+ ion by means of a secular scan as described in Section 3.5, the spectroscopy and dissociation lasers irradiate the ion for 10 s. If the ion is in the desired initial level ($v = 0, L = 1$), populated by blackbody radiation (BBR), it can be excited by the spectroscopy laser into the higher rovibrational level ($v = 4, L = 0$). In this case, the dissociation laser excites the ion further into the anti-binding $2p\sigma$ state with essentially unit probability, and the ion dissociates. The theoretical cross section for this process is $8.5 \times 10^{-18}\,\mathrm{cm}^2$ at the wavelength 266 nm [48]. The two dissociation channels $H(1s) + D^+$ or $D(1s) + H^+$ can take place. Only in a fraction of cases, the dissociation of HD^+ leads to the observation of a sudden change of the Be^+ ion's position on the CCD image (compare Figure 12) as a consequence of the removal of the HD^+ ion. We believe that the dissociated fragments of HD sometime react chemically with the residual gas or that a charge exchange takes place. In these events, the newly formed ion remains in the trap. This statement is supported by two observations: (a) a restoration of the Be^+ ion's position to the trap centre is not visible on the CCD image, and (b) a subsequent secular excitation scan reveals an unexpected low-frequency resonance indicating the presence of a heavy sympathetically cooled molecular ion.

A quick axial excitation scan of the type shown in Figure 11, but shortened from 30 to 6 s, is applied to verify if the Be^+–HD^+ pair's in-phase resonance is present or not. If it is absent, this proves that dissociation of the HD^+ ion has taken place. If it is still present, both lasers are unblocked for 20 s and a second secular scan is performed afterwards. If the HD^+ ion is still trapped, the procedure is repeated for the last time, but now the lasers are unblocked for 30 s.

Afterwards, the molecular ion is removed by applying a strong radial out-of-phase excitation (as discussed in Section 3.5) and a new MHI is loaded into the trap. Then the cycle is repeated. A complete loading - excitation - detection - cleaning cycle has a duration of approximately 2 min.

We performed a total of 18 HD^+ preparation and excitation cycles and observed that out of the 18 single HD^+ ions, 5 were dissociated in 10 s, 4 in the subsequent 20 s and 4 more in the final 30 s. We also performed the same procedure with the spectroscopy laser detuned by $\Delta_{\mathrm{spec}} = +10\,\mathrm{GHz}$ from the resonance. Out of 9 HD^+ single ions none was dissociated in 10 s and none in the subsequent 20 s, but one ion was lost during the last 30 s run. This single observed ion loss is most likely not due to a dissociation event, but rather due to a long storage time of the ion leading to a chemical reaction. Consequently, also for the on-resonance case, such an event could have occurred. A display of these results is shown in Figure 15. For a qualitative understanding of the observation, we compute the normalised excitation rate of the rovibrational transition, using the known transition dipole moment and ignoring the hyperfine structure. The value is $1.4\,\mathrm{s}^{-1}/(\mathrm{mW/mm}^2)$, assuming a gas at 8 mK translational temperature and a laser spectrum narrower than the Doppler width of 4 MHz. We estimate that the effect of the hyperfine structure present and the actual laser linewidth yields an effective excitation rate reduced by a factor of the order 10^2, the product

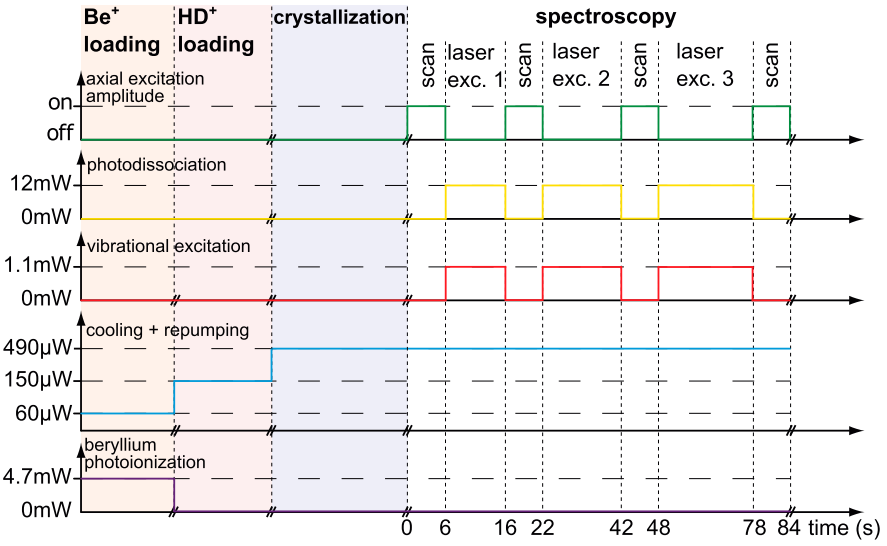

Figure 14. Timing diagram for the spectroscopy on single HD^+ ions. The spectroscopy laser (red) and the dissociation laser (yellow) simultaneously irradiate the HD^+ ion for 10 s, then 20 s and finally 30 s. Before and after each irradiation period a secular scan (green) is performed to probe whether the single HD^+ is still present or not.

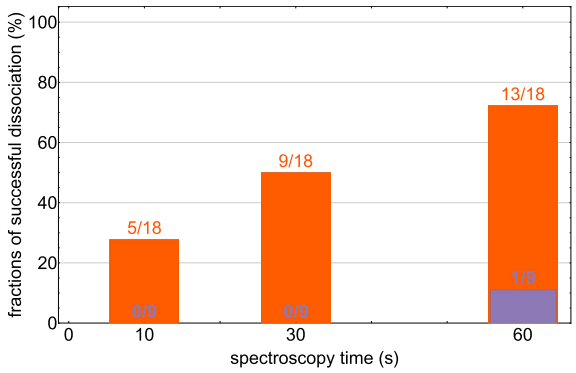

Figure 15. Results of vibrational excitation – dissociation of a set of single HD^+ ions. The three columns show the cumulated fractions of successful HD^+ ion dissociations after 10, 30 and 60 s of cumulative irradiation time by the 1420 nm and 266 nm lasers, respectively. Orange: the spectroscopy laser is tuned to resonance, the ion loss is significant. Blue: the spectroscopy laser is detuned by +10 GHz. The one event that occurred within the last 30 s might be due to a reaction with residual gas in the vacuum chamber during the relatively long storage time of this specific ion.

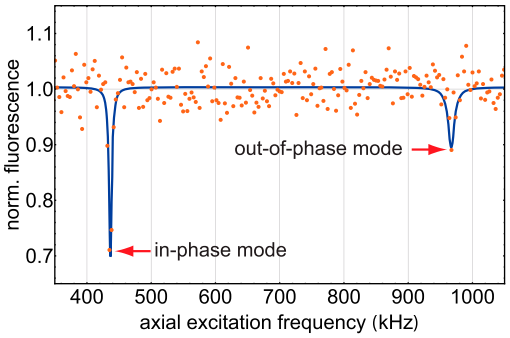

Figure 16. Typical axial frequency spectrum of a Be^+–N_2^+ ion pair. The first resonance is the in-phase axial mode, the second is the out-of-phase mode. Scan duration: 30 s. The blue line is a guide to the eye.

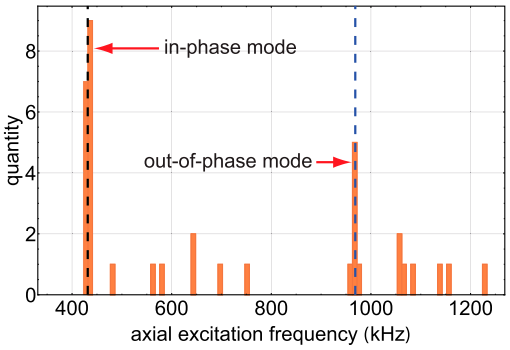

Figure 17. Histogram of Be^+–N_2^+ ion-pair axial resonance frequencies as observed during a number of scans. The theoretically predicted values for the axial in-phase (black, ω_1) and axial out-of-phase (blue, ω_2) modes are indicated by dashed lines.

of the number of hyperfine components (10) and the ratio of laser linewidth to Doppler width (12). Given the above value of I_{1420} this leads to an excitation rate of $\approx 0.07\ s^{-1}$ if the molecules are in the initial level. Since the thermal population fraction of that state is 0.25, after a 10 s irradiation, the ensemble-averaged cumulative excitation probability is ≈ 0.2. The observed excitation probabilities are in rough agreement with this simple estimate. The action of the excitation lasers on single molecular ions is convincing. Due to the facts that the vibrational excitation laser intensity is low and that the HD^+ ions are not prepared and do not permanently stay in the initial spectroscopy level, a time-dependent cumulative dissociation probability is observed.

4.1. Other ion species

The apparatus features the ability to trap various ion species that can be sympathetically cooled by the atomic ion. As an example, a Be^+–N_2^+ ion pair is prepared as follows.

We first prepare a single Be^+ in the trap and measure its axial ($\omega_1/(2\pi) \approx 652$ kHz) and radial ($\omega_2/(2\pi) \approx 1.665$ MHz and $\omega_3/(2\pi) \approx 1.673$ MHz) secular frequencies by applying excitation scans as described above. Using these values, we compute the eigenfrequencies of the Be^+–N_2^+ system, in the same way as done for the Be^+–HD^+ system.

An N_2^+ ion is loaded in a similar way as an HD^+ ion and excitation scans are performed. A typical scan result is shown in Figure 16. The PMT signal (red dots, normalised) and the corresponding fit to the data (solid blue line) show the axial in-phase resonance $\omega_1/(2\pi) \approx 436.7$ kHz and the axial out-of-phase resonance $\omega_2/(2\pi) \approx 967.1$ kHz. The axial out-of-phase resonance is less efficiently excited because the lighter ion (Be^+) oscillates with a smaller amplitude than in the in-phase mode (see Table 1). This results in a signal on the PMT that is almost hidden in the noise, but was confirmed by a clearly visible excitation on the CCD camera (comparable to Figure 8(b)), as discussed above. The results of the resonances observed in a number of scans are gathered in a histogram (Figure 17).

A comparison of the measured frequencies with the calculated frequencies $\omega_1/(2\pi) \approx 431.5$ kHz and $\omega_2/(2\pi) \approx 986.9$ kHz, proves the dark ion to be N_2^+. The histogram Figure 17 also contains unknown resonances. These can be explained by random position changes or collisions with residual gas occurring during the scans.

5. Discussion and conclusions

A system suited for a range of quantum-optical studies on various single molecular ions has been designed, built and characterised. At present, single HD^+- and single N_2^+- ions are reliably prepared in the trap, where they are sympathetically cooled to sub-millikelvin axial secular temperatures. Current storage times for the single molecular ions are already sufficiently long for permitting precision spectroscopic studies.

A proof of the overall functionality is given by demonstrating the induction and detection of a vibrational transition on single MHIs. The initial state is a thermally populated rotational state that is excited to a higher rovibrational state by a continuous-wave laser and then photodissociated. The photodissociation is verified by careful observation of the ion positions and analysis of the secular excitation scans. We find evidence of chemical reaction or charge exchange of HD^+ fragments with the residual gas, resulting in the co-trapping of an unwanted heavier molecular ion species. We do not observe that the fragments H^+ or D^+ remain trapped together with the beryllium ion.

Towards the implementation of high-precision spectroscopy of a single MHI, it is important to improve the probability that the prepared single ion is in the desired initial state for spectroscopy. For the heteronuclear HD^+ molecule this can be done via rotational cooling [47] (red and purple arrows in Figure 13), a technique well-established in our laboratory, while for the homonuclear H_2^+ molecule other techniques have to be applied, for example selective photodissociation of those ions that are in unwanted vibrational states. A more advanced preparation is hyperfine state preparation [49], a technique that still requires more development. The availability of such techniques will shorten the data acquisition time, improve the data statistics, and allow application of certain types of nondestructive internal state read out.

We believe that once rotational cooling is implemented, the apparatus could in principle be used for precision spectroscopy on single molecular hydrogen ions, achieving precision at the 10^{-13} fractional level with acceptable effort. Two reasons for this are that (i) accurate theoretical predictions for the transition frequencies are already available and therefore the transitions do not need to be searched for over substantial frequency intervals, and (ii) the excitation spectrum of a transition will exhibit an ultra-narrow resolved carrier component, as can be inferred from our observations with HD^+ ion strings in a beryllium cluster. Based on our results in Section 4, we find that with approximately 20 single-ion preparation and excitation cycles we can obtain one data point of the spectrum (excitation probability) with reasonable signal-to-noise ratio. We expect that we can enhance the system performance so as to obtain two data points per day. Thus, one transition line can be measured within one week, with an expected linewidth at the 10^{-13} fractional level. Our past experience in characterising systematics indicates that a line needs to be measured half-a-dozen times in order to verify the systematic shifts, by varying in succession magnetic field, spectroscopy laser power, trap rf amplitude, and cooling laser intensity by a factor of two. Altogether, within a two-month period the transition frequency of a suitably chosen Zeeman component of a rovibrational transition could be determined with a fractional uncertainty lower than 10^{-12}.

An important question is how thight the confinement of the MHI is for the conditions realised in the apparatus at present. With the current observation tools, the CCD camera with its 200 ms exposure time, and the PMT with its signal noise level (10%), we find no indication that there is significant spurious large-amplitude motion of the Be^+–HD^+ system. The spatial extent of the Be^+ ion CCD image is 0.5 μm in the two observed directions, corresponding to a temperature upper limit of 8 mK. Assuming the same temperature for the HD^+ and Be^+ ion, we can then place an upper limit to the HD^+ motional range of < 1 μm in each direction. Thus, for the 5.1 μm-wavelength fundamental transition the Dicke condition $kx_{\mathrm{RMS}} \lesssim 1$ is satisfied and a substantial recoil-free carrier transition is expected. Possibly, sideband cooling on the $(v = 0, L = 1) \rightarrow (v = 1, L = 0)$ vibrational transition will be feasible.

Finally, we point out that a major improvement in MHI spectroscopy would be the introduction of a non-destructive state detection technique that consequently allows to reuse the same molecular ion for multiple spectroscopy cycles, effectively reducing the spectroscopic data acquisition time. This will also reduce the number of loading events and hence the total experimentation time. Evidence that a heteronuclear MHI in an MHI-Be^+ ion pair is in a particular rovibrational state should be obtainable by coherently exciting the motion of the ion pair using an intense standing-wave near-resonantly tuned to a fundamental or low-overtone vibrational transition [23,34]. A suitable laser for this purpose appears to be a high-power continuous-wave optical parametric oscillator.

Acknowledgments

The authors are grateful to Prof. Johannes Hecker Denschlag's group (Universität Ulm) for providing their trap's CAD files.

We are indebted to M. G. Hansen for his assistance on frequency stabilisation of the Doppler cooling laser, to S. Alighanbari for his help with the HD^+ spectroscopy and photodissociation lasers, and to both for their insights and stimulating discussions. M.S., G.G. and C.W. acknowledge a fellowship from the Professor W. Behmenburg-Schenkung.

Disclosure statement

No potential conflict of interest was reported by the author(s).

Funding

This work has received funding from the European Research Council (ERC) under the European Union's Horizon 2020 research and innovation programme (grant agreement number 786306, 'PREMOL'), and from the Deutsche Forschungsgemeinschaft and Land Nordrhein-Westfalen in projects INST 208/667-1 FUGG and INST 208/737-1 FUGG. K. B. acknowledges support from the Alexander von Humboldt Foundation for a fellowship under Humboldt-ID 1159544.

ORCID

Christian Wellers http://orcid.org/0000-0001-6084-6495
Magnus R. Schenkel http://orcid.org/0000-0001-6048-9168
Gouri S. Giri http://orcid.org/0000-0002-6713-4412
Kenneth R. Brown http://orcid.org/0000-0001-7716-1425
Stephan Schiller http://orcid.org/0000-0002-0797-8648

References

[1] M.S. Safronova, D. Budker, D. DeMille, D.F.J. Kimball, A. Derevianko and C.W. Clark, Rev. Mod. Phys **90**, 025008 (2018). doi:10.1103/RevModPhys.90.025008
[2] D. DeMille, J.M. Doyle and A.O. Sushkov, Science **357** (6355), 990–994 (2017). doi:10.1126/science.aal3003
[3] I.V. Kortunov, S. Alighanbari, M.G. Hansen, G.S. Giri, V.I. Korobov and S. Schiller, Nat. Phys. **17**, 59–573 (2021). doi:10.1038/s41567-020-01150-7
[4] S. Alighanbari, G.S. Giri, F.L. Constantin, V.I. Korobov and S. Schiller, Nature **581**, 152–158 (2020). doi:10.1038/s41586-020-2261-5
[5] S. Patra, M. Germann, J.P. Karr, M. Haidar, L. Hilico, V.I. Korobov, F.M.J. Cozijn, K.S.E. Eikema, W. Ubachs and J.C.J. Koelemeij, Science **369**, 1238 (2020). doi:10.1126/science.aba0453
[6] D. Hanneke, R.A. Carollo and D.A. Lane, Phys. Rev. A **94**, 050101 (2016). doi:10.1103/PhysRevA.94.050101
[7] K. Beloy, M.G. Kozlov, A. Borschevsky, A.W. Hauser, V.V. Flambaum and P. Schwerdtfeger, Phys. Rev. A **83**, 062514 (2011). doi:10.1103/PhysRevA.83.062514
[8] M. Kajita, G. Gopakumar, M. Abe, M. Hada and M. Keller, Phys. Rev. A **89**, 032509 (2014). doi:10.1103/PhysRevA.89.032509
[9] J.P. Karr, J. Mol. Spectrosc. **300**, 37–43 (2014). doi:10.1016/j.jms.2014.03.016
[10] S. Schiller, D. Bakalov and V.I. Korobov, Phys. Rev. Lett **113**, 023004 (2014). doi:10.1103/PhysRevLett.113.023004
[11] S. Schiller and V. Korobov, Phys. Rev. A **71**, 032505 (2005). doi:10.1103/PhysRevA.71.032505
[12] P. Blythe, B. Roth, U. Fröhlich, H. Wenz and S. Schiller, Phys. Rev. Lett **95**, 183002 (2005). doi:10.1103/PhysRevLett.95.183002
[13] A. Ostendorf, C.B. Zhang, M.A. Wilson, D. Offenberg, B. Roth and S. Schiller, Phys. Rev. Lett. **97**, 243005 (2006). doi:10.1103/PhysRevLett.97.243005
[14] M. Germann, X. Tong and S. Willitsch, Nat. Phys. **10**, 820–824 (2014). doi:10.1038/nphys3085
[15] A.T. Calvin, S. Janardan, J. Condoluci, R. Rugango, E. Pretzsch, G. Shu and K.R. Brown, J. Phys. Chem. A **122**, 3177–3181 (2018). doi:10.1021/acs.jpca.7b12823
[16] A.T. Calvin and K.R. Brown, J. Phys. Chem. Lett. **9** (19), 5797–5804 (2018). doi:10.1021/acs.jpclett.8b01387PMID: 30212222.
[17] P.R. Stollenwerk, I.O. Antonov, S. Venkataramanababu, Y.W. Lin and B.C. Odom, Phys. Rev. Lett. **125**, 113201 (2020). doi:10.1103/PhysRevLett.125.113201
[18] H.G. Dehmelt, Bull. Am. Phys. Soc. **8**, 23 (1963).
[19] H.G. Dehmelt, Bull. Am. Phys. Soc. **7**, 470 (1962).
[20] H.G. Dehmelt, Phys. Rev. **103**, 1125–1126 (1956). doi:10.1103/PhysRev.103.1125
[21] F. Wolf, Y. Wan, J. Heip, F. Gebert, C. Shi and P. Schmidt, Nature **530**, 457–460 (2016). doi:10.1038/nature16513
[22] C. Chou, C. Kurz, D. Hume, P. Plessow, D.R. Leibrandt and D. Leibfried, Nature **545**, 203–207 (2017). doi:10.1038/nature22338
[23] M. Sinhal, Z. Meir, K. Najafian, G. Hegi and S. Willitsch, Science **367**, 1213–1218 (2020). doi:10.1126/science.aaz9837
[24] Y. Wan, F. Gebert, J.B. Wübbena, N. Scharnhorst, S. Amairi, I.D. Leroux, B. Hemmerling, N. Lärch, K. Hammerer and P.O. Schmidt, Nat. Commun. **5**, 3096 (2014). doi:10.1038/ncomms4096
[25] P.O. Schmidt, T. Rosenband, C. Langer, W.M. Itano, J.C. Bergquist and D.J. Wineland, Science **309**, 749–752 (2005). doi:10.1126/science.1114375
[26] J.C.J. Koelemeij, B. Roth and S. Schiller, Phys. Rev. A **76**, 023413 (2007). doi:10.1103/PhysRevA.76.023413
[27] D.B. Hume, C.W. Chou, D.R. Leibrandt, M.J. Thorpe, D.J. Wineland and T. Rosenband, Phys. Rev. Lett. **107**, 243902 (2011). doi:10.1103/PhysRevLett.107.243902
[28] N.B. Khanyile, G. Shu and K.R. Brown, Nat. Commun. **6**, 7825 (2015). doi:10.1038/ncomms8825
[29] V.I. Korobov, L. Hilico and J.P. Karr, Phys. Rev. Lett. **118**, 233001 (2017). doi:10.1103/PhysRevLett.118.233001
[30] B. Roth, J.C.J. Koelemeij, H. Daerr and S. Schiller, Phys. Rev. A **74**, 040501 (2006). doi:10.1103/PhysRevA.74.040501
[31] B. Roth and S. Schiller, in *Cold Molecules: Theory, Experiment, Applications*, edited by W.C. Stwalley, B. Friedrich, and R. Krems (CRC Press, Boca Raton, 2009).
[32] M.D. Barrett, B. DeMarco, T. Schaetz, V. Meyer, D. Leibfried, J. Britton, J. Chiaverini, W.M. Itano, B. Jelenković, J.D. Jost, C. Langer, T. Rosenband and D.J. Wineland, Phys. Rev. A **68**, 042302 (2003). doi:10.1103/PhysRevA.68.042302
[33] R.H. Dicke, Phys. Rev. **89**, 472–473 (1953). doi:10.1103/PhysRev.89.472
[34] J.C.J. Koelemeij, B. Roth, A. Wicht, I. Ernsting and S. Schiller, Phys. Rev. Lett. **98**, 173002 (2007). doi:10.1103/PhysRevLett.98.173002

[35] H.Y. Lo, J. Alonso, D. Kienzler, B.C. Keitch, L.E. de Clercq, V. Negnevitsky and J.P. Home, Appl. Phys. B **114**, 17–25 (2013). doi:10.1007/s00340-013-5605-0
[36] M.G. Hansen, E. Magoulakis, Q.F. Chen, I. Ernsting and S. Schiller, Opt. Lett. **40**, 2289–2292 (2015). doi:10.1364/OL.40.002289
[37] A.Y. Nevsky, S. Alighanbari, Q. Chen, I. Ernsting, S. Vasilyev, S. Schiller, G. Barwood, P. Gill, N. Poli and G.M. Tino, Opt. Lett. **38**, 4903–6 (2013). doi:10.1364/OL.38.004903
[38] J.P. Home, Adv. At. Mol. Opt. Phys., **62**, 231–277 (2013). doi:10.1016/B978-0-12-408090-4.00004-9
[39] D.J. Berkeland, J.D. Miller, J.C. Bergquist, W.M. Itano and D.J. Wineland, J. Appl. Phys. **83**, 5025–5033 (1998). doi:10.1063/1.367318
[40] S. Knünz, M. Herrmann, V. Batteiger, G. Saathoff, T.W. Hänsch and T. Udem, Phys. Rev. A **85**, 023427 (2012). doi:10.1103/PhysRevA.85.023427
[41] J. Schmidt, T. Louvradoux, J. Heinrich, N. Sillitoe, M. Simpson, J.P. Karr and L. Hilico, Phys. Rev. Appl. **14**, 024053 (2020). doi:10.1103/PhysRevApplied.14.024053
[42] S.T. Pratt, Rep. Prog. Phys. **58** (8), 821–883 (1995). doi:10.1088/0034-4885/58/8/001
[43] M.A. O'Halloran, S.T. Pratt, P.M. Dehmer and J.L. Dehmer, J. Chem. Phys. **87**, 3288–3298 (1987). doi:10.1063/1.453022
[44] P.M. Dehmer and W.A. Chupka, J. Chem. Phys. **79** (4), 1569–1580 (1983). doi:10.1063/1.446029
[45] S. Schiller, I. Kortunov, M. Hernández Vera, F. Gianturco and H. da Silva, Phys. Rev. A **95**, 043411 (2017). doi:10.1103/PhysRevA.95.043411
[46] Z. Amitay, D. Zajfman and P. Forck, Phys. Rev. A **50**, 2304–2308 (1994). doi:10.1103/PhysRevA.50.2304
[47] T. Schneider, B. Roth, H. Duncker, I. Ernsting and S. Schiller, Nat. Phys. **6**, 275–278 (2010). doi:10.1038/nphys1605
[48] M. Tadjeddine and G. Parlant, Mol. Phys. **33**, 1797–1803 (1977). doi:10.1080/00268977700101461
[49] U. Bressel, A. Borodin, J. Shen, M. Hansen, I. Ernsting and S. Schiller, Phys. Rev. Lett. **108**, 183003 (2012). doi:10.1103/PhysRevLett.108.183003

B. Winding Machine and Material Studies

Beryllium is an essential component of all our experiments. To ionise and to trap it, it must be routinely evaporated. Therefore, as much as possible should be stored in the ovens by winding up the brittle material. To produce windings that are as regular and dense as possible, a winding machine has been built (Figure B.1). The purpose of this machine was to avoid double windings or faults that would lead to cold or hot spots that could have a negative impact on the lifetime of the oven. Initially a tungsten blank (Figure B.2) is clamped between two stepper motors (motor A) with the help of specially developed chucks. These allow centred rotation of the thin filament around its axis, which prevents it from breaking off. For this, the two motors A must rotate synchronised in opposite directions. Depending on the winding speed and the (beryllium) wire thicknesses used, the wire supply must be moved forward with the feed carriage. Motor B is used for this. The winding speed and direction as well as the feed forward can be adjusted on the control unit. The number of turns as well as the length of the wrapped (beryllium) wire can be checked by the user on the display. An example with different winding densities is shown in Figure B.3. After about 30 cm of beryllium wire has been spooled, a chuck is loosened on one side and an additional rod (diameter 0.8 mm) is inserted axially on the other side. By holding the loose end and by a continuously slowly rotating motor A, the filament is wrapped around the rod. This procedure creates the double spiral shown above (Figure 5.14). It takes about 20 minutes to wrap an oven.

B.1. Tests with Materials other than Beryllium

Since beryllium is a toxic and expensive material, initial winding tests are carried out with other materials and in different thicknesses. As expected, soft copper works best, but a very thin tungsten or aluminium wire (both 25 µm diameter) can also be used to wrap around 100 µm thick tungsten (Figure B.4).

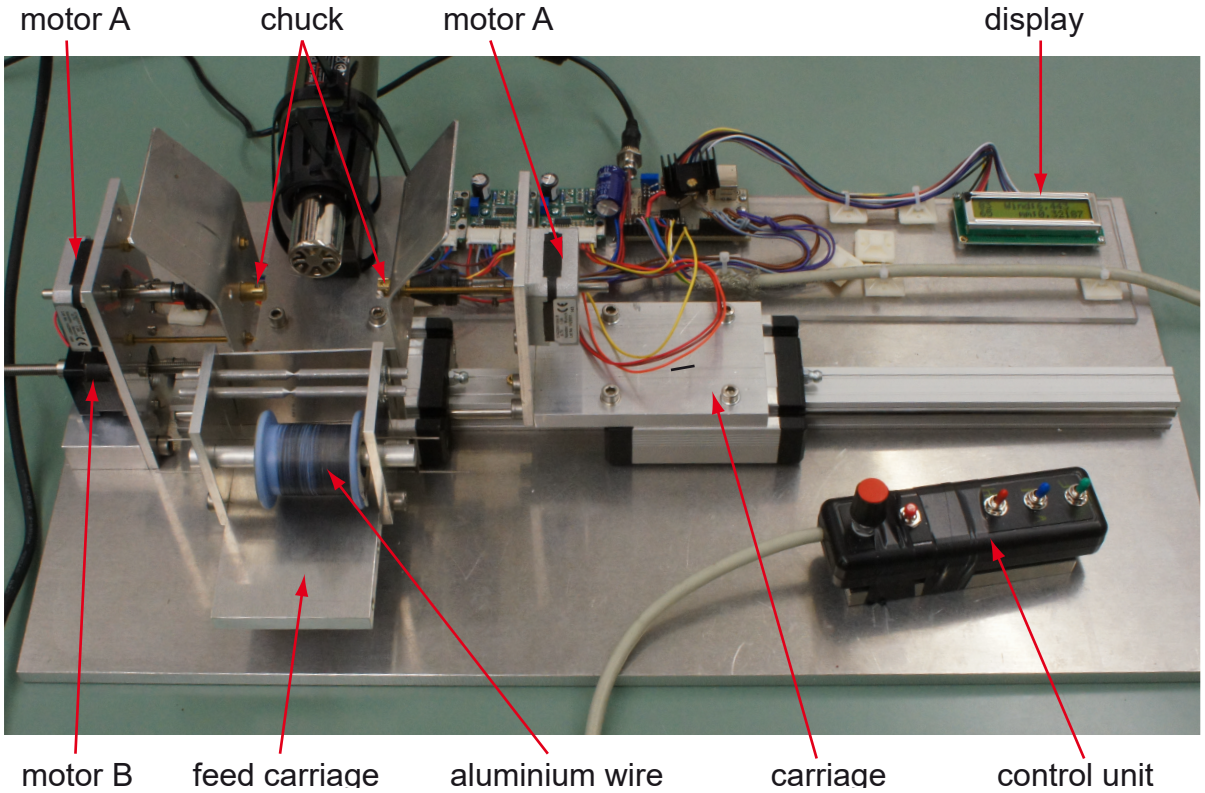

Figure B.1.: Winding machine: Overview of the components, explanation in the main text.

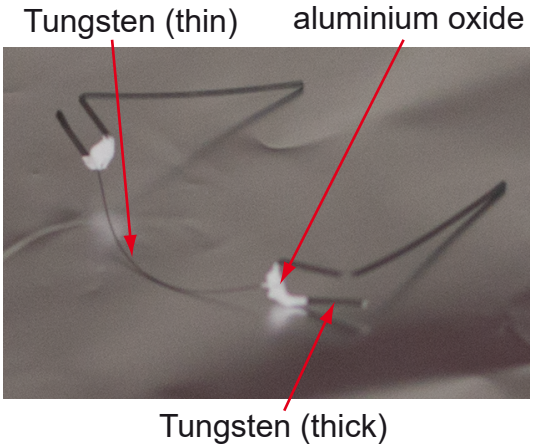

Figure B.2.: Tungsten blanks: The thin wire is approximately 2.5 cm long.

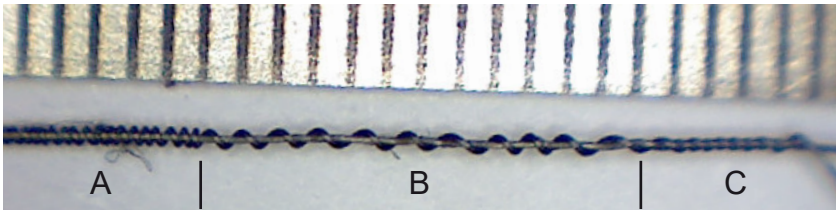

Figure B.3.: Example with different winding: Three windings per millimetre are set in section A, one in section B and four in section C. The millimetre grid of a ruler is shown at the top of the image.

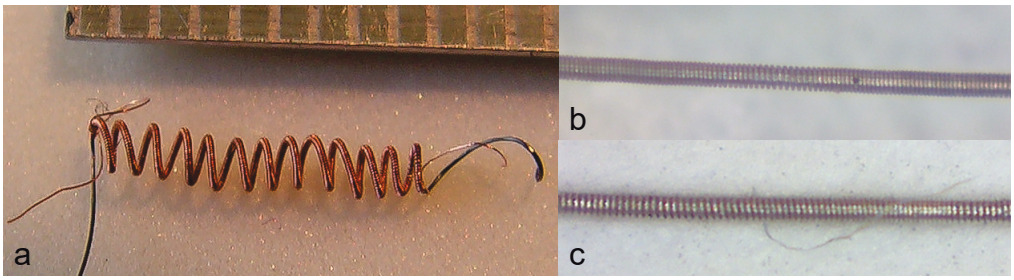

Figure B.4.: Winding tests with copper (a), tungsten (b) and aluminium (c) on 100 µm thick tungsten.

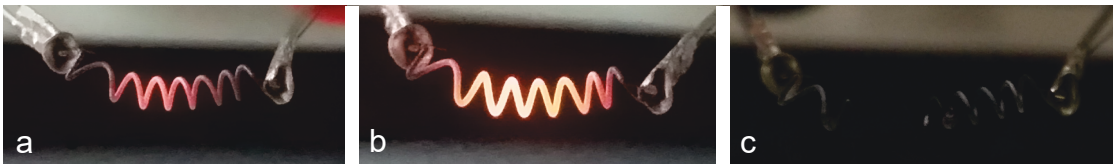

Figure B.5.: Annealing test of a tungsten/tungsten spiral: Applied current 1.6 A for a) and 2.2 A for b). The filament burns after a few seconds with the latter current (image c).

A simple test without a heating chamber and at atmosphere shows the heat distribution of the filament for a tungsten/tungsten double spiral. By applying 1.6 A, the beginning of the filament starts to glow (Figure B.5a). If the current is further increased to 2.2 A, the entire spiral glows, with the first part being the hottest (Figure B.5b). After a few seconds, the material burns at this spot (Figure B.5c). Without the additional air cooling, the currents mentioned here are much too high. In practice, a pressure increase in the vacuum chamber is already measured from 0.5 A, whereby a value of 0.63 to 0.69 A proves to be favourable for efficient operation of the experiment.

Bibliography

[1] V. I. Korobov, L. Hilico, J.-P. Karr, Fundamental Transitions and Ionization Energies of the Hydrogen Molecular Ions with Few ppt Uncertainty, Phys. Rev. Lett. 118 (2017) 233001. doi:10.1103/PhysRevLett.118.233001. ii, 1

[2] C. Wellers, M. R. Schenkel, G. S. Giri, K. R. Brown, S. Schiller, Controlled preparation and vibrational excitation of single ultracold molecular hydrogen ions, Molecular Physics 0 (0) (2021) e2001599. doi:10.1080/00268976.2021.2001599. 1, 47, 56, 57, 59, 62, 63, 82, 83, 84, 90, 91, 92

[3] I. V. Kortunov, S. Alighanbari, M. G. Hansen, G. S. Giri, V. I. Korobov, S. Schiller, Proton-electron mass ratio by high-resolution optical spectroscopy of ion ensembles in the resolved-carrier regime, Nat. Phys. 17 (2021) 59–573. doi:10.1038/s41567-020-01150-7. 1

[4] S. Alighanbari, M. G. Hansen, V. I. Korobov, S. Schiller, Rotational spectroscopy of cold and trapped molecular ions in the Lamb-Dicke regime, Nat. Phys. 14 (2018) 555. doi:10.1038/s41567-018-0074-3. 1

[5] S. Patra, M. Germann, J.-P. Karr, M. Haidar, L. Hilico, V. I. Korobov, F. M. J. Cozijn, K. S. E. Eikema, W. Ubachs, J. C. J. Koelemeij, Proton-electron mass ratio from laser spectroscopy of HD^+ at the part-per-trillion level, Science 369 (2020) 1238. doi:10.1126/science.aba0453. 1

[6] S. Alighanbari, Frequency metrology of HD^+ by ultra-high resolution rotational spectroscopy, Ph.D. thesis, Heinrich-Heine Universität (2020).
URL https://docserv.uni-duesseldorf.de/servlets/DocumentServlet?id=56418 1

[7] D. Hanneke, R. A. Carollo, D. A. Lane, High sensitivity to variation in the proton-to-electron mass ratio in $O_2{}^+$, Phys. Rev. A 94 (2016) 050101. doi:10.1103/PhysRevA.94.050101. 1

[8] K. Beloy, M. G. Kozlov, A. Borschevsky, A. W. Hauser, V. V. Flambaum, P. Schwerdtfeger, Rotational spectrum of the molecular ion NH^+ as a probe for α and m_e/m_p

variation, Phys. Rev. A 83 (6) (2011) 062514. doi:10.1103/PhysRevA.83.062514. 1

[9] M. Kajita, G. Gopakumar, M. Abe, M. Hada, M. Keller, Test of m_p/m_e changes using vibrational transitions in N_2^+, Phys. Rev. A 89 (2014) 032509. doi:10.1103/PhysRevA.89.032509. 1

[10] J.-P. Karr, H_2^+ and HD^+: candidates for a molecular clock, J. Mol. Spectrosc. 300 (2014) 37 – 43. doi:10.1016/j.jms.2014.03.016. 1, 3

[11] S. Schiller, D. Bakalov, A. K. Bekbaev, V. I. Korobov, Static and dynamic polarizability and the Stark and blackbody-radiation frequency shifts of the molecular hydrogen ions H_2^+, HD^+, and D_2^+, Phys. Rev. A 89 (2014) 052521. doi:10.1103/PhysRevA.89.052521. 1, 3

[12] S. Schiller, V. Korobov, Test of time-dependence of the electron and nuclear masses with ultracold molecules, Phys. Rev. A 71 (2005) 032505. doi:10.1103/PhysRevA.71.032505. 1

[13] P. Blythe, B. Roth, U. Fröhlich, H. Wenz, S. Schiller, Production of ultracold trapped molecular hydrogen ions, Phys. Rev. Lett. 95 (2005) 183002. doi:10.1103/PhysRevLett.95.183002. 1

[14] D. Offenberg, C. B. Zhang, C. Wellers, B. Roth, S. Schiller, Translational cooling and storage of protonated proteins in an ion trap at subkelvin temperatures, Phys. Rev. A 78 (2008) 061401. doi:10.1103/PhysRevA.78.061401. 1

[15] M. Germann, X. Tong, S. Willitsch, Observation of dipole-forbidden transitions in sympathetically cooled, state-selected, homonuclear diatomic molecular ions, Nature Physics 10 (2014) 820–824. doi:10.1038/nphys3085. 1

[16] A. T. Calvin, K. R. Brown, Spectroscopy of molecular ions in coulomb crystals, J. Phys. Chem. Lett. 9 (19) (2018) 5797–5804, pMID: 30212222. doi:10.1021/acs.jpclett.8b01387. 1

[17] A. T. Calvin, S. Janardan, J. Condoluci, R. Rugango, E. Pretzsch, G. Shu, K. R. Brown, Rovibronic Spectroscopy of Sympathetically Cooled $^{40}CaH^+$, The Journal of Physical Chemistry A 122 (2018) 3177–3181. doi:10.1021/acs.jpca.7b12823. 1

[18] P. R. Stollenwerk, I. O. Antonov, S. Venkataramanababu, Y.-W. Lin, B. C. Odom, Cooling of a zero-nuclear-spin molecular ion to a selected rotational state, Phys. Rev. Lett. 125 (2020) 113201. doi:10.1103/PhysRevLett.125.113201. 1

[19] H. G. Dehmelt, Bull. Am. Phys. Soc. 8 (1963) 23. 1

[20] H. G. Dehmelt, Bull. Am. Phys. Soc. 7 (1962) 470. 1

[21] H. G. Dehmelt, Paramagnetic resonance reorientation of atoms and ions aligned by electron impact, Phys. Rev. 103 (1956) 1125–1126. doi:10.1103/PhysRev.103.1125. 1

[22] F. Wolf, Y. Wan, J. Heip, F. Gebert, C. Shi, P. Schmidt, Non-destructive state detection for quantum logic spectroscopy of molecular ions, Nature 530 (2016) 457–460. doi:10.1038/nature16513. 1, 93

[23] C. Chou, C. Kurz, D. Hume, P. Plessow, D. R. Leibrandt, D. Leibfried, Preparation and Coherent Manipulation of Pure Quantum States of a Single Molecular Ion, Nature 545 (2017) 203–207. doi:doi:10.1038/nature22338. 1, 93

[24] M. Sinhal, Z. Meir, K. Najafian, G. Hegi, S. Willitsch, Quantum-nondemolition state detection and spectroscopy of single trapped molecules, Science 367 (6483) (2020) 1213–1218. doi:10.1126/science.aaz9837. 1

[25] J. C. J. Koelemeij, B. Roth, S. Schiller, Blackbody thermometry with cold molecular ions and application to ion-based frequency standards, Phys. Rev. A 76 (2007) 023413. doi:10.1103/PhysRevA.76.023413. 1, 93

[26] D. B. Hume, C. W. Chou, D. R. Leibrandt, M. J. Thorpe, D. J. Wineland, T. Rosenband, Trapped-ion state detection through coherent motion, Phys. Rev. Lett. 107 (2011) 243902. doi:10.1103/physrevlett.107.243902. 1, 94

[27] Y. Wan, F. Gebert, J. B. Wäbbena, N. Scharnhorst, S. Amairi, I. D. Leroux, B. Hemmerling, N. Lärch, K. Hammerer, P. O. Schmidt, Precision spectroscopy by photon-recoil signal amplification, Nat. Commun. 5 (2014) 3096. doi:10.1038/ncomms4096. 1

[28] P. O. Schmidt, T. Rosenband, C. Langer, W. M. Itano, J. C. Bergquist, D. J. Wineland, Spectroscopy using quantum logic, Science 309 (2005) 749–752. doi:10.1126/science.1114375. 1

[29] S. Alighanbari, G. S. Giri, F. L. Constantin, V. I. Korobov, S. Schiller, Precise test of quantum electrodynamics and determination of fundamental constants with HD^+ ions, Nature 581 (2020) 152 – 158. doi:10.1038/s41586-020-2261-5. 1

[30] R. Moss, Calculations for vibration-rotation levels of HD^+, in particular for high N, Molecular Physics 78 (1993) 371–405. doi:10.1080/00268979300100291. 2, 19, 87, 89

[31] B. D. Esry, H. R. Sadeghpour, Adiabatic formulation of heteronuclear hydrogen molecular ion, Physical Review A 60 (5) (1999) 3604–3617. doi:10.1103/physreva.60.3604. 2, 87, 89

[32] B. Roth, J. C. J. Koelemeij, H. Daerr, S. Schiller, Rovibrational spectroscopy of trapped molecular hydrogen ions at millikelvin temperatures, Phys. Rev. A 74 (2006) 040501. doi:10.1103/PhysRevA.74.040501. 3

[33] J. B. Wübbena, S. Amairi, O. Mandel, P. O. Schmidt, Sympathetic cooling of mixed-species two-ion crystals for precision spectroscopy, Phys. Rev. A 85 (2012) 043412. doi:10.1103/PhysRevA.85.043412. 4

[34] P. K. Ghosh, Ion Traps, OXFORD UNIV PR, 1996. 7

[35] F. G. Major, V. N. Gheorghe, G. Werth, Charged Particle Traps, Springer-Verlag, 2005. doi:10.1007/b137836. 7

[36] J. F. T. Raymond E. March, Quadrupole Ion Trap Mass Spectrometry, John Wiley & Sons, 2005. doi:10.1002/9780470027318.a6015. 7, 10, 11

[37] P. H. Dawson (Ed.), Quadrupole Mass Spectrometry and Its Applications, American Institute of Physics, 1995. 7

[38] J. F. J. T. Raymond E. March (Ed.), Practical Aspects of Ion Trap Mass Spectrometry, Volume I, CRC Press, 1995. 7, 11

[39] W. Paul, H. Steinwedel, Improved Arrangements for Separating or Separately Detecting Charged Particles of Different Specific Charges, Great Britain, 773689 (1957). 7

[40] M. Drewsen and A.Brøner, Harmonic linear Paul trap: Stability diagram and effective potentials, Phys. Rev. A 62 (2000) 045401. doi:10.1103/PhysRevA.62.045401. 7

[41] W. T. Scott, Who Was Earnshaw?, American Journal of Physics 27 (1959). doi:10.1119/1.1934886. 8

[42] A. Ostendorf, Sympathetische Kühlung von Molekülionen durch lasergekühlte Bariumionen in einer linearen Paulfalle, Ph.D. thesis, Heinrich-Heine Universität

(2005).
URL https://docserv.uni-duesseldorf.de/servlets/DocumentServlet?id=3404 9

[43] D. Leibfried and D. Lucas, Trapping and cooling of atomic ions, Proceedings of the International School of Physics "Enrico Fermi" 189 (Ion Traps for Tomorrow's Applications) (2015) 1–63. doi:10.3254/978-1-61499-526-5-1. 10

[44] R. F. Wuerker, H. Shelton, R. V. Langmuir, Electrodynamic Containment of Charged Particles, Journal of Applied Physics 30 (1959). doi:10.1063/1.1735165. 11

[45] P. L. Kapitza, Dynamic stability of a pendulum when its point of suspension vibrates, Soviet Phys. JETP. 51 (1951). 11

[46] P. L. Kapitza, A pendulum with oscillating suspension, Uspekhi Fizicheskikh Nauk 44 (1951). 11

[47] L. D. Landau and E. M. Lifshitz, Mechanics, Pergamon Press, 1960. 11

[48] D. J. Berkeland, J. D. Miller, J. C. Bergquist, W. M. Itano, D. J. Wineland, Minimization of ion micromotion in Paul trap, J. Appl. Phys. 83 (1998) 5025–5033. doi:10.1063/1.367318. 12

[49] B. Rohde, Experimente zur Quanteninformationsverarbeitung in einer linearen Ionenfalle, Ph.D. thesis, Leopold-Franzens-Universität Innsbruck (2001).
URL https://www.quantumoptics.at/images/publications/dissertation/rohde_diss.pdf 12

[50] D. James, Quantum dynamics of cold trapped ions with application to quantum computation, Applied Physics B: Lasers and Optics 66 (2) (1998) 181–190. doi:10.1007/s003400050373. 13, 16

[51] X.-L. Deng, D. Porras, J. I. Cirac, Effective spin quantum phases in systems of trapped ions, Physical Review A 72 (2005). doi:10.1103/physreva.72.063407. 13

[52] J. P. Home, Quantum science and metrology with mixed-species ion chains, in: Advances In Atomic, Molecular, and Optical Physics, Elsevier, 2013, pp. 231–277. doi:10.1016/b978-0-12-408090-4.00004-9. 15

[53] W. Caswell, G. Lepage, Effective lagrangians for bound state problems in QED, QCD, and other field theories, Physics Letters B 167 (4) (1986) 437–442. doi:10.1016/0370-2693(86)91297-9. 17

[54] P.-P. Zhang, Z.-X. Zhong, Z.-C. Yan, T.-Y. Shi, Precision spectroscopy of the hydrogen molecular ion D_2^+, Phys. Rev. A 93 (2016) 032507. doi:10.1103/PhysRevA.93.032507. 20

[55] D. Bakalov, V. I. Korobov, S. Schiller, High-precision calculation of the hyperfine structure of the HD^+ ion, Phys. Rev. Lett. 97 (2006) 243001. doi:10.1103/PhysRevLett.97.243001. 19, 97

[56] D. Bakalov, V. Korobov, S. Schiller, Magnetic field effects in the transitions of the HD^+ molecular ion and precision spectroscopy, J. Phys. B: At. Mol. Opt. Phys. 44, 025003 (2011); Corrigendum, J. Phys. B: At. Mol. Opt. Phys. 45 (2012) 049501. doi:10.1088/0953-4075/45/4/049501. 21

[57] G.H. Dunn, Photodissociation of H_2^+ and D_2^+: Theory and Tables, JILA report 92 (1986). 22

[58] C. Monroe, D. M. Meekhof, B. E. King, S. R. Jefferts, W. M. Itano, D. J. Wineland, P. Gould, Resolved-Sideband Raman Cooling of a Bound Atom to the 3D Zero-Point Energy, Phys. Rev. Lett. 75 (22) (1995) 4011–4014. doi:10.1103/physrevlett.75.4011. 25, 30

[59] T. Andersen, K. A. Jessen, G. Sørensen, Mean-life measurements of excited electronic states in neutral and ionic species of beryllium and boron, Physical Review 188 (1) (1969) 76–81. doi:10.1103/physrev.188.76. 25

[60] N. Shiga, W. M. Itano, J. J. Bollinger, Diamagnetic correction to the $^9Be^+$ ground-state hyperfine constant, Phys. Rev. A 84 (1) (2011) 012510. doi:10.1103/PhysRevA.84.012510. 26

[61] G. Breit, I. I. Rabi, Measurement of Nuclear Spin, Physical Review 38 (11) (1931) 2082–2083. doi:10.1103/PhysRev.38.2082.2. 26

[62] P. R. Berman, V. S. Malinovsky, Principles of Laser Spectroscopy and Quantum Optics, Princeton Univ Pr, 2011. 28, 29

[63] F. Schmidt-Kaler, H. Häffner, S. Gulde, M. Riebe, G. P. T. Lancaster, T. Deuschle, C. Becher, W. Hänsel, J. Eschner, C. F. Roos, R. Blatt, How to realize a universal quantum gate with trapped ions, Applied Physics B: Lasers and Optics 77 (8-8) (2003) 789–796. doi:10.1007/s00340-003-1346-9. 37

[64] U. Fröhlich, Coulomb Crystal Studies, Sympathetic Cooling, and Mass Spectrometry Using Laser-Cooled Be^+ Ions, Ph.D. thesis, Heinrich-Heine Universität Düsseldorf (2008).
URL https://docserv.uni-duesseldorf.de/servlets/DocumentServlet?id=10396 40, 41

[65] M. G. Hansen, E. Magoulakis, Q.-F. Chen, I. Ernsting, S. Schiller, Quantum cascade laser-based mid-IR frequency metrology system with ultra-narrow linewidth and 1×10^{-13}-level frequency instability, Opt. Lett. 40 (2015) 2289–2292. doi:10.1364/OL.40.002289. 47

[66] A. Y. Nevsky, S. Alighanbari, Q. Chen, I. Ernsting, S. Vasilyev, S. Schiller, G. Barwood, P. Gill, N. Poli, G. M. Tino, Robust frequency stabilization of multiple spectroscopy lasers with large and tunable offset frequencies 38 (2013) 4903–6. doi:10.1364/ol.38.004903. 47

[67] H.-Y. Lo, J. Alonso, D. Kienzler, B. C. Keitch, L. E. de Clercq, V. Negnevitsky, J. P. Home, All-solid-state continuous-wave laser systems for ionization, cooling and quantum state manipulation of beryllium ions, Applied Physics B 114 (1-2) (2013) 17–25. doi:10.1007/s00340-013-5605-0. 55

[68] V. Rajagopal, J. P. Marler, M. G. Kokish, B. C. Odom, Trapped ion chain thermometry and mass spectrometry through imaging, European Journal of Mass Spectrometry 22 (1) (2016) 1–7. doi:10.1255/ejms.1408. 63

[69] K. Okada, M. Wada, T. Nakamura, R. Iida, S. Ohtani, J.-i. Tanaka, H. Kawakami, I. Katayama, Laser-Microwave Double-Resonance Spectroscopy of Laser-Cooled $^9Be^+$ Ions in a Weak Magnetic Field for Studying Unstable Be Isotopes, Journal of the Physical Society of Japan 67 (9) (1998) 3073. doi:10.1143/JPSJ.67.3073. 67, 70

[70] J. Shen, A. Borodin, S. Schiller, A simple method for characterization of the magnetic field in an ion trap using Be^+ ions, Eur. Phys. J. D 68 (2014) 359. doi:10.1140/epjd/e2014-50360-7. 72

[71] L. Matus, I. Opauszky, D. Hyatt, A. J. Masson, K. Birkinshaw, M. J. Henchman, Kinematic investigations of ion-neutral collision mechanisms at ≈ 1 ev, Discuss. Faraday Soc. 44 (1967) 146–156. doi:10.1039/DF9674400146. 85

[72] Z. Amitay, D. Zajfman, P. Forck, Rotational and vibrational lifetime of isotopically asymmetrized homonuclear diatomic molecular ions, Phys. Rev. A 50 (1994) 2304–2308. doi:10.1103/PhysRevA.50.2304. 86, 96, 98, 100

[73] T. Schneider, B. Roth, H. Duncker, I. Ernsting, S. Schiller, All-optical preparation of molecular ions in the rovibrational ground state, Nature Physics 6 (2010) 275 – 278. doi:10.1038/nphys1605. 86

[74] S. Schiller, I. Kortunov, M. Hernández Vera, F. Gianturco, H. da Silva, Quantum state preparation of homonuclear molecular ions enabled via a cold buffer gas: An ab initio study for the H_2^+ and the D_2^+ case, Phys. Rev. A 95 (2017) 043411. doi:10.1103/PhysRevA.95.043411. 88

[75] J. Schmidt, T. Louvradoux, J. Heinrich, N. Sillitoe, M. Simpson, J.-P. Karr, L. Hilico, Trapping, cooling, and photodissociation analysis of state-selected H_2^+ ions produced by (3 + 1) multiphoton ionization, Phys. Rev. Applied 14 (2020) 024053. doi:10.1103/PhysRevApplied.14.024053. 88

[76] M. Tadjeddine, G. Parlant, Computed photodissociation cross sections of HD and Franck-Condon factors for the ionization of HD, Molecular Physics 33 (6) (1977) 1797–1803. doi:10.1080/00268977700101461. 88

[77] D. Leibfried, B. DeMarco, V. Meyer, D. Lucas, M. Barrett, J. Britton, W. M. Itano, B. Jelenković, C. Langer, T. Rosenband, D. J. Wineland, Experimental demonstration of a robust, high-fidelity geometric two ion-qubit phase gate, Nature 422 (6930) (2003) 412–415. doi:10.1038/nature01492. 93

[78] M. R. Schenkel, Simulation of a HD^+-Be^+ two-ion crystal in a linear Paultrap under the influence of a time-dependent optical force, Spezialisierung (2019). 94, 95

[79] C. Zhang, Production and sympathetic cooling of complex molecular ions, Ph.D. thesis, Heinrich-Heine-Universität Düsseldorf (2008).
URL http://docserv.uniduesseldorf.de/servlets/DocumentServlet?id=9606 94

[80] Z. Meir, G. Hegi, K. Najafian, M. Sinhal, S. Willitsch, State-selective coherent motional excitation as a new approach for the manipulation, spectroscopy and state-to-state chemistry of single molecular ions, Faraday Discussions 217 (2018) 561–583. doi:10.1039/c8fd00195b. 94, 95

[81] Q.-L. Tian, L.-Y. Tang, Z.-X. Zhong, Z.-C. Yan, T.-Y. Shi, Oscillator strengths between low-lying ro-vibrational states of hydrogen molecular ions, Journal of Chemical Physics 137 (2) (2012) 024311–024311. doi:10.1063/1.4733988. 95

[82] H. Olivares Pilón, D. Baye, Dipole transitions in the bound rotational-vibrational spectrum of the heteronuclear molecular ion HD^+, Phys. Rev. A 88 (3) (2013) 032502. doi:10.1103/PhysRevA.88.032502. 95